


REVIEW

Open Access



# Remote sensing and its applications using GNSS reflected signals: advances and prospects

Shuanggen Jin<sup>1,2\*</sup> , Adriano Camps<sup>3</sup>, Yan Jia<sup>4</sup>, Feng Wang<sup>5</sup>, Manuel Martin-Neira<sup>6</sup>, Feixiong Huang<sup>7</sup>, Qingyun Yan<sup>8</sup>, Shuangcheng Zhang<sup>9</sup>, Zhongyu Li<sup>10</sup>, Komi Edokossi<sup>8</sup>, Dongkai Yang<sup>5</sup>, Zhiyu Xiao<sup>4</sup>, Zhongmin Ma<sup>9</sup> and Weihua Bai<sup>7</sup>

## Abstract

The Global Navigation Satellite Systems (GNSS), including the US's GPS, China's BDS, the European Union's Galileo, and Russia's GLONASS, offer real-time, all-weather, any-time, anywhere and high precision observations by transmitting L band signals continuously, which have been widely used for positioning, navigation and timing. With the development of GNSS technology, it has been found that GNSS-reflected signals can be used to detect Earth's surface characteristics together with other signals of opportunity. In this paper, the current status and latest advances are presented on Global Navigation Satellite System-Reflectometry (GNSS-R) in theory, methods, techniques and observations. New developments and progresses in GNSS-R instruments, theoretical modeling, and signal processing, ground and space-/air-borne experiments, parameters retrieval (e.g. wind speed, sea surface height, soil moisture, ice thickness), sea surface altimetry and applications in the atmosphere, oceans, land, vegetation, and cryosphere are given and reviewed in details. Meanwhile, the challenges in the GNSS-R development of each field are also given. Finally, the future applications and prospects of GNSS-R are discussed, including multi-GNSS reflectometry, new GNSS-R receivers, GNSS-R missions, and emerging applications, such as mesoscale ocean eddies, ocean phytoplankton blooms, microplastics detection, target recognition, river flow, desert studies, natural hazards and landslides monitoring.

**Keywords** GNSS, Reflectometry, Remote sensing, Environmental change

\*Correspondence:

Shuanggen Jin  
sgjin@shao.ac.cn

<sup>1</sup> Shanghai Astronomical Observatory, Chinese Academy of Sciences, Shanghai 200030, China

<sup>2</sup> School of Surveying and Land Information Engineering, Henan Polytechnic University, Jiaozuo 454003, China

<sup>3</sup> Department of Signal Theory and Communications, Technical University of Catalonia, Barcelona 08034, Spain

<sup>4</sup> Department of Surveying and Geoinformatics, Nanjing University of Posts and Telecommunications, Nanjing 210023, China

<sup>5</sup> School of Electronics and Information Engineering, Beihang University, Beijing 100191, China

<sup>6</sup> European Space Research and Technology Centre (ESTEC), European Space Agency, 2200-AG Noordwijk, The Netherlands

<sup>7</sup> National Space Science Center, Chinese Academy of Sciences, Beijing 100190, China

<sup>8</sup> School of Remote Sensing and Geomatics Engineering, Nanjing University of Information Science and Technology, Nanjing 210044, China

<sup>9</sup> College of Geological Engineering and Geomatics, Chang'an University, Xi'an 710054, China

<sup>10</sup> University of Electronic Science and Technology of China, Chengdu 611731, China



© The Author(s) 2024. **Open Access** This article is licensed under a Creative Commons Attribution 4.0 International License, which permits use, sharing, adaptation, distribution and reproduction in any medium or format, as long as you give appropriate credit to the original author(s) and the source, provide a link to the Creative Commons licence, and indicate if changes were made. The images or other third party material in this article are included in the article's Creative Commons licence, unless indicated otherwise in a credit line to the material. If material is not included in the article's Creative Commons licence and your intended use is not permitted by statutory regulation or exceeds the permitted use, you will need to obtain permission directly from the copyright holder. To view a copy of this licence, visit <http://creativecommons.org/licenses/by/4.0/>.

## Introduction

Global Navigation Satellite Systems (GNSS) include the US's Global Positioning System (GPS), China's BeiDou Navigation Satellite System (BDS), Russia's GLONASS System (GLONASS) and Europe's Galileo Navigation Satellite System (Galileo), as well as regional augmentation systems (e.g. Japan's Quasi-Zenith Satellite System (QZSS) and India's Regional Navigation Satellite System (IRNSS)). All of them are characterized by all-weather, real-time, any time, anywhere and high precision capabilities. These systems continuously transmit L-band signals and are broadly used in Positioning, Navigation, and Timing (PNT). As various navigation satellite systems gradually improve and the number of GNSS observation stations increases, their application fields are becoming increasingly extensive. GNSS is not only used in PNT, but also can use its surface reflection signal for remote sensing. GNSS satellites continuously broadcast radio signals to Earth, and some of them are reflected off the Earth's surface. Delayed GNSS signals reflected from rough surfaces can provide different information about the direct and reflected signal paths (Jin et al., 2011; Najibi & Jin, 2013). This information includes changes in the waveform, amplitude, phase, and frequency of the reflected signal. Changes in polarization characteristics are directly associated with the properties of the reflecting surface. Combined to the receiver antenna position and medium information, the delay measurement and the reflecting surface properties can be used to determine the surface roughness and properties, namely GNSS-R (Global Navigation Satellite System-Reflectometry).

In 1988, Hall and Cordey (1988) firstly proposed the use of GPS reflected signals for scatterometry applications. Later on, GPS reflection measurement was first proposed for altimetry by the European Space Agency (ESA) scientist Manuel Martin-Neira in 1993, that is, the GPS surface reflection signal and the direct signal are received by the receiver together, and the delay between them can be used for altimetry applications (Martin-Neira, 1993), namely Passive Reflectometry and Interferometry System (PARIS). In 1994, French scientists published the results that accidentally a receiver locked to sea surface reflected signals during a flight test, but because of its impact on positioning accuracy, it is usually rejected as a multipath signal (Auber et al., 1994). In 1996, the scientists at National Aeronautical and Space Administration's (NASA) Langley Research Center used dual-frequency GPS signals to perform sea forward scatter to obtain and eliminate ionospheric delays, which made up for the shortcomings of traditional satellite altimeters. However, ground-based experiments showed that traditional

receivers are difficult to track GNSS reflected signals for a long time and effectively. For phase locking, a new type of receiver should be developed (Katzberg & Garrison, 1996). In 1997, the ESA carried out the GNSS-R sea surface altimetry experiment—the PARIS altimeter Zeeland Bridge I experiment in the Netherlands (Martin-Neira et al., 2001). In October 2000, the National Oceanic and Atmospheric Administration's (NOAA) aircraft, "Hurricane Hunter", carried GNSS-R equipment and flew into Hurricane "Michael" from the coast of South Carolina, and analyzed the reflection from the tropical cyclone sea surface. The returned GPS signal obtained the wind speed signature (Katzberg et al., 2001). In 2003, the United Kingdom-Disaster Monitoring Constellation (UK-DMC) satellite successfully obtained the physical coefficients of the Earth's surface, including sea surface roughness, by using the GNSS-R equipment carried on it (Gleason et al., 2005). The GPS reflection signal in the tranquil sea area can also obtain high-precision altimetry results (Gleason et al., 2010).

The first space-borne GNSS-R Technology Demonstration Satellite-1 (TDS-1) launched in 2014, provided Delay-Doppler Map (DDM) data products and paved the way for the application of spaceborne GNSS reflection measurement. In addition, many other scientific institutions have conducted a series of theoretical studies as well as experiments on GNSS-reflected signals, developed new GNSS-R receivers, and performed application tests across various platforms such as ground, coast, bridge, and aircraft, as well as examining the use of GNSS-R for estimating sea surface (such as height and wind speed) and land surface, and numerous results and progress have been obtained. In particular, the Cyclone Global Navigation Satellite System (CYGNSS) mission, launched on December 15, 2016, consisting of eight microsatellites constellation jointly operated by the NASA and the University of Michigan (UM), provided a huge amount of space-borne GNSS-R data and made a number of progress in oceans, e.g. wind speed, sea surface, and significant wave height (Cardellach et al., 2011; Clarizia & Ruf, 2016; Foti et al., 2017; Qiu & Jin, 2020; Wang et al., 2019; Yang et al., 2021a) and the land, e.g., soil moisture and soil freeze/thaw cycles (Dong & Jin, 2021; Wu et al., 2020).

In this paper, the detailed principles, methods, and latest application progresses of GNSS-R are presented and reviewed, including instruments, theoretical modeling, signal processing, ground and space-/airborne experiments, and remote sensing of the atmosphere, oceans, lands, vegetation, hydrology, and ice and snow characteristics. Notably, the recent progresses on BDS-R and TDS-1/CYGNSS GNSS-R applications are highlighted. In the end, the future applications and

prospects of GNSS-R are discussed, such as multi-GNSS reflectometry, new GNSS-R receivers, GNSS-R satellite programs, and small- to medium-sized feature and target detection.

### Theory and methods

GNSS-R consists of collecting the reflected signals from sources of opportunity as well as, sometimes, the corresponding direct signals, and then performing some processing to retrieve geophysical parameters of interesting reflecting surface. By “reflected” signals it is understood the composite signal emanating from very many scatterers at and around the “specular” point. The specular reflection point is to be defined as the location on the reflecting surface with the shortest transit time among all possible transmitter-surface-receiver paths. Therefore, the coordinates of the specular reflection point can be estimated based on the positions of the transmitter, receiver, and reflecting surface. In practice, the exact position of the reflecting surface is not known, and a model is used as an approximation to the real reflecting surface, from which the specular point is estimated by numerical methods. An ideal model of the reflecting surface should have a resolution comparable to the wavelength, but this is impractical. Geoid models over the ocean and digital elevation models over land are used instead. Over land, because of the slopes of the terrain, it may happen that there are multiple reflection points, but they are typically clustered around the specular point one would find when removing those slopes. It is important to understand that GNSS-R has developed in this way, that is, by exploiting signals reflected at and around the specular point, as proposed by Martin-Neira (1993). Signals scattered from the points far away from the specular point have generally too low power to be useful for retrievals and therefore are not used.

The signals reflected off the Earth’s surface, whether on the ground, air-borne, or on space-borne satellites, are captured by GNSS-R receivers. These observables are utilized in a range of applications such as land surface and sea surface parameter estimations. The methodology is categorized into 2 groups: the first one uses receivers equipped with at least 2 antennas to analyze the GNSS waveforms, while the second employs a classical GNSS receiver with a single antenna. The first group is suited for in-situ observations, aircraft, and satellite observations, while the second one is only applicable for in-situ observations or low-altitude flights.

In terms of signal acquisition and processing techniques, there are conventional (cGNSS-R) and interferometric (iGNSS-R) receivers. cGNSS-R establishes

the correlation at  $T_c$  between the reflected signal  $S_r(t)$  and a replica  $a^*(t)$  of the receiver-generated Pseudo-Random Noise (PRN) code, factoring a time log  $\tau$ , and after compensating for Doppler frequency shift  $f_d$  (Park et al., 2014a, b). The amplitude of the correlation  $Y^c$  can be written as:

$$Y^c(t_0, \tau, f_d) = \frac{1}{T_c} \int_{t_0}^{t_0+T_c} S_r(t) a^*(t - \tau) e^{-j2\pi(f_c+f_d)t} dt. \quad (1)$$

where  $t_0$  is the time that marks the point at which the coherent integration begins. In order to improve  $Y^c$ , an incoherent average ( $N_i$ ) must be used:

$$\langle |Y^c(\tau, f_d)|^2 \rangle \approx \frac{1}{N_i} \sum_{n=1}^{N_i} |Y^c(t_n, \tau, f_d)|^2. \quad (2)$$

This technique has several advantages including the separation of the signals via their precise code, infinite Signal-to-Noise Ratio (SNR), smaller antennas, etc., however, some limited-bandwidth Pseudo-Random Noise (PRN) codes, such as GPS L1 C/A code, are not suitable for altimetry (Park et al., 2014a, b). This implementation is employed in the CYGNSS mission.

The second group including interferometric waveform receivers (iGNSS-R) employs the correlation between the reflected and the direct signal ( $S_d$ ) instead of the reflected signals and the replica (Park et al., 2014a, b):

$$Y^i(t_0, \tau, f_d) = \frac{1}{T_c} \int_{t_0}^{t_0+T_c} S_r(t) S_d(t - \tau) e^{-j2\pi(f_c+f_d)t} dt \quad (3)$$

$$\langle |Y^i(\tau, f_d)|^2 \rangle \approx \frac{1}{N_i} \sum_{n=1}^{N_i} |Y^i(t_n, \tau, f_d)|^2. \quad (4)$$

Several advantages including the improved code-free SNR, increased bandwidth, the ability to utilize satellite television and radio signals, and cross-correlation differential processing featuring low delay and readily easy-to-track Doppler frequency dynamics are characteristics of this technique (Park et al., 2014a, b). However, large antennas for up-looking are required for this technique (Zavorotny & Voronovich, 2000).

### Geometry of GNSS-R

A GNSS-R receiver has different access to direct and reflected signals, depending mainly on its altitude over the ground. Ground receivers at the top of a tripod or a mast, at the tip of a boom, on top of a building, etc.... receive direct signals from above their local horizon and reflected signals from below their local horizon plane. For these receivers nearby obstacles as trees, buildings, mountains, etc.... may limit the reception of the signals

of opportunity. The Earth can be approximated as flat with the delay separation between reflected and direct signals typically less than one chip of the modulating signal. Near-ground receivers embarked on drones, aircraft, or balloons, have a similar geometry to ground receivers, except that the Earth curvature may have to be considered for certain applications such as altimetry, and some direct signals can be acquired from below the local horizon. This relative delay between the reflected and the direct signals may exceed one chip, enabling the separation in the delay of the reflected waveform from the direct one. Finally, for space-borne GNSS-R receivers, the reflected signal is captured by the low-Earth-orbit satellites (e.g., TDS-1 or CYGNSS satellite). The Earth's reflected surface is not flat, while it can be approximate by an ellipsoid.

**Single antenna interference**

The Interference Pattern Technique (IPT) utilizes a single antenna equipped with dual polarization, combining both polarizations to generate interference in the measured SNR, comprising both the reflected SNR ( $SNR_r$ ) and direct SNR ( $SNR_d$ ). This interference facilitates the estimation of soil moisture content (SMC) and vegetation characteristics. The IPT can be categorized into two primary types: the interference pattern technique and the multipath method/SNR method. The interference pattern technique relies on analyzing the interference diagram (main observable) generated by the interaction between the reflected and direct signals. In order to simplify the modeling of the interference pattern and to optimize signal reception, the receiving antenna is oriented horizontally (Fig. 1). This orientation results in a symmetrical antenna gain pattern, ensuring that signal differences arise solely from the surface. In addition, the antenna is linearly polarized (vertically) in the IPT for multiple reasons: (1) the need of simultaneous reception of both direct and reflected signals; (2) horizontal and vertical components exhibit more variations with the

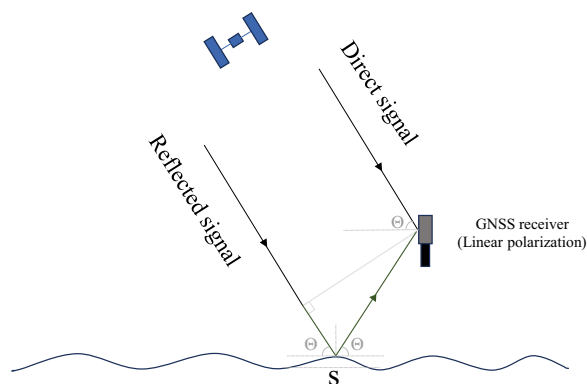


**Fig. 1** Single-antenna GNSS-R geometry for the IPT method. From <https://tel.archives-ouvertes.fr/tel-01417284>

angle of incidence  $\theta$  than the Right-Hand Circular Polarization (RHCP) and Left-Hand Circular Polarization (LHCP) components, making the linear polarization more sensitive to interactions between the reflecting surface and the RHCP wavelengths; and (3) the combination of direct and reflected signals at the antenna generates both positive and negative interferences. The interference pattern varies with the angle of incidence  $\theta$  as the launching satellite moves. The Brewster angle generates a singularity (notch) in the interference pattern, resulting in a minimum observable amplitude in the signal's oscillations. The position and amplitude of the notch are two parameters that reflect surface properties and can be used to retrieve surface properties. The fluctuations in the amplitude of both polarizations increase with increasing SMC, and v-polarization is more sensitive to SMC than h-polarization. Meanwhile, the notch position and amplitude of v-polarization are both sensitive to SMC.

Using the IPT equation, the maxima  $P_{qmax}$  and minima  $P_{qmin}$  power values can then be obtained as (Rodriguez-Alvarez et al., 2009; Arroyo et al., 2014):

$$P_{qmax}(\theta, \varepsilon) = F_n(\theta) \cdot |E_{0i}|^2 \cdot |1 + |R_p(\theta, \varepsilon)||^2 \tag{5}$$

$$P_{qmin}(\theta, \varepsilon) = F_n(\theta) \cdot |E_{0i}|^2 \cdot |1 - |R_p(\theta, \varepsilon)||^2 \tag{6}$$

where  $\theta$  is the elevation angle,  $F_n(\theta)$  is the antenna radiation pattern,  $E_{0i}$  is the incident electric field amplitude, and  $R_p(\theta, \varepsilon)$  is the Fresnel reflection coefficient at  $p$  polarization. Then, the total reflection coefficient of the entire interference pattern at  $p$  polarization can be expressed as (Arroyo et al., 2014):

$$\left| \widehat{R}_p(\theta, \varepsilon) \right| \approx \frac{\sqrt{\frac{P_{qmax}(\theta, \varepsilon)}{P_{qmin}(\theta, \varepsilon)} - 1}}{\sqrt{\frac{P_{qmax}(\theta, \varepsilon)}{P_{qmin}(\theta, \varepsilon)} + 1}} \tag{7}$$

where the reflection coefficient is a function of the elevation angle  $\theta$  and the soil dielectric constant  $\varepsilon$ .  $\left| \widehat{R}_p(\theta, \varepsilon) \right|$  is the amplitude estimator using the Fresnel Reflection coefficient at different elevation angles at  $p$  polarization (Arroyo et al., 2014). Thus,  $\left| \widehat{R}_p(\theta, \varepsilon) \right|$  is linked to the soil moisture content at different  $\theta$  values.

For the multipath method (Fig. 2), since  $h$  is the antenna height and  $SNR_r$  is a periodic function of the carrier phase, it can be expressed as:

$$SNR_r = A_r \cos \left( \frac{4\pi h}{\lambda} \sin(\theta) + \psi_r \right), \tag{8}$$

where  $A_r$  is the combination of the reflected power and gain pattern, proportional to the reflected power from



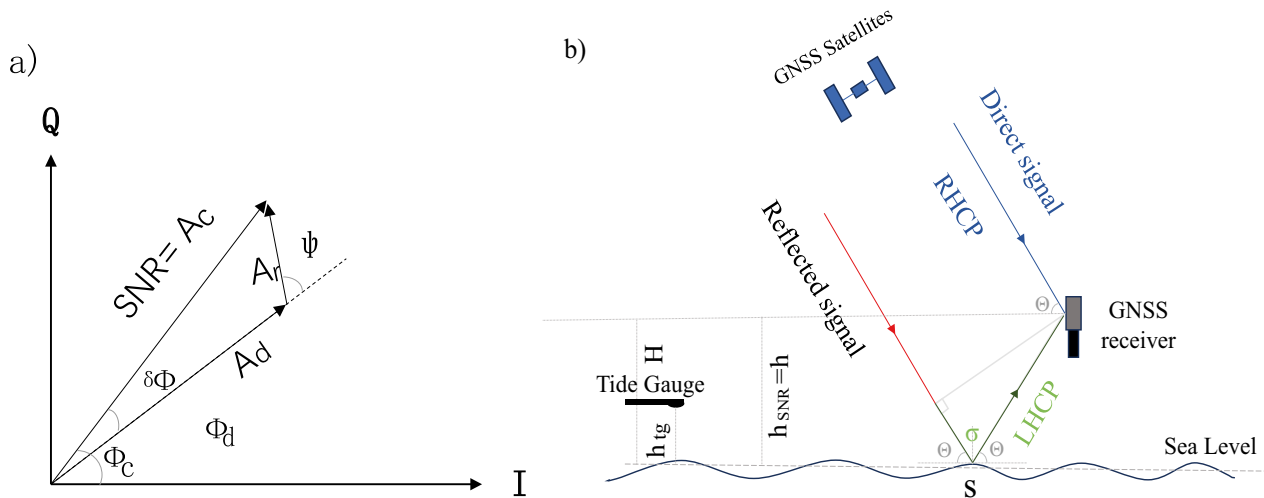


**Fig. 2** a Displays the phasor diagram of the received GNSS signal with demonstrating the relationships between the components in quadrature (Q) and phase (I) of the signal. b The geometry of the omnidirectional single antenna GNSS-R receiver. From <https://tel.archives-ouvertes.fr/tel-01417284>

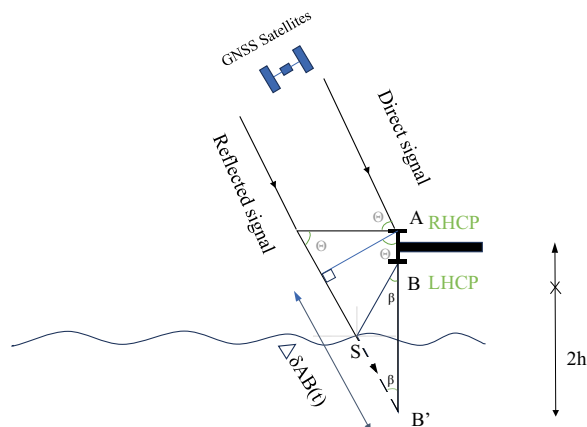


**Fig. 3** Geometry of a dual-antenna GNSS-R. From <https://tel.archives-ouvertes.fr/tel-01417284>

the ground, and  $\psi_r$  is the phase. Both depend on the angle of incidence  $\theta$ .

Changes in soil moisture can be estimated by analyzing temporal fluctuations in the phase of SNR data for direct and reflected signals.

**GNSS-R dual antennas**

In general, receivers equipped with dual antennas capturing direct signals through an RHCP antenna oriented to the zenith, while the reflected signals are captured using an LHCP antenna, with each signal’s power measured independently (Fig. 3). Three types of observing systems are feasible, depending on the antenna configuration:

An up-looking RHCP paired with a down-looking LHCP antenna receives the direct and surface-reflected signals, respectively. The reflectivity ( $\Gamma_0$ ) can be determined either by using the ratio of the reflected signal to the direct signal (Gleason et al., 2005), or through a bistatic radar equation (Masters et al., 2004). Subsequently,  $\epsilon$  can be retrieved from  $\Gamma_0$  using a surface roughness parameter within a specific scattering model (Ulaby et al., 1982). These observations are influenced by  $\epsilon$ ,  $\theta$ , and the surface roughness.

A configuration featuring one upward-looking antenna (RHCP) and two downward-looking antennas (one RHCP and one LHCP) enables measurement of both cross-polarized and co-polarized components of  $\Gamma_0$  (Zavorotny & Voronovich, 2000). SMC is anticipated to correlate well with the ratio of the two  $\Gamma_0$ , independent of the effect of the surface roughness.

For horizontal and vertical polarizations, the ratio of reflected to direct power can be expressed as a function of the surface roughness and soil reflectivity  $\Gamma_0$ . The effect of surface roughness can be mitigated by utilizing the orthogonal polarization power ratio. This demonstrates its applicability across a broad range of roughness, by retrieving the dielectric constant through the ratio of power densities scattered at  $hh$  and  $vv$  polarizations at different angles of incidence  $\theta$ . To improve the calculation of  $\epsilon$ , assuming that the ratio is a function of  $\epsilon$  and  $\theta$ , it is necessary to measure at least two different  $\theta$  using the least squares method (Jia et al., 2019).

In all the three cases, the DDM is the basic observable when using the GNSS-R dual antenna configuration:

$$\langle |Y(\tau, f)|^2 \rangle = \frac{T_i^2 P_t G_t \lambda^2}{(4\pi)^3} \iint_A \frac{G_r(\bar{\rho})}{R_0^2(\bar{\rho}) R^2(\bar{\rho})} \sigma_{pq}^0 x^2(\bar{\rho}, \delta\tau, \delta f) d\bar{\rho} \quad (9)$$

The DDM represents the power of the signal as depicted in this equation. Across various points on the observation surface, the DDM illustrates the contributions of each  $\tau$  and  $f$ . The bistatic radar coefficient ( $\sigma^0$ ) is subsequently estimated from the peak of the reflected signal waveform. On smooth surfaces, the coherent component is significant and could be estimated through the direct signal, the Fresnel reflection coefficient ( $R$ ), and a rough term depending on  $\theta$ :

$$\langle |Y(\tau, f)|^2 \rangle_{spec} = |Y_0(\tau, f)|^2 |R| e^{-8\pi^2 \sigma_h^2 \cos^2(\theta) / \lambda^2}. \quad (10)$$

This method is predominantly used for oceanic studies and SMC measurements. Subsequently, the surface reflectivity ( $\Gamma_0$ ) can be estimated by the ratio of the reflected to direct signal. For this approach, the Doppler shifts of both reflected and direct signals are assumed to be identical, with an additional delay accounting for the reflected signal due to the measurement geometry. The corresponding equation can be expressed as:

$$\Gamma_{pq} = \left| \left\langle \frac{Y_{r,q}(\Delta\tau, f)}{Y_{d,p}(0, f)} \right\rangle \right|^2. \quad (11)$$

where  $\langle \rangle$  represents the average operator,  $\Delta\tau$  denotes the delay between direct and reflected signals,  $Y_{d,p}$  is the correlation of the direct signal with the polarization  $p$ , and  $Y_{r,q}$  is the correlation of the reflected signal with polarization  $q$ . The Interferometric Complex Field (ICF) constitutes another observable, defined as the time series representing the maximum ratio of the reflected signal to the direct signal:

$$ICF(t) = \frac{Y_{r,q}(i, \Delta\tau, f)}{Y_{d,p}(t, 0, f)} = \frac{R(t)}{D(t)} = \frac{r(t)}{d(t)} e^{-i(\phi_r(t) - \phi_d(t))}, \quad (12)$$

where  $R(t)$  and  $D(t)$  represent the maxima of the waveforms in the time series, and  $r(t)$ ,  $d(t)$ ,  $\phi_r$ , and  $\phi_d$  are denoted as the amplitude and corresponding phase. The ICF serves as an indicator of surface roughness, dielectric properties, and SMC characterization (Alonso-Arroyo et al., 2014).

### Observations and missions

Ground-based observations, airborne platforms, and spaceborne GNSS-R missions constitute the three types of missions. In the case of ground-based platforms, either two antennas are utilized to separately receive the direct and reflected signals, or a single antenna is

employed to capture both signals, while in the case of aircraft or satellite platforms, only the dual antenna is employed.

### Ground GNSS-R observations

Several ground-based experiments have demonstrated the GNSS-R's sensitivity to geophysical parameters such as soil moisture, snow depth, biomass content, sea surface height, sea ice, surface mean square slope, and wind speed (Chew et al., 2016; Edokossi et al., 2020; Qian & Jin, 2016; Yan & Huang, 2019c; Alonso-Arroyo et al., 2017). In fact, multipath effects of ground-based GNSS receivers have been demonstrated in many studies and utilized to retrieve soil moisture and biomass content (Chew et al., 2016; Zavorotny et al., 2009). The IPT was employed to retrieve SMC (Mironov et al., 2012; Rodriguez-Alvarez et al., 2009, 2010) and Arroyo et al. (2014) demonstrated a dual-polarization GNSS-R IPT capability to increase the soil moisture estimate accuracy. Ground-based experimental campaign, the Land MOnitoring with Navigation Signals (LEiMON), was conducted by Egido et al. (2012) to enhance the accuracy of the reflectivity measurements. Soulat et al. (2004) tested ground-based GNSS observations to retrieve sea state (surface mean square slope and wind speed). The sea surface height was retrieved using the ground-based GNSS-R (Cardellach et al., 2011; Jin et al., 2017a; Ribot et al., 2014; Ruffini et al., 2004). In 2013, Beihang University, China Meteorological Administration (CMA) and ESA conducted the first typhoon observation using coastal GNSS-R (Typhoon Investigation using GNSS-R Interferometric Signals, TIGRIS) in Yangjiang and Shenzhou, Guangdong, China (Li et al., 2014a, b; Martín et al., 2014).

### Airborne GNSS-R experiments

GNSS-R dual antenna is mostly used in airborne missions and several missions have demonstrated the capability of airborne observations for parameters retrieval (Jia et al., 2016; Katzberg et al., 2006a; Klemas et al., 2014; Martin et al., 2011; Masters et al., 2004; Motte et al., 2016; Troglia Gamba et al., 2015). Soil moisture content was extracted from airborne experiments (Katzberg et al., 2006b; Masters et al., 2004). Egido et al. (2014) used low-altitude airborne to perform polarimetric measurements of SMC, and Motte et al. (2016) introduced the GLOBal navigation satellite system Reflectometry Instrument (GLORI) to retrieve soil moisture, vegetation water content, forest biomass content, and in-land water bodies. Frappart et al. (2021), Jia (2018), and Troglia Gamba et al. (2015) employed airborne technique for in-land water body surface detection. Ribot et al. (2014) used experimental airborne campaigns for retrieving sea

surface height. Cardellach et al. (2003) and Garrison et al. (2002) employed airborne field campaigns to retrieve sea state parameters. Ocean wind speed and surface roughness were recently studied using DDM observables from a receiver mounted on an aircraft. Aircraft experiments for sea and freshwater ice conditions and the freeze/thaw state of frozen ground were described in Komjathy et al. (2000).

**Spaceborne GNSS-R missions**

The UK Disaster Monitoring Constellation (UK-DMC) satellite represented the first spaceborne GNSS-R mission, launched in 2003, followed by the UK TechDemoSat-1 mission in 2014, and NASA’s CYGNSS with a small 8-satellite constellation in 2016. Bufeng-1 A/B is the first Chinese GNSS-R mission, while FY-3/GNOS-II operated by China Meteorological Administration is the first operational mission launched in 2021 that combines GNSS-R and GNSS radio occultation using multiple GNSS constellations. Spire CubeSats and ESA FSSCAT CubeSats have also been successfully launched since 2019. Additionally, the ESA Passive REflecTomeTry and dosimetrY (PRETTY) satellite (for GNSS-R altimetry) was launched in October 2023, and the NASA Signals of Opportunity P-band Investigation (SNOOPI) mission (first reflectometry mission at P-band) is expected to be launched in 2024. The Hydrological Global Navigation

Satellite System (HydroGNSS) is planned to be launched in 2025 by ESA and targets to collect data on the hydrological climate variables. 3CAT-2 was an Experimental Nano-Satellite for GNSS-R Earth Observation developed by Universitat Politècnica de Catalunya (UPC). GNSS-R spaceborne missions are summarized in Table 1.

**Status and advances**

**Instruments**

Currently, the cGNSS-R, L1/LHCP, and GPS are the most common configurations used even though iGNSS-R offers improved accuracy in ocean altimetry products. The next generation of GNSS-R instruments is currently being developed to expand upon the capabilities of the SGR-ReSI instrument in NASA’s CYGNSS mission (Ruf et al., 2016). This instrument operates on the low (L1/E1) and high (L5/E5) bandwidth signals of GPS and Galileo satellites, while CYGNSS uses only the GPS L1 signal (Ruf et al., 2016). Table 2 summarizes the characteristics of ground-based, air-borne, and space-borne GNSS-R instruments.

**Ocean altimetry**

GNSS-Reflectometry was first used to study ocean altimetry or sea surface height. Martin-Neira (1993) first proposed the concept of the PARIS. GNSS-R altimetry facilitates the detection of the height difference between

**Table 1** GNSS-R spaceborne missions and instruments. Left- and Right-Hand Circular Polarization (L/R-HCP)

| Mission  | Launched date | GNSS-R type                   | Band/Pol used                    | GNSS constellations              |
|--|---------------|-------------------------------|----------------------------------|----------------------------------|
| UK-DMC (Gleason et al., 2005)                    | 2003          | cGNSS-R                       | L1 / LHCP                        | GPS                              |
| UK-TDS-1 (Unwin et al., 2016)                    | 2015          | cGNSS-R                       | L1 / LHCP                        | GPS                              |
| CYGNSS (Ruf et al., 2016)                        | 2016          | cGNSS-R                       | L1 / LHCP                        | GPS                              |
| 3Cat-2 (Carreno-Luengo et al., 2016)             | 2016          | cGNSS-R<br>rGNSS-R<br>iGNSS-R | L1, L2 / LHCP, RHCP              | GPS<br>GLONASS<br>Galileo<br>BDS |
| SMAP GNSS-R (Carreno-Luengo et al., 2017)        | 2017          | cGNSS-R                       | L2 / H, V                        | GPS                              |
| BuFeng-1 A/B (Jing et al., 2019)                 | 2019          | cGNSS-R                       | L1 / LHCP                        | GPS<br>BDS                       |
| Spire series (Masters, 2019)                     | 2019          | cGNSS-R                       | L1 / LHCP                        | GPS<br>Galileo                   |
| Fengyun-3 series (Sun et al., 2023)              | 2021          | cGNSS-R                       | L1 / LHCP                        | GPS<br>Galileo<br>BDS            |
| 3Cat-5 A/B (FSSCat mission) (Camps et al., 2022) | 2020          | cGNSS-R                       | L1 / LHCP                        | GPS<br>Galileo                   |
| 3Cat-4 (J. F. Munoz-Martin et al., 2018)         | 2021          | cGNSS-R                       | L1, L2 / LHCP                    | GPS<br>Galileo                   |
| Pretty (Dielacher et al., 2019)                  | 2022          | iGNSS-R<br>cGNSS-R            | L5 / RHCP                        | GPS<br>Galileo                   |
| TRITON (Juang et al., 2016)                      | 2023          | cGNSS-R                       | L1/LHCP                          | GPS                              |
| HydroGNSS (Unwin et al. 2021)                    | 2025          | cGNSS-R                       | L1/LHCP + RHCP<br>L5/LHCP + RHCP | GPS<br>Galileo                   |

**Table 2** Available information on existing GNSS-R receivers. Types of GNSS-R instruments include S for Spaceborne, A for Airborne, and G for Ground-based. GPS-IR represents GPS Interferometric Reflectometry

| ID   | HW/ SW | Number RF Port | Frequency Bands              | BB Bandwidth (MHz)  | Sampling Rate (MHz) | Output Rate (Hz) | Receiver Technique       | GNSS Constellation          | Type    |
|--|--------|----------------|------------------------------|---------------------|---------------------|------------------|--------------------------|-----------------------------|---------|
| GORS-1(2) (Helm et al., 2007)                            | HW     | 2 (4)          | L1, L2                       | –                   | –                   | –                | cGNSS-R (C/A, L2C)       | GPS, Galileo                | G, A    |
| TR   | SW     | 2              | L1, L2                       | –                   | –                   | –                | Raw                      | GPS                         | G       |
| BJ   | SW     | 4              | L1, L2                       | 18                  | 20                  | 20,000           | Raw                      | GPS                         | G       |
| TriG (extended)  | HW     | 8 (16)         | Any 4 within L band          | 2 to 40 config      | 20/40               | 0.1–1000         | Any: software config     | GPS, GLONASS Galileo        | G       |
| OceanPal/SAM   | SW     | 2              | L1                           | 4                   | 16.367              | 1000             | Raw                      | GPS                         | G       |
| OpenGPS (Helm, 2008)                                     | HW     | 2              | L1                           | –                   | 5.7                 | < 1000           | cGNSS-R (C/A)            | GPS                         | G       |
| COMNAC   | SW     | 1              | L1                           | –                   | 5.7                 | –                | Raw                      | GPS                         | G       |
| Ublox LEA-4T   | HW     | 1              | L1                           | 2                   | 4                   | –                | cGNSS-R (C/A)            | GPS                         | G       |
| NordNav  | SW     | 1(4)           | L1                           | 2                   | 16.4                | –                | Raw                      | GPS                         | G       |
| GRAS   | HW     | 3              | L1, L2                       | 20                  | 28.25               | 1000             | cGNSS-R (C/A)            | GPS                         | G       |
| DMR (Unwin et al., 2013)                                 | HW     | 4              | L1, L2                       | 4                   | 16                  | variable         | cGNSS-R, raw             | GPS                         | S       |
| SGR-ReSI-Z   | HW     | 6              | L1, L5                       | 4 at L1<br>20 at L5 | 49.6                | 1                | cGNSS-R, raw             | GPS Galileo                 | S       |
| NGRx (C. Ruf et al., 2020)                               | HW     | 20             | L1, L5                       | 32                  | 65                  | variable         | cGNSS-R, raw             | GPS, Galileo, other         | S       |
| POLITO-GNSS-R  | SW     | 1              | L1                           | –                   | 8.1838              | –                | Raw                      | GPS                         | G       |
| GRIP-SARGO   | HW     | 2              | L1, L5, E1, E5               | 52                  | ≤ 150               | 1                | cGNSS-R                  | GPS Galileo                 | G       |
| GLORI (Motte et al., 2016)                               | SW     | 4              | L1                           | 4                   | 16.4                | –                | cGNSS-R                  | GPS                         | A       |
| GOLD-RTR (Nogués-Correig et al., 2007)                   | HW     | 3              | L1                           | 8                   | 20                  | 1000             | cGNSS-R (C/A)            | GPS                         | G, A    |
| PIR/A (Rius et al., 2012)                                | HW     | 3              | L1                           | 12                  | 80                  | 1000             | iGNSS-R                  | Any at L1                   | G, A    |
| SPIR (Ribó et al., 2017)                                 | SW     | 16             | L1, L5                       | 80                  | 40                  | 40,000           | Raw                      | Any at L1, L5               | G, A    |
| SPIR-UAV   | SW     | 8              | L1, L5                       | 80                  | 40                  | 40,000           | Raw                      | Any at L1, L5               | A       |
| DODEREC (Nogués et al., 2003; Nogues-Correig, 2002)      | HW     | 3              | L1                           | –                   | 20.46               | –                | cGNSS-R (C/A)            | GPS                         | G       |
| SMIGOL (Rodríguez-Alvarez et al., 2009)                  | HW     | 1              | L1                           | 2.2                 | 5.745               | 1                | GPS-IR (C/A)             | GPS                         | G       |
| PYCARO (Carreno-Luengo et al., 2014; Olivé et al., 2016) | SW     | 2              | L1, L2                       | 20                  | > 100 MHz           | Tc and Ti config | cGNSS-R, rGNSS-R iGNSS-R | GPS, GLO-NASS, Galileo, BDS | G, A, S |
| PYCARO-2   | SW     | 2              | L1, L2, L5 B1, B2, B3 E1, E5 | 50                  | > 100 MHz           | 1                | cGNSS-R, rGNSS-R         | GPS, GLO-NASS, Galileo, BDS | G       |
| MIR (Onrubia et al., 2019)                               | HW/SW  | 2              | L1, L5                       | 24                  | 32.736 (×2)         | Tc and Ti config | Raw                      | GPS Galileo                 | G, A    |



**Table 2** (continued)

| ID                                    | HW/ SW | Number RF Port | Frequency Bands | BB Bandwidth (MHz) | Sampling Rate (MHz) | Output Rate (Hz)          | Receiver Technique         | GNSS Constellation                | Type |
|---------------------------------------|--------|----------------|-----------------|--------------------|---------------------|---------------------------|----------------------------|-----------------------------------|------|
| FMPL-1<br>(Munoz-Martin et al., 2018) | HW/SW  | 2              | L1, L2          | 2                  | 4.096               | Tc and Ti config          | cGNSS-R                    | GPS                               | S    |
| FMPL-2<br>(Munoz-Martin et al., 2020) | HW/SW  | 2              | L1, E1          | 2.4                | 4.096               | Tc = 1 or 4 ms; Ti config | cGNSS-R                    | GPS L1 C/A Galileo E1             | S    |
| FMPL-3                                | HW/SW  | 2              | L5 E5a          | 24                 | 10.230              | Tc and Ti config          | cGNSS-R                    | GPS L5 Galileo E5a                | S    |
| GENESIS (Qiu et al., 2023)            | HW     | 16             | All L-band      | –                  | 2–40 I/Q config     | 1000                      | cGNSS-R, GNSS-RO, GNSS-PRO | All GNSS and SBAS, ≥ 2 freq. each | A, S |
| GRrSv.3 (Xing et al., 2022)           | HW     | 4              | L1, B1          | 4                  | 16.369              | 1000                      | cGNSS-R                    | GPS BDS                           | G    |
| GNOS-II (Sun et al., 2019)            | HW     | 8              | L1, B1, E1      | 8                  | 4.096               | 1                         | cGNSS-R                    | GPS BDS Galileo                   | S    |

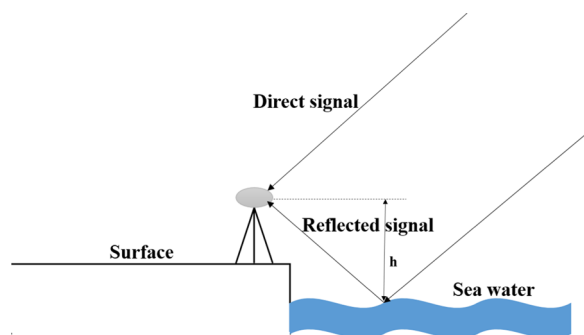


**Fig. 4** Geometry of GNSS-R altimetry. *h* is the antenna height from the reflected surface (Jin et al., 2017a)

the receiver and the reflecting surface. The distances between the transmitter, receiver, and/or surface are the observables to be considered in the measurement (Cardellach et al., 2011) as it is shown in Fig. 4. Perfectly flat surfaces such as water or ice can be considered for altimetry measurement (Fabra et al., 2011; Hajj & Zuffada, 2003). The circular regression technique referred to as carrier phase altimetry is more precise than the group delay altimetry (code delay) technique (Kucwaj et al., 2017).

Radar altimetry considered as the primary spaceborne sea surface observation technology, is constrained by the mode of sub-satellite observation, suitable only for features on scales larger than 400 km (Fu et al., 2010). GNSS-R is an effective technique that overcomes this limitation and facilitates the observation of small- to medium-scale and submesoscale sea surface heights with enhanced spatial and temporal resolution (Clarizia & Ruf, 2016). UK-DMC launched in 2003 and equipped

with GNSS-R receiver, demonstrated its feasibility for altimetry technique. TDS-1 was launched in July 2014, and could output the delay-Doppler maps (DDMs) (Unwin et al., 2016). NASA’s CYGNSS mission employed an improved receiver to monitor ocean wind speed (Ruf et al., 2012). Thanks to the advances in GNSS-R technology, the Delay–Doppler Mapping Instrument (DDMI) can also process the signals transmitted by GPS, Galileo, and BDS.

To date, the only launched space mission dedicated to altimetry is ESA’s PRETTY mission. It operates at L5, the longest of the GNSS wavelengths, approximately 25 cm, to maximize coherence over the sea surface and the sea ice when observed at grazing elevation angles (below some 15°). The 3U CubeSat is pointed in such a way that the RHCP GNSS-R antenna, attached to one of its faces, looks towards the limb of the Earth. Both the direct and the reflected signals are received through the same antenna. When a coherent reflection occurs, carrier-phase-based precise altimetry can be performed. Otherwise, a less precise group delay altimetry is carried out. From the carrier-phase observations centimeter-level precision altimetric profiles can be extracted. To convert those profiles into absolute height the carrier-phase ambiguity must be solved or, alternatively, an auxiliary observation needs to be ingested. Group delay measurements provide absolute heights directly, after correcting for atmospheric effects.

**Ocean wind**

When the wind blows, the sea surface becomes rough under the wind-generated waves. The GNSS satellite signal illuminates the rough sea surface and undergoes

diffuse reflection. The peak value and shape of the DDM or delay waveform are closely linked to the wind speed and the sea surface’s roughness. As wind speed increases, the sea surface comes rougher, approaching diffuse reflection, which results in a smaller peak value of the DDM or delay waveform and flatter waveform edges. Conversely, the closer proximity to specular reflection yields a larger peak value and steeper waveform edges. Therefore, ocean wind speed can be retrieved by the DDM or delay waveform.

**Bistatic radar equation**

Based on Kirchoff Approximation to Geometric Optics (KA-GO), the expectation of DDM can expressed as an integral of the glistening area (Zavorotny & Voronovich, 2000):

$$|Y(\tau, f)|^2 = \frac{\lambda^2 P_t G_t}{(4\pi)^3} \iint \frac{G_r(\vec{\rho}) \Lambda^2(\Delta\tau) S^2(\Delta f)}{R_t^2(\vec{\rho}) R_r^2(\vec{\rho})} \sigma_0(\vec{\rho}) d(\vec{\rho}) \tag{13}$$

where the left side of the equation indicates the correlated power value between the reflected signal component, characterized by delay size  $\tau$  and Doppler frequency  $f$ , and the local pseudo-random code of the receiver in the GNSS multipath reflected signal. This side typically utilizes the relative values of signal delay and Doppler frequency in reference to the specular reflection point. The symbols of the  $\langle \rangle$  operation indicate the averaging or expectation;  $\lambda$  on the right side of the equation is the GNSS signal carrier wavelength;  $P_t$  and  $G_t$  are the GNSS satellite transmitting power and antenna gain.  $P_t G_t$  represents the Effective Isotropic Radiated Power (EIRP) of the GNSS satellite, which usually varies not much in the sea surface area integrating around the specular point;  $G_t$  is the gain of the transmit antenna;  $\Lambda^2(\Delta\tau) S^2(\Delta f)$  is the Woodward Ambiguity Function (WAF) of the GNSS-R bistatic radar describing the selection of the correlation power with respect to the Doppler frequency and the time delay;  $\vec{\rho}$  represents the position of each point on the sea surface;  $R_t$  and  $R_r$  represent the distances from the specular point to the transmitter and receiver, respectively;  $\sigma^0$  is the GNSS-R normalized bistatic scattering cross-section, which is related to the wind speed and can be expressed as:

$$\sigma_0 = \pi |\mathfrak{R}|^2 P \left( -\frac{\vec{q}_\perp}{q_z} \right) \frac{\vec{q}^4}{q_z^4} \tag{14}$$

where  $\mathfrak{R}$  is the Fresnel reflection coefficient,  $\vec{q}$  is the bisector,  $q_z$  and  $q_\perp$  are the vertical and horizontal components, and  $P()$  symbolizes the PDF of the sea surface slope, commonly assumed to follow a Gaussian distribution as a function of mean square slope:

$$P(\vec{s}, m) = \frac{1}{2\psi_{sx}\sigma_{sy}\sqrt{1-b_{x,y}}} \exp \left[ -\frac{1}{2(1-b_{x,y}^2)} \left( \frac{s_x^2}{\sigma_{sx}^2} - 2b_{x,y} \frac{s_x s_y}{\sigma_{sx}\sigma_{sy}} + \frac{s_y^2}{\sigma_{sy}^2} \right) \right] \tag{15}$$

By assuming a 0° wind direction, the PDF can simplified to be:

$$P(\vec{s}, m) = \frac{1}{2\pi m} \exp \left( -\frac{|\vec{s}|^2}{2m} \right) \tag{16}$$

where  $\vec{s} = -\frac{\vec{q}_\perp}{q_z}$  denotes the surface slope and  $m$  is the mean square slope. The mean square slope can be related to the wind speed by a wind spectrum (Zavorotny & Voronovich, 2000) or an empirical model (Katzberg et al., 2006a).

**Observables**

As wind speed is related to the magnitude and shape of the DDM or delay waveform, for simplifications, the observables can be extracted from the DDM and a geophysical model function can be trained for the relationship between the observable and wind speed. There are a large number of observables, among which the most commonly used ones are the Normalized Bistatic Radar Cross-Section (NBRCS) and Leading-Edge Slop (LES), especially for spaceborne missions.

Assuming that the geometry and power terms are the same as the ones at the specular point, the bistatic radar equation can be simplified to be:

$$\langle |Y(\tau, f)|^2 \rangle = \left[ \frac{P_t G_t}{(4\pi R_t^2)} \right] \left[ \frac{\sigma_0 A_{eff}}{(4\pi R_r^2)} \right] \left[ \frac{\lambda^2 G_r}{(4\pi)} \right] \tag{17}$$

where  $A_{eff} = \iint \Lambda^2(\Delta\tau) S^2(\Delta f) ds$  is the effective scattering area at the specular point. The Bistatic Radar Cross-Section (BRCS) can be calculated as:

$$\sigma = \sigma_0 A_{eff} = \langle |Y(\tau, f)|^2 \rangle \left\{ \left[ \frac{P_t G_t}{(4\pi R_t^2)} \right] \left[ \frac{1}{(4\pi R_r^2)} \right] \left[ \frac{\lambda^2 G_r}{(4\pi)} \right] \right\}^{-1} \tag{18}$$

The NBRCS,  $\sigma_0$  is computed as the BRCS normalized by the effective scattering area:

$$\sigma_0 = \frac{BRCS}{A_{eff}} \tag{19}$$

To reduce noise, the NBRCS can be extended to the Delay-Doppler Map Average (DDMA), which is the average of NBRCS for several DDM bins in proximity to the specular point. The averaging area is determined by the

requirement of the spatial resolution. For example, the averaging box for CYGNSS limited by the 25-km resolution is 3 delay bins times 5 Doppler bins.

The LES is defined as the slope of the leading edge for the integrated delay waveform. The integrated delay waveform is the averaged delay waveform for several Doppler bins. The LES can be computed by the least square fitting method:

$$\text{LES} = \frac{m \sum_{i=1}^m x_i y_i - \sum_{i=1}^m x_i \sum_{i=1}^m y_i}{m \sum_{i=1}^m x_i^2 - (\sum_{i=1}^m x_i)^2} \quad (20)$$

where  $m$  is the number of fitting points, and  $(x_i, y_i)$  is the coordinate of points.

### Retrieval algorithm

Wind speed retrieval based on the observables and GMF is the most mature method up to now as it is easy to implement. For airborne cases, there are a large number of observables based on the shape and power of the DDM (Li et al., 2023; Rodriguez-Alvarez et al., 2013). However, for spaceborne missions, limited by the spatial resolution, usually only a small part of the DDM can be used for retrieval, and thus the DDM power magnitude is more sensitive to wind speed rather than the shape.

There are various methods for the training of the GMF. It can be trained by generating a set of look-up tables (LUT) (Clarizia et al., 2014) or non-linear fitting (Ruf & Balasubramaniam, 2018). The training is usually implemented by different incidence angles. Because of the non-linear relationship between the observables and wind speed, and the difference in sea state, the GMF can also be trained for low and high wind speeds separately (Ruf & Balasubramaniam, 2018). Some statistical methods have been proposed for the training and show good results (Clarizia & Ruf, 2020; Guo et al., 2021; Wu et al., 2022). Some optimization methods can be used to additionally enhance the retrieval accuracy. A minimum variance estimator can be used to aggregate the results of multiple observables to improve accuracy (Clarizia et al., 2014). Significant wave height (SWH) information was found to be useful in correcting the sea state effect and showing improvement in wind speed retrieval, especially at low wind speeds (Clarizia & Ruf, 2017; Pascual et al., 2021). A track-wise bias correction method can effectively correct the bias in the estimated transmitting power and antenna pattern and show great improvement, although pre-knowledge wind speed information from a numerical weather prediction (NWP) model is required. Generally, the wind speed error of well-calibrated GNSS-R observations is around 1.5 m/s when compared to NWP models or other satellite observations, and 1.2–1.5 m/s with extra

optimizations (Clarizia & Ruf, 2020; Huang et al., 2022) under low to medium wind speeds.

The second type of retrieval method is based on waveform fitting using a physical model. This method has been widely used for airborne cases and even wind direction can be retrieved (Yang et al., 2022; Zhang et al., 2024). However, it is difficult to apply for spaceborne cases as the footprint of the DDM can cover an area of over 100 km. Huang et al. (2019; 2020) proposed a method based on a physical DDM forward model that creates a grid of wind fields in the glistening zone, and then the wind speed at each grid can be inverted by sequential DDMs using the physical model and extended Kalman filter. A swath of wind field can be retrieved when compared to traditional a track of wind speeds at specular points. Similarly, Cardellach et al. (2020) proposed a method using a physical model and variational assimilation method, which shows better retrieval results at high wind speeds when compared to traditional methods. However, currently, none of the methods above has been used operationally due to the complexity of implementation and computational cost.

The third type of retrieval method is based on machine learning (ML). There is a large bundle of ML-related methods in recent years (Liu et al., 2023; Reynolds et al., 2020). Machine learning (ML) has the advantage of extracting high non-linear relationships between a large number of variables. The input variables are usually not limited to observables that are used by traditional methods but also include multiple geometry and instrument terms such as incidence angle, antenna gain, and PRN code. Therefore, the ML method has the advantage of correcting potential calibration errors. Furthermore, some ML methods such as convolutional neural networks can extract information from the entire DDM (Arabi et al., 2023; Guo et al., 2021). The accuracy of most ML methods presents slightly better retrieval accuracy than GMF methods with RMSE under 1.5 m/s globally. However, the performance in the retrieval of high wind speeds is still challenging for both.

### Typhoon monitoring

Typhoon, as an extreme weather system, is a high-altitude cyclone phenomenon that often occurs in tropical and subtropical oceans. According to the different sea areas the typhoons have different names. When it occurs in the Northwest Pacific, it is generally called as typhoon, while those occurring in the Atlantic and East Pacific are commonly referred to as hurricanes. Vigorous cyclone often causes weather disasters, such as heavy rainfall, thunderstorms, strong winds, tornadoes, and hail. Those natural disasters are harmful to daily life, transportation, industrial, and agricultural production, therefore, have an

important influence on social activities. China has a long coastline located in the northwest Pacific Ocean. The China Meteorological Administration found that approximately 8–10 typhoons make landfall in China every year. The detection, estimation, and prediction of typhoons are a common concern for all societies. Especially, the accurate positioning of the typhoon center and the prediction of typhoon path are closely related to the forecast qualities of thunderstorms and the strong winds it brings. Therefore, accurate predictions of typhoon center positioning and typhoon path are the most important work in precise typhoon prediction and scientific analysis of disaster reduction.

GNSS-R serves as a passive remote sensing technique. The successes of numerous spaceborne GNSS-R missions, including UK-DMC, UK-TDS-1, CYGNSS, and BuFeng-1 A/B, alongside extensive airborne and ground-based experiments, underscores the huge potential of GNSS-R for measuring Earth surface parameters. In comparison with traditional remote sensing techniques, GNSS-R offers the advantage of low-cost and low-power observations. Once microsatellites are equipped to form a constellation, and high spatial and temporal resolution can be achieved on a global scale. Furthermore, GNSS-R’s operation at L-band makes it less susceptible to precipitation, rendering it particularly suitable for typhoon observations. Some studies have concentrated

on detecting and estimating typhoons using coastal, airborne, and spaceborne GNSS-R.

The first typhoon observation of coastal GNSS-R was conducted by Beihang University and ESA in Yangjiang and Shenzhou of Guangdong province, China, from July to September 2013 (Li et al., 2014a; Martín et al., 2014). During the experiment, the GPS and BDS reflected signals were acquired when the typhoons “Jebi” and “Utor” passed through the observation areas. Figure 5b shows the observable evolutions of the reflected signals from the BDS GEO satellite in time and frequency domains, as well as wind speed during the typhoon “Jebi” and “Utor”. There was a good correlation between the observables of the reflected signal and typhoon wind speeds, with the observed maximum wind speeds reaching up to 35 m/s (Li et al., 2016). After then, more observables sensitive to typhoon wind speed were proposed (Wang et al., 2016, 2019).

From 2000 to 2005, NASA’s Langley Research Center equipped the GPS reflection receiver on the NOAA Aircraft Operations Center (AOC) Hurricane Hunter P-3’s to acquire GPS reflected signals from several typhoons and tropical storms. The first retrieval of typhoon wind speed using airborne GNSS-R was performed on the data from the typhoon “Michael” (Katzberg et al., 2001). The analysis revealed that the received signal power levels were relatively strong, showing comparability to that observed at considerably

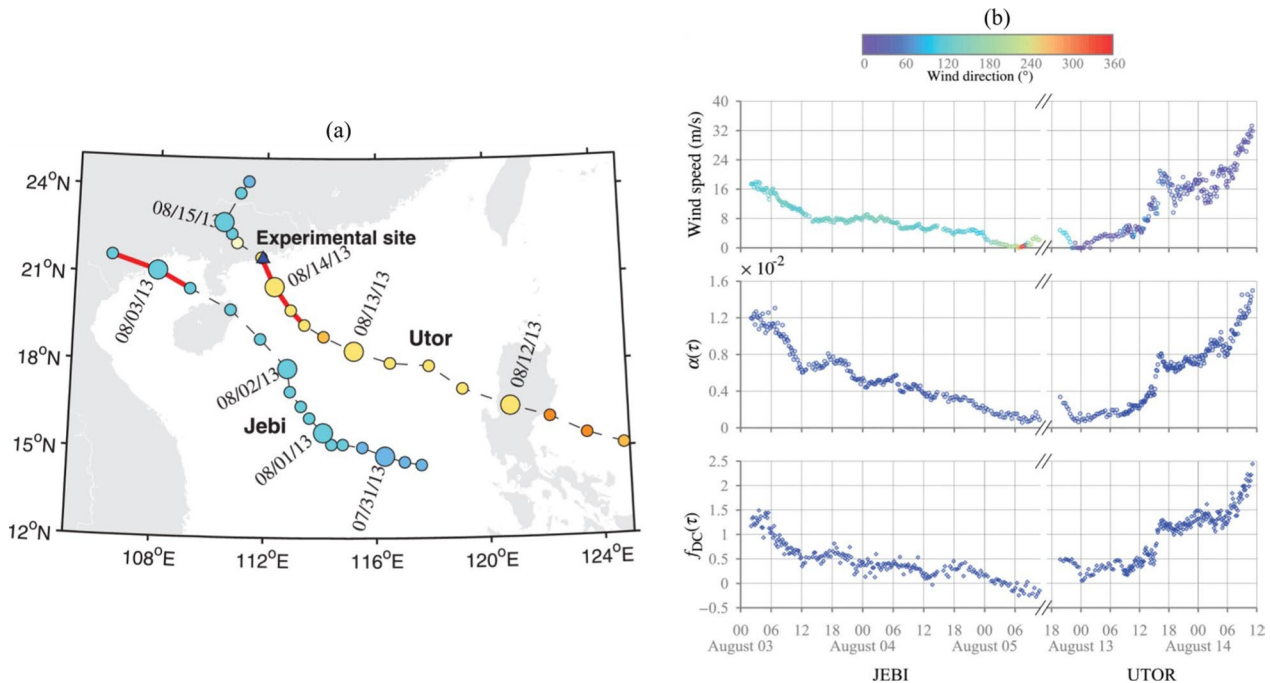


**Fig. 5** **a** The track history of the typhoons “Jebi” and “Utor”. The blue triangle marker indicates the location of the experimental site. **b** Comparison of sea surface wind speed and coastal GNSS-R observables in time and frequency domains during “Jebi” and “Utor” (Li et al., 2016)



lower wind speeds. A more detailed analysis and results were presented in Katzberg et al. (2006a), in which a simple function, as shown in Eq. (21), was developed to model the mean square slope with wind speed from tropical storms.

$$\begin{cases} \sigma_{\parallel} = 0.45 \cdot (0.000 + 0.00316 \cdot f(U)) \\ \sigma_{\perp} = 0.45 \cdot (0.003 + 0.00192 \cdot f(U)) \end{cases} \quad (21)$$

where  $\sigma_{\parallel}$  and  $\sigma_{\perp}$  are respectively mean square slope parallel and perpendicular to wind direction, and  $f(U)$  is a function of wind speed  $U$  as:

$$f(U) = \begin{cases} U & 0.00 < U \leq 3.49 \\ 6 \cdot \ln(U) - 4.0 & 3.49 < U \leq 46.00 \\ 0.411 \cdot U & 46.00 < U \end{cases} \quad (22)$$

This model is different from that of typhoon-free sea in (Cox & Munk, 1954), and has been widely used to model the mean square slope in the case of typhoons. This work also indicated that the retrieval approach designed for typhoon-free sea may be underestimated for high wind speed in the case of typhoons. A summary of wind speed retrieval using airborne GNSS-R during several typhoons was presented by Katzberg et al. (2013). The results indicated that reflected GPS signals could be utilized to observe sea surface wind speeds from near-zero to in excess of 40 m/s.

As compared to the studies of monitoring typhoons using coastal and airborne GNSS-R, more works were focused on detecting and measuring typhoons using spaceborne GNSS-R through theoretical simulation and analyzing actual data from in-orbit spaceborne missions. Two types of works have been focused on typhoon measurement. One work was to accurately retrieve typhoon

wind speed. Foti et al. (2017) firstly processed the data from TDS-1 passing through typhoons and preliminarily demonstrated that spaceborne GNSS-R could be employed to retrieve typhoon wind speed. The sensitivity of the CYGNSS observables to typhoon wind speed was examined by Guan et al. (2019), and it was found that CYGNSS-derived wind speed exhibited similar behavior to ASCAT, WindSat, and SMAP data juxtaposed around the eye of Typhoon "Irma", albeit underestimated at high wind speed. The relationships between the CYGNSS observables and wind speeds of both Fully Developed Sea (FDS) and Young Sea/Limited Fetch (YSLF) were explored (Ruf & Balasubramaniam, 2018). The results found that, as shown in Fig. 6, the dependency of the observables on wind speed varies between tropical cyclones and FDS conditions. The dependence of DDMA and LES on wind speed is independent of the sea state when wind speed is below 10 m/s. Above 10 m/s, the wind speed dependence of the DDMA and LES in YSLF conditions progressively diverges from those in FDS conditions (Wang et al., 2023). The different dependencies of the spaceborne GNSS-R observables on wind speed of FDS and YSLF conditions indicate that a special retrieval model of typhoon wind speed should be developed, such as in Ruf & Balasubramaniam (2018) and Wang et al. (2023). To improve the accuracy of retrieving typhoon wind speed, some novel algorithms were also proposed and tested. As an example, Huang et al. (2019, 2020) introduced extended Kalman filtering and data assimilation to the retrieval models of wind speed. The test results of the CYGNSS data showed that those novel retrieval models can perform better than the previous models in typhoon conditions, such as Rodriguez-Alvarez and Garrison (2015).

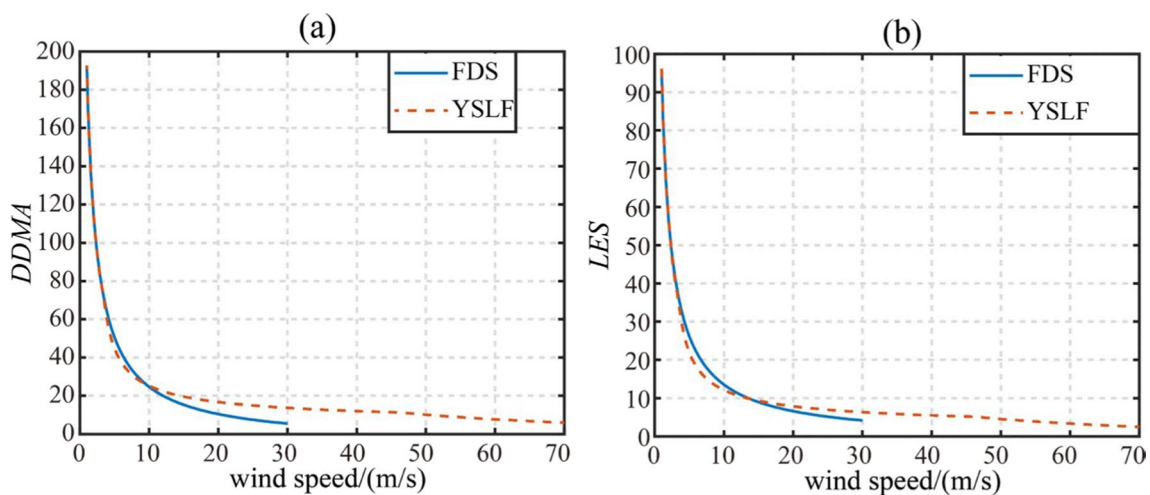


**Fig. 6** Relationships of DDMA (a) and LES (b) with wind speeds for FDS and YSLF conditions (Ruf & Balasubramaniam, 2018)

The other work was to perform the detection of typhoons and the estimation of typhoon structure, such as the maximum wind speed, typhoon eye position, and radio of maximum wind speed using spaceborne GNSS-R. Park et al. (2014b) discussed the feasibility of spaceborne GNSS-R detecting typhoons and locating cyclone eye by using an end-to-end performance simulator for GNSS Reflectometry, Radio Occultation, and Scatterometry onboard International Space Station (GEROS-ISS) mission. The proposed methodology is to reconstruct or map the scattering coefficients on the spatial domain from the DDM. This methodology was further demonstrated (Li et al., 2015), where a Spatial Integration Approach (SIA) was introduced to retrieve the scattering coefficients in the spatial domain from the DDM to detect oil slick and typhoon, as well to determine oil slick size and typhoon location. Figure 7 shows an example of detecting typhoons using this methodology, in which the reconstruction approach of the scattering coefficients is the constrained least squares (CLS) filter (Valencia et al., 2011). Compared to the DDM, the reconstructed scattering coefficients in the delay-Doppler domain can highlight the scattering coefficients of typhoon area due

to removing the modulations of the Woodward ambiguity function, antenna pattern, and propagation factors. Once the scattering coefficients are mapped from the delay-Doppler domain to the spatial domain, the typhoon area is clearly manifested in the spatial domain. However, this methodology is sensitive to the DDM SNR (higher SNR can obtain a better performance), and should solve an ambiguity problem (two spatial scattering cells in the spatial domain map into the same delay-Doppler bin in the DDM).

Another simpler approach to detecting typhoons is to use the specificity of the DDM in the case of typhoons. Wang et al. (2023) found that, as the specular point passed through a typhoon, there was an abnormal shift in DDM asymmetry. They identified two subsequent features—the slope and extremum difference—along the specular point’s trajectory, as indicators for typhoon detection. Figure 8 illustrates the subsequence features as the specular points traversed the typhoons “Champi”, “In-Fa”, “Linda”, and “Mindulle”. The defined two subsequence features are sensitive to the four typhoons. As the specular points passed through the typhoons, the subsequent slopes exhibited anomalous “heartbeat” fluctuations,

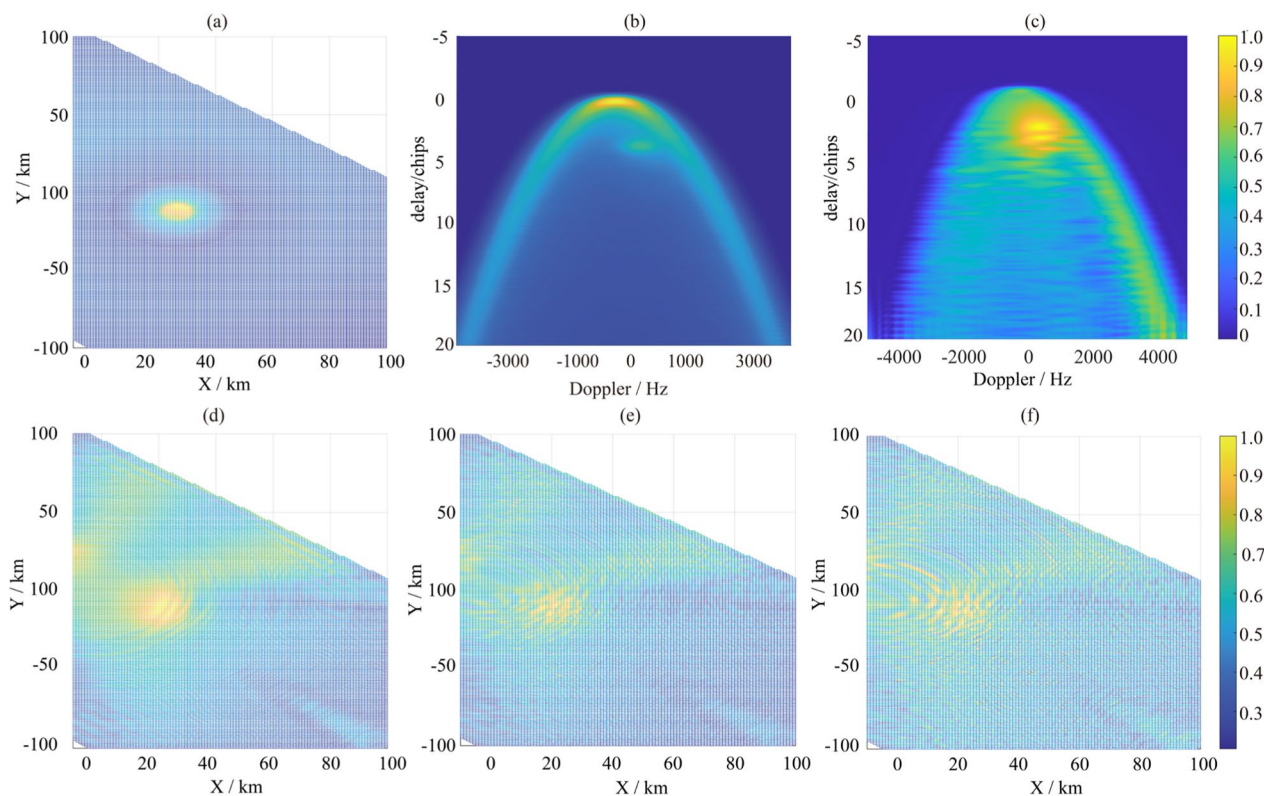


**Fig. 7** **a** Ground-truth scattering coefficients in the spatial domain; **b** Noise-free DDM in the case of typhoon; **c** Reconstructed noise-free scattering coefficients in the delay-Doppler domain using CLS filter; **d–f** Reconstructed and mapped scattering coefficients in the spatial domain from the noise-free DDM and the DDM with the SNR of 8 and 2 dB, respectively (Valencia et al., 2011)

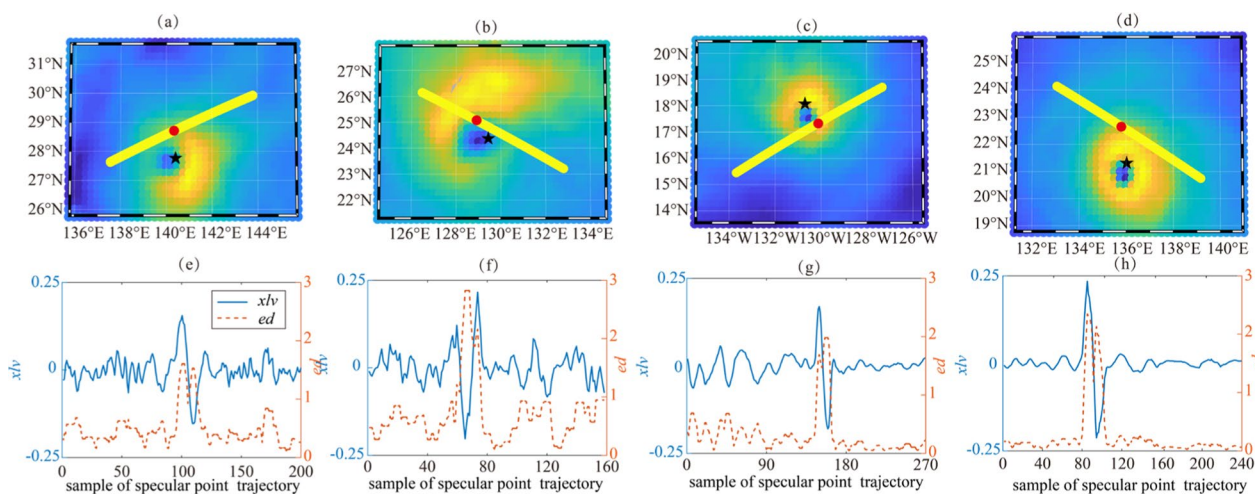


**Fig. 8** a–d MERRA-2 wind speed distributions and e–h subsequence features of tropical cyclones (a) and (e) “Champi” (b) and (f) “In-Fa” (c) and (g) “Linda” and (d) and (h) “Mindulle” (Wang et al., 2023). In (a)–(d), the black five-pointed star represents the tropical cyclone center, the yellow line corresponds to the trajectory of the CYGNSS specular point, and the red solid circles indicate the coarse estimations of the cyclone centers

while the extremum differences displayed bimodal anomalous fluctuations. The spatial and temporal distribution of wind speeds retrieved through spaceborne GNSS-R also aids in typhoon identification. Park et al. (2018) and Al-Khaldi et al. (2021a) developed a threshold-based (range or standard deviation of wind speeds within a time clump) detection mechanism to indicate convective activities. The algorithm to fix the typhoon center (Mayers & Ruf, 2019a, 2019b) used a parametric typhoon wind model to best-fit spaceborne GNSS-R wind speed data. It should be noted that these approaches have a strong dependence on the quality and temporal resolution of the retrieved wind speed from spaceborne GNSS-R.

At present, two types of approaches have been involved to estimate the parameters of typhoon structure. One method is to use the spatial and temporal distributions of wind speed retrieved via spaceborne GNSS-R. Similar to the procedure of fixing the typhoon center, the best-fitting of a parametric typhoon wind model to the spaceborne GNSS-R wind speed measurements also can be utilized to estimate the parameters of typhoon structure, such as the maximum wind speed, radius of maximum wind speed, and 50-kt wind radii (Morris & Ruf, 2017a, 2017b). The corresponding estimation errors for maximum wind speed, radius of maximum wind speed, 34-kt, 50-kt, and 64-kt wind radii respectively are  $-5.29$  m/s,  $-1.2$  km,  $-120.5$  km,  $-31.9$  km, and  $-2.8$  km. The estimation accuracies strongly depend on the accuracies of the parametric typhoon wind model and GNSS-R wind speed. The other method entails directly estimating typhoon parameters from spaceborne GNSS-R observations, like delay waveforms. An estimation algorithm for

typhoon maximum wind speed was proposed based on a matched filter between actual and theoretical waveforms (Said et al., 2017). This method was also expanded to incorporate the full DDM (FDDM) (Al-Khaldi et al., 2019a) and exhibited dependency on the typhoon models employed (Al-Khaldi et al., 2021a).

### Sea ice detection

Sea ice detection is an important task for climate studies, maritime navigation, and environmental monitoring (Yan & Huang, 2019c). However, traditional remote sensing methods, including Synthetic Aperture Radar (SAR) (Chen et al., 2023) and Passive Microwave Radiometry (PMR) (Petrou & Tian, 2019), have some limitations in terms of spatial resolution, temporal coverage, and sensitivity to different types of sea ice. GNSS-R represents a groundbreaking approach, leveraging reflected signals from navigation satellites like GPS, GLONASS, and Galileo, to infer information about the surface properties of the Earth. GNSS-R has several advantages over conventional methods, such as low cost, high availability, wide coverage, and high sensitivity to sea ice (Jin & Komjathy, 2010). In recent years, many studies have explored the potential of GNSS-R for sea ice detection and characterization (Alonso-Arroyo et al., 2017; Hu et al., 2017; Li et al., 2017; Schiavulli et al., 2017; Yan & Huang, 2016, 2018a, 2019a, 2019b; Zhu et al., 2017). Here, the main achievements and challenges are presented in this field, encompassing sea ice detection methods, type classification, concentration estimation, and thickness retrieval.

Sea ice detection methods are the first step to identifying the presence or absence of sea ice in a given area.



Several methods have been proposed based on different features extracted from the GNSS-R signals, such as delay-Doppler map (DDM) observables (Alonso-Arroyo et al., 2017; Hu et al., 2017; W. Li et al., 2017; Schiavulli et al., 2017; Yan & Huang, 2016, 2018a, 2019a, 2019b; Zhu et al., 2017), polarimetric ratios (PRs) (Fabra et al., 2011; Gao et al., 2017; Yun et al., 2014), waveform analysis (Hu et al., 2017; Li et al., 2017), and scattering coefficients ( $\sigma_0$ ) (Schiavulli et al., 2017; Yan & Huang, 2018b). These features capture the variations in the scattering behavior between sea ice and open water, which are mainly influenced by surface roughness, permittivity, and coherence. Some of the methods use supervised learning techniques, such as neural networks (NNs) (Yan et al., 2017), support vector machines (SVMs) (Yan & Huang, 2019a), and convolutional neural networks (CNNs) (Yan & Huang, 2018a), to classify the features into sea ice or open water classes. Other methods use unsupervised learning techniques, such as isometric mapping (ISOMAP) (Hu et al., 2024), to reduce the dimensionality of the features and cluster them into different groups. The performance of these methods depends on several factors, such as the quality of the GNSS-R data, the availability of ground truth or reference data, the choice of features and classifiers, and the environmental conditions.

Sea ice concentration estimation is the next step to quantify the fraction of sea ice in a given area. This is useful for assessing the extent and variability of sea ice in different regions and seasons. Several methods have been proposed based on different models that relate the GNSS-R features to the sea ice concentration (Yan & Huang, 2019b; Yan et al., 2017). Some of the models are empirical, such as linear regression or polynomial regression, which use historical data to establish a statistical relationship between the features and the concentration. Other models are physical, such as radiative transfer models or coherent scattering models, which use physical principles to describe how the GNSS signals interact with sea ice and open water. The performance of these methods depends on several factors, such as the accuracy of the models, the availability of calibration or validation data, the spatial resolution and coverage of the GNSS-R data, and the heterogeneity and dynamics of sea ice.

Sea ice type classification is another step to distinguish between various forms of sea ice, such as first-year or multi-year ice. This is useful for understanding the age and evolution of sea ice in different regions and seasons. The Classification and regression tree (CART) (Breiman, 2017) has been adopted to fulfill this task based on different features extracted from the GNSS-R DDM observables (Rodriguez-Alvarez et al., 2019a). These features capture the variations in the scattering behavior among

different forms of sea ice, which are mainly influenced by the salinity, density, porosity, and microstructure.

Sea ice thickness retrieval is the final step to estimate the vertical dimension of sea ice in a given area. This is useful for evaluating the volume and mass balance of sea ice in different regions and seasons. Several methods have been proposed based on different models that relate the GNSS-R features to the sea ice thickness including altimetric models (Li et al., 2017) or two-layer scattering models (Yan & Huang, 2020), which use physical principles to describe how the GNSS-R signals reflect from or penetrate into sea ice.

#### **Soil moisture retrieval**

Soil moisture (SM) is a crucial component in the water cycle, which directly affects the evaporation, infiltration, water loss, and hygroscopicity of plants. It is of great significance to agriculture, ecology, wildlife, and public health (Shi et al., 2012). Accurate measurement of soil moisture can study the energy balance between the land and the atmosphere, helps to predict and deal with disasters, such as floods and landslides, contributes to the development of fine agriculture, and is therefore related to the national economy and people's livelihood. However, it is usually impractical to obtain soil moisture on a larger scale through field measurements. Microwave remote sensing has the characteristics of all-weather, all-weather, and strong penetration ability, and is one of the most effective means to obtain soil moisture on large-scale and long-term time series. Existing microwave remote sensing systems, such as scatterometer and radiometer, can effectively penetrate the atmosphere and perform large-scale measurements under various weather conditions (Entekhabi et al., 2010; Zhu et al., 2022). However, due to the high cost of equipment, low spatio-temporal resolution, data sharing, and other factors, there are still some problems in SM retrieval and scientific research.

Compared with other measurement methods, GNSS-R technology is distinguished by its low cost and low power consumption, and enjoys many free and uninterrupted GNSS signal sources. Its receiver itself can use direct signals to achieve positioning and timing, and the L-band where the signal is located has the advantages of strong penetration in the atmosphere, low attenuation, etc., making it highly sensitive to soil moisture information, so that the GNSS-R has been widely used in land surface soil moisture estimation (Njoku & Entekhabi, 1996). In addition, the GNSS-R can provide strong spatial-temporal resolution and can receive multi-angle and multi-polarized reflected signals, which provides a variety of possibilities for the study of signal processing and calculation methods. At present, there are more than 130



navigation satellites around the world that can provide continuous and stable high-quality GNSS-R measurements with providing unprecedented opportunities for intensive soil moisture measurement.

The different relative dielectric constant of the surface observation object will cause the reflected signal to show different waveforms, which in turn affects the amplitude, phase, frequency, and other information of the reflected signal. The water content of the soil is positively correlated with the soil dielectric constant, that is, the water content of the soil is high, and its dielectric constant value is also higher (Njoku & Entekhabi, 1996). The variation in the dielectric constant results in an alteration of the reflectance of the received surface reflected signal. In addition, changes in vegetation cover and roughness on the surface will affect or complicate the forward process of soil moisture (Wan et al., 2015; Wu et al., 2021a). Therefore, the simplest foundation experiments are often carried out on relatively flat and open bare ground.

The total reflected power ( $P_r^s$ ) received by the GNSS-R receiver is the composite of different proportions of coherent reflection ( $P_{RL}^{coh}$ ) and incoherent scattering ( $P_{RL}^{inc}$ ), as shown in Eq. 23. This value depends on the dielectric constant of the signal reaching the scattered surface, the geometric characteristics, and the direction of incident and outgoing electromagnetic radiation (Yueh et al., 2020):

$$P_r^s = P_{RL}^{coh} + P_{RL}^{inc} \quad (23)$$

Among them, the calculation of the coherent component of the received signal for the dual-base radar can be written as:

$$P_{RL}^{coh} = \left( \frac{\lambda}{4\pi} \right)^2 \frac{P_t G_t G_r}{(R_r + R_t)^2} \Gamma_{RL}(\theta) \quad (24)$$

where  $\lambda$  denotes the wavelength,  $P_t$  represents the peak power of the transmitted GNSS signal,  $G_t$  and  $G_r$  indicate the gain of the transmitting and the receiving antenna respectively,  $R_r$  and  $R_t$  are the distances from the specular reflection point to the GNSS-R receiver and the GNSS transmitter, and  $\Gamma_{RL}(\theta)$  is the reflectance of the specular reflection point.

Equation (24) can be rewritten in the logarithmic format as:

$$\begin{aligned} 10 \log P_{rl}^{coh} &= 10 \log P_r^t + 10 \log G^t + 10 \log G^r \\ &+ 20 \log \lambda + 10 \log \Gamma_{RL} \\ &- 20 \log (R_{ts} + R_{tr}) - 20 \log (4\pi) \end{aligned} \quad (25)$$

Solving formula (25) can obtain the surface reflectance SR:

$$\begin{aligned} SR &= 10 \log \Gamma_{RL} = 10 \log P_{rl}^{coh} - 10 \log P_r^t \\ &- 10 \log G^t - 10 \log G^r - 20 \log \lambda \\ &+ 20 \log (R_{ts} + R_{tr}) + 20 \log 4\pi \end{aligned} \quad (26)$$

While the total reflected power comprises both coherent and incoherent components, it is unrealistic to completely separate the two in practice. Therefore, it is difficult to calculate the median value of the solution in Eq. (26) separately. Therefore, alternative parameters and scalars are typically employed. For example, the SNR or peak of each DDM is used instead of reflected power (Chew & Small, 2020; Yan et al., 2020a, 2020b). The peak of SNR or each DDM is not exactly equal. Therefore, the reflectance estimated according to Eq. (26) is called the equivalent reflectance. In addition, Eq. (26) shows that some potential and unknown factors affect the reflectance estimate, which in turn reduces its accuracy (Eroglu et al., 2019).

Equation (24) is usually used under relatively flat surface reflection conditions dominated by coherent reflection. In some areas with large topographic changes and roughness, or dense vegetation, the incoherent components contained in the reflected signal become stronger than the coherent components (Chew & Small, 2018; Clarizia et al., 2019; Ruf et al., 2018; Senyurek et al., 2020; Zavorotny et al., 2014). The incoherent or diffuse scattering components of the reflected signal are articulated by the subsequent equation (Zavorotny & Voronovich, 2000):

The calculation of the incoherent components can be written as follows:

$$P_{RL}^{inc} = \frac{\lambda^2 P_t G_t G_r R_{PL}}{(4\pi)^3 (R_r R_t)^2} \sigma_{RL} \quad (27)$$

$\sigma_{RL}$  is a bistatic radar cross-section in units of  $m^2$ , which is the Fresnel reflection coefficient. Among them:

$$\sigma_{RL} = A_s \sigma_{RL}^0 \quad (28)$$

where  $\sigma_{RL}^0$  is the NBRCS, which denotes the reflected surface area (often referred to as the shining area).

At this time, assuming that the surface reflection screen is relatively flat and smooth, the signal received by the GNSS-R receiver can primarily be considered as a coherent component, that is,  $P_{RL}^{coh} = P_{RL}^{inc}$ . Then the reflectance can be expressed as:

$$\Gamma_{RL}(\theta) = \frac{\sigma_{RL} (R_r + R_t)^2}{4\pi R_r^2 R_t^2} \quad (29)$$

In addition, based on the Kirchhoff Approximation (KA) model, both coherent and incoherent components in proximity to the specular direction are expressed as a

function of the Fresnel reflectance and the square of the Fresnel reflection coefficient ( $R_{RL}^2$ ) (Tsang et al., 1985).

The Fresnel coefficient can be solved by the specular reflectance of the reflection point:

$$\Gamma_{RL}(\theta) = R_{RL}(\theta)^2 \gamma^2 \exp(-h \cos^2(\theta)) \quad (30)$$

where the parameter  $h$  can be obtained directly from the SMAP data,  $\gamma$  is the opacity coefficient of vegetation,  $\gamma = \exp(-\tau \cos(\theta))$ , and the optical thickness of vegetation is calculated by the water content of vegetation (VWC) and the empirical coefficient of the land cover type. VWC can be obtained from the empirical value of the normalized vegetation index (NDVI) through SMAP data, which is directly provided by SMAP data.

The Fresnel reflection coefficient correlates with the dielectric constant ( $\epsilon_r$ ). After obtaining the Fresnel coefficient, the relationship between the reflectance and the Fresnel coefficient can be written as:

$$R_{RL}(\theta) = \frac{1}{2}(R_{VV}(\theta) - R_{HH}(\theta)) \quad (31)$$

Further, the dielectric constant is related to the soil water content (Tabbagh et al., 2013):

$$R_{HH}(\theta) = \frac{\cos\theta - \sqrt{\epsilon_r - \sin^2\theta}}{\cos\theta + \sqrt{\epsilon_r - \sin^2\theta}} \quad (32)$$

$$R_{VV}(\theta) = \frac{\epsilon_r \cos\theta - \sqrt{\epsilon_r - \sin^2\theta}}{\epsilon_r \cos\theta + \sqrt{\epsilon_r - \sin^2\theta}} \quad (33)$$

where  $R_{VV}(\theta)$  is the vertical polarization component and  $R_{HH}(\theta)$  is the horizontal polarization component, and both are functions of the angle of incidence  $\theta$  and the soil dielectric constant  $\epsilon$ . The Fresnel reflection coefficients for different polarizations function are based on the angle of incidence and the dielectric constant.

Therefore, the ideal GNSS-R-based soil moisture forward projection method relies on solving the dual-base radar equation when obtaining surface reflectance. After the acquired GNSS-R surface reflectance was corrected for the effects of vegetation cover and surface roughness to obtain the Fresnel reflectance coefficient. Further, the dielectric constant can be calculated by the Fresnel reflectance equation model, and the soil water content can be further solved. The method to estimate soil moisture by the dual-base radar equation mainly adopts the model method of reflectance, dielectric constant, and soil moisture, which is a typical method of positive soil moisture (Yin et al., 2023). Starting from this idea, the soil moisture forward observation model based on GNSS-R technology is roughly divided into the following three strategies:

The first method is to use the multipath reflection effect of GNSS signals, also known as GNSS-Interferometric Reflectometry (GNSS-IR) technology. Representative results mainly come from a group from the University of Colorado, USA. This method uses a ground-based RHCP antenna pointing to the zenith to simultaneously receive direct signals from GPS and reflected signals from the surface with causing multipath effects. The delay in the phase of the reflected signal relative to the direct signal causes the amplitude of the total received signal to change regularly with the sine of the satellite elevation angle  $\theta$  ( $\sin(\theta)$ ), and the soil moisture information will be reflected in the signal-to-noise ratio of the received signal (Geremia-Nievinski & Larson, 2013; Larson et al., 2010; Minsi et al., 2015; Wu et al., 2018; Yueji et al., 2020).

The second method is the "Interference Pattern Technique" (IPT), which was mainly developed by UPC University, Spain. This method usually uses a horizontally oriented Vertical Polarization (VP) antenna. The interference between the received direct and reflected signals will cause fluctuations in the total received power, and the point with the smallest amplitude fluctuation (notch) corresponds to the position of the Brewster angle, and the surface parameters are obtained by establishing a model (Rodriguez-Alvarez et al., 2009). Based on this IPT polarization interference theory, the UPC designed a new L-band reflectometer instrument (SMIGOL reflectometer), which can use GNSS interference mode to obtain parameters, such as terrain, soil moisture, and vegetation height (Rodriguez-Alvarez et al., 2011). In theory, IPT technology can be applied to both Vertical Polarization (VP) components and Horizontal Polarization (HP) components. As a result, Alonso-Arroyo et al. (2014) added an HP polarized antenna, proposed a measurement technique that involves tracing the phase difference between VP and HP interferogram, and updated the calculation model to enhance the precision of Brewster angle determination and further augment the SM measurement accuracy. Compared with the minimum notch detection algorithm, the change in calculation results is smoother, and the effectiveness of this method is verified. However, since IPT technology relies on the coherent scattering of the reflected signal, the reflected surface to be tested must meet the Rayleigh requirements of the smooth surface.

The third dual-base radar method (bi-static radar) is also the most commonly used. This method is commonly used in aircraft, satellites, and other platforms to realize mobile remote sensing of the surface. Since reflectance is a function of soil dielectric constant, elevation angle, and surface roughness, the dielectric constant can be calculated by correctly selecting a specific surface scattering model (Ulaby et al., 1986). Since then, the calculation

of soil moisture based on the dielectric constant of the microwaves (notably the L-band) has undergone extensive study, leading to the establishment of several recognized theoretical and empirical models (Dobson et al., 1985; Hallikainen et al., 1985; Mironov et al., 2009; Wang & Schmugge, 1980). However, most of the input variables to such models need to provide soil texture information, such as the percentage content of clay and sand. After obtaining the dielectric constant of the target observation point, combined with the soil texture information, the soil water content can be calculated.

In recent years, due to the demand for large-scale space and continuous observation, the method of using satellite constellations equipped with GNSS-R receivers to receive data and then retrieve soil moisture estimates by referring to soil moisture modeling has been widely recognized. Initially, space-borne GNSS-R missions were designed to monitor and observe the ocean, but the scattered signals received from land attracted more interests in land surface applications, like soil moisture estimation (Ruf et al., 2018), particularly from the CYGNSS mission.

The CYGNSS constellation mission with eight microsatellites was originally designed to monitor tropical cyclones and covered all regions from 38°N to 38°S latitude (Jin et al., 2017b; Li et al., 2014a). Each satellite of this mission can receive up to four signals at the same time, working as a multi-receiving bistatic radar. In this way, the data of eight satellites can be obtained at a single point in time to observe 32 different points on the earth's surface, and then obtain metadata such as DDM and BRCS. From this point, the CYGNSS constellation mission is designed to have a high temporal resolution (an average of 7.2 h in the ocean and 1–2 days on land) (Ruf et al., 2016). For specular reflection (Fresnel zone) and diffuse reflection (shining zone), the spatial resolution of the constellation theoretically ranges from 0.5 km to 25 km, respectively (Eroglu et al., 2019). Since 2019, the incoherent time of CYGNSS has been adjusted from 1 to 0.5 s, with the commonly utilized minimal spatial resolution by  $3.5 \times 0.5$  km (Chew & Small, 2020).

In retrieving soil moisture from CYGNSS data, most of the soil moisture released by the SMAP constellation mission is used as a reference and modeling basis. In terms of modeling methods, Chew and Small (2018) discovered and explained the correlation between CYGNSS reflectance and SMAP soil moisture changes through linear regression methods, with an unbiased Root Mean Square Error (ubRMSE) of  $0.045 \text{ cm}^3/\text{cm}^3$ . In 2019, Zribi et al. (2019) used ASCAT (C-band microwave scatterometer) to measure soil moisture on-site and evaluated the soil moisture retrieval algorithm proposed by it,

confirming the effectiveness of the retrieval algorithm. Chew and Small (2018) proposed a daily soil moisture product (UCAR CU) based on CYGNSS data with a spatial resolution of 36 km. It was verified by SMAP soil moisture, and the ubRMSE obtained was  $0.049 \text{ cm}^3/\text{cm}^3$  with a correlation coefficient of 0.4. Al-Khalidi et al. (2019b) utilized the maximal and minimal SMAP soil moisture references to constrain the limits of CYGNSS SM retrieval results and achieved an overall RMS error (RMSE) of  $0.04 \text{ cm}^3/\text{cm}^3$ . Kim and Lakshmi (2018) proposed to use the relative Signal-to-Noise Ratio (rSNR) from CYGNSS to retrieve soil moisture and derived the daily soil moisture estimator by amalgamating the rSNR of CYGNSS with the SMAP soil moisture.

Machine Learning (ML) and Deep Learning (DL) techniques are effective to study and model the linear or nonlinear relationships between input and output characteristics. For example, widely recognized supervised regression ML (such as Support Vector Machine (SVM), Decision Tree (DT), and Random Forest (RF)), along with neural networks have been used to enhance the accuracy of GNSS-R soil moisture retrieval (Yang et al., 2016), and Extreme Gradient Boosting (XGBoost) method were used to perform correlation analysis of the relationship between some input variables and soil moisture in the single-base radar method (Jia et al., 2019). Eroglu et al. (2019) proposed a soil moisture retrieval method based on Artificial Neural Networks (ANN). The input characteristics of ANN include CYGNSS reflectance and several other auxiliary data. The number of auxiliary data is large, and the retrieval effect is better. Yang et al. (2020) used a Back-Propagation Artificial Neural Network (BP-ANN) to construct a model to retrieve monthly soil moisture estimates at the target location, and at the same time evaluated the soil moisture retrieval performance of the CYGNSS and TDS satellite constellations. Furthermore, Santi et al. (2020a) used a multi-layer perceptron artificial neural network (MLP-ANN) algorithm to determine soil moisture and vegetation optical thickness (VOD). The estimated values of VOD and soil moisture (SM) obtained using the ANN algorithm were well consistent with the reference values provided by SMAP (RVOD=0.924; RSM=0.85), proving the potential of the algorithm in determining VOD and soil moisture parameters. Senyurk et al. (2020) used a variety of ML methods, such as ANN, SVM, and RF, to conduct comparative experiments. Comparing with the experimental results, the use of the RF algorithm to estimate SM has the best results, with an average ubRMSE of  $0.047 \text{ cm}^3/\text{cm}^3$ . Other methods are greatly affected by the quality of data. Yan et al., (2020a, 2020b) proposed the BRT (bagged regression

trees) method to retrieve SM, using CYGNSS data products, geographic location data, and related climate type information as input parameters, and the RMSE of the retrieval result was  $0.05 \text{ cm}^3/\text{cm}^3$ .

In terms of large-scale spatial study on a global scale, Jia et al. (2021) combined ML methods with pre-classification strategies to retrieve soil moisture and construct estimation sub-models based on different types of global surfaces. The results showed that under the pre-classification strategy, the accuracy of different ML retrieval algorithms has been significantly improved, and the pre-classification strategy has a positive effect on soil moisture retrieval. After that, Jia et al. (2022) used surface classification as an input parameter and used the strategy of digitizing surface parameters combined with the XGBoost algorithm to estimate global soil moisture. The model requires fewer input variables and better prediction accuracy. The average ubRMSE for Retrieve global soil moisture is  $0.041 \text{ cm}^3/\text{cm}^3$ . Similarly, Lei et al. (2022) used auxiliary data sets such as reflectance provided by CYGNSS data, and the soil moisture from SMAP as a reference value, and the RF method was used to achieve a global soil moisture estimate at a spatial resolution of 9 km. The retrieval result showed that ubRMSE reached  $0.0543 \text{ cm}^3/\text{cm}^3$ . The results indicated that the ML method based on the classification regression tree is more suitable for the retrieval of soil moisture from CYGNSS. In addition, some scholars have tried to elucidate the impact of interfering factors through the application of semi-empirical methods or the development of new model algorithms (Calabia et al., 2020; Tang & Yan, 2022). Meanwhile, ML and DL methods were employed to investigate and delineate the potential nonlinear relationship among interfering factors (such as vegetation and surface roughness), GNSS-R observations, and soil moisture, and more significant results were achieved.

### Flood mapping

Flooding is usually a surge of water caused by heavy rainfall or snowmelt over a short period of time, etc. Each year, human casualties and property damage due to flooding rank among the highest of all types of disasters (Mishra et al., 2022). When a flood occurs, high temporal and spatial resolution flood monitoring can not only provide a reference for the government's rescue decision-making, but also help in post-disaster reconstruction planning. At the same time, flood monitoring enhances our understanding of the spatial and temporal dynamics of floods, offering crucial support for future flood forecasting and early warning systems (Hirabayashi et al., 2013; Jonkman, 2005; Klemas, 2015).

The traditional flood monitoring approaches such as hydrological station monitoring, although highly accurate, are small in scope, time-consuming, and labor-intensive, falling short of the demands for large-scale monitoring. The advent and advances of satellite remote sensing technology have revolutionized inland water monitoring, switching from the conventional single-point scale to a wider spatial scale and providing technical support for long-time sequence and large-scale inland water monitoring (Bates, 2004). However, optical remote sensing missions (such as Sentinel-2, Moderate Resolution Imaging Spectroradiometer (MODIS), Landsat, GF-2, GF-6, and ZY-3) are susceptible to cloud cover and vegetation obscuration (Asner, 2001). Comparatively, microwave remote sensing is favored for soil moisture monitoring and inland water monitoring, benefits from its resilience to clouds and vegetation and its sensitivity to surface dielectric constants. Microwave remote sensing is categorized into active and passive types based on whether or not the signal is actively emitted. Common active microwave remote sensing satellites include Sentinel-1 SAR, ALOS-2, TerraSAR-X, GF-3, and others. Although they can provide high spatial resolution (10 m–10 km), the time resolution of active microwaves is low (7d–15d). Common passive microwave remote sensing satellites include SMAP, SMOS, AMSR-E, FY-3, and so on. Although they can provide high temporal resolution (1–3d), the spatial resolution of passive microwaves is low (> 25 km).

Spaceborne GNSS-R is an emerging remote sensing technology that has emerged in recent years. Using a constellation of near-Earth micro-satellites to receive and process the surface-reflected L-band signals emitted by the GNSS, spaceborne GNSS-R is now widely employed for the inversion of various oceanic and land surface parameters (Rodriguez-Alvarez et al., 2010). As compared to active microwave remote sensing, GNSS-R leverages pre-existing GNSS L-band signals, resulting in reduced costs and lower power consumption (Hein, 2020). Compared to passive microwave remote sensing, GNSS-R measurements of forward-scattered signals are less susceptible to the influence of surface roughness. In conjunction with the many GNSS signals that already exist and are available in large quantities free of charge, spaceborne GNSS-R technology has received increasing attention. Numerous spaceborne GNSS-R missions have been developed, such as UK-DMC and TDS-1 in the United Kingdom, the CYGNSS in the United States, and BF-1 and FY-3 in China. Among them, CYGNSS is currently the only mission that operates in orbit and opens the download of observations to the public free of charge. Here, some major achievements are presented in the field of CYGNSS flood detection.



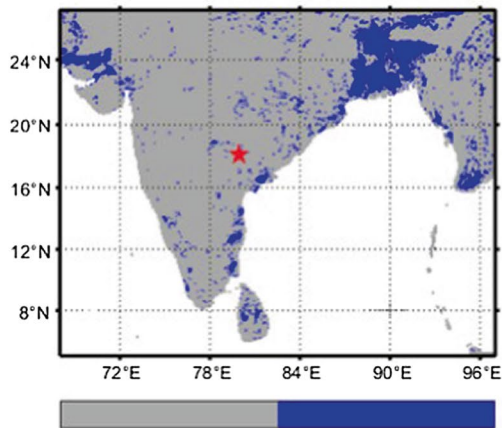
In 2018, Chew et al. (2018) conducted flood detection in parts of the United States and the Caribbean during the 2017 Atlantic typhoon season using CYGNSS data, and obtained surface inundation maps before and after flooding, respectively, using the reflectivity threshold method. A comparison of the inversion results with SMAP surface bright temperature data and Landsat optical imagery demonstrates that spaceborne GNSS-R can provide higher-resolution surface inundation information (Chew et al., 2018). This marked the inaugural demonstration of the feasibility of CYGNSS data for flood detection. Wan et al. (2019) used the CYGNSS reflectivity threshold method to delineate the extent of flooding caused by heavy rainfall during the 2017 typhoon season in China, revealing a significant correlation between the CYGNSS surface reflectivity and Global Precipitation Measurement (GPM) data. The flood extent mapped from CYGNSS data closely aligns with the surface brightness temperature data from SMAP and SMOS. Rodriguez-Alvarez et al. (2019b) utilized a ML method based on the RF algorithm with multiple decision tree random structure (MDTR), using CYGNSS peak SNR, leading edge slope, trailing edge slope as well as topographic data and vegetation information as inputs. It was shown that seasonal floods within the Pacaya-Samiria Nature Reserve, situated in the Peruvian Amazon's tropical wetlands, were categorizable into three types, namely, Open Water (OW), Flooded Vegetation (FV) and Non-Flooded vegetation (NF). The findings indicated classification accuracies for OW, FV, and NF at 65.4%, 60.26%, and 94.75%, respectively (Rodriguez-Alvarez et al., 2019b). Unnithan et al. (2020) combined CYGNSS data with terrain data and generated flood inundation maps using parameters such as the height of the nearest drainage system (HAND) and the slope of the nearest drainage system (SND). Meanwhile, Sentinel-1A's Synthetic Aperture Radar (SAR) data were employed to simulate the floods occurring in Kerala in August 2018 and northern India in August 2017. The findings revealed that CYGNSS's flood detection accuracy ranged from 60 to 80% (Unnithan et al., 2020). Rajabi et al. (2020) investigated the feasibility of monitoring the spatial and temporal evolution of floods using CYGNSS data during the 2020 heavy rains in Sistan and Baluchistan, Pakistan. The study concluded that CYGNSS SNR was effective for detecting and mapping flood distribution, with retrieval results aligning well with flood data from MODIS optical imagery (Rajabi et al., 2020). Liu et al. (2021) investigated the spatial and temporal variations of seasonal floods in South Asia using the coherent signal detection approach, utilizing CYGNSS raw count DDM proposed by Al-Khaldi et al. (2021b). The results showed that, during the dry season, the monitoring extents of the two methodologies were

largely comparable to the flood detection results from SMAP. However, in the rainy season, the detection scope for surface reflectivity exceeded that of power ratio. The spatial distribution of CYGNSS coherent signals in South Asia in May and August 2020, as well as the spatial distribution of floods in South Asia obtained using CYGNSS surface reflectivity and SMAP satellites are given in Fig. 9 (Liu et al., 2021).

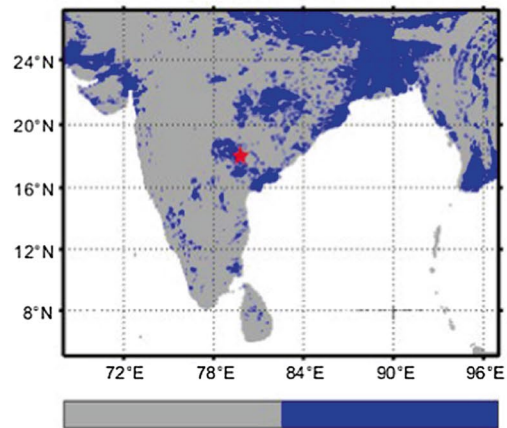
Zhang et al. (2021) inverted the surface inundation during extreme precipitation in Henan, China in 2021 using the surface reflectivity threshold (SR) method. The SR threshold was established through a comparison of SR values across various land covers and land uses in Henan, China. The comparison revealed that the retrieval results closely mirrored the inundation extent from SMAP, with the former boasting superior spatial and temporal resolution. Figure 10 shows the differences in the CYGNSS basic observation DDM for an area before and after the occurrence of the 7.20 rainstorm in Henan, China (Zhang et al., 2021). The specific statistics are given in Table 3 (Zhang et al., 2021). Figure 11 gives the changes in surface reflectivity, soil moisture, and daily rainfall before and after the flooding in a region of Henan, China (Zhang et al., 2021).

Yang et al. (2021b) undertook a parallel study with employing the surface reflectivity thresholding method to map the flood distribution across Henan Province, China in July 2021. Unlike previous studies, Yang et al. (2021b) linearly interpolated the daily CYGNSS SR, which in turn yielded daily flood monitoring results. MODIS and SMAP data were served as validation data, and results revealed a strong correlation among the three datasets. Zeiger et al. (2022) analyzed the surface reflectivity of CYGNSS in depth and assessed its potential for dynamic mapping of global floods. An optimal balance between high spatial and temporal resolution was identified with a spatial resolution of  $0.1^\circ$  and a sampling interval of every 7 days. In addition, the results showed that even along the Amazon and Congo rivers, where surface biomass (AGB) was as high as 300 Mg/ha, and CYGNSS data can still identify major floodplains and open waters. Zhang et al. (2023a) explored the potential of employing CYGNSS data for near-real-time flood monitoring. Daily, 3 km flood monitoring results were obtained by interpolating CYGNSS SR through a newly proposed spatial interpolation method based on previous observations (POBI) (Chew, 2021).

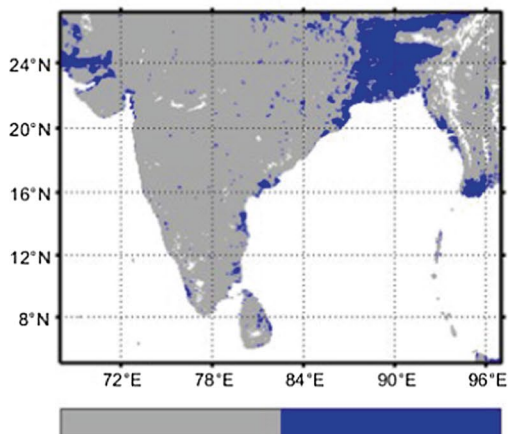
Wei et al. (2023) combined Sentinel-2 data to classify the surface into high soil moisture areas and low vegetation cover areas and proposed a dual-threshold method based on the classification results, which was successfully applied to the detection of flooding in Guangdong Province, China in the summer of 2022. Downs et al.



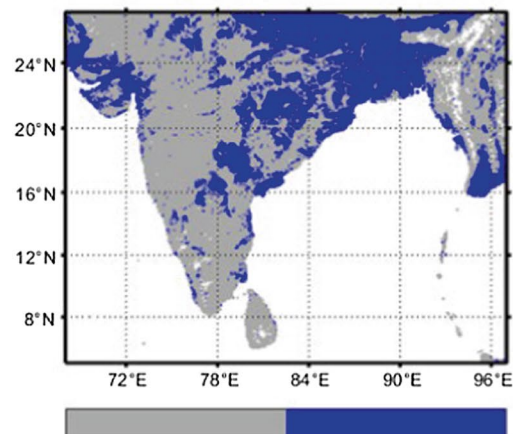
(a) Distribution of coherent regions in May (coherent blue, incoherent gray, the same below)



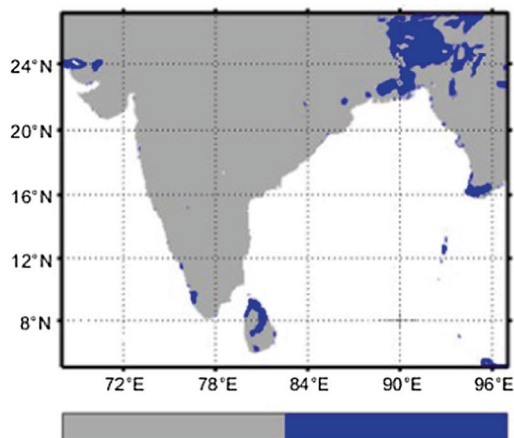
(b) Distribution of coherent regions in August



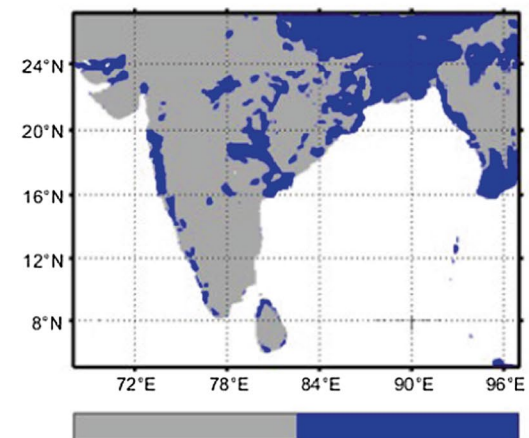
(c) May Flood Distribution Obtained by Reflectivity (Flood Blue, Same Below)



(d) August Flood Distribution Obtained by Reflectivity



(e) May Flood Distribution Detected by SMAP



(f) August Flood Distribution Detected by SMAP

**Fig. 9** Spatial Distribution of CYGNSS coherent signals and flood using CYGNSS Surface Reflectivity and SMAP in May and August 2020 (Liu et al., 2021)

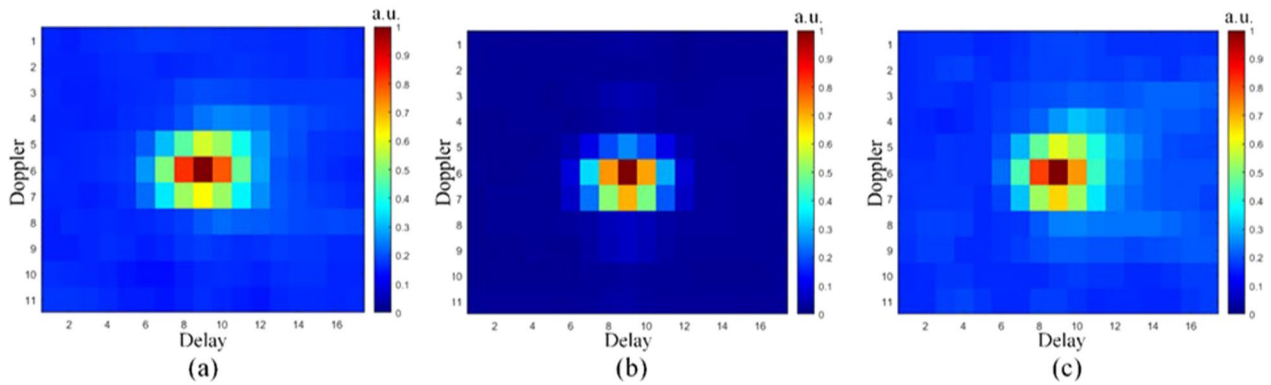


**Fig. 10** Delay-Doppler map (DDM) changes before and after floods in the same area. **a** 5 June (before the flood); **b** 23 July (flooding); and **c** 13 August (after the flood) (Zhang et al., 2021)

**Table 3** Changes in delay-Doppler map (DDM) parameters before and after floods in the same area. Effective isolated radiated power (EIRP), surface reflectivity (SR), and SNR (Zhang et al., 2021)

| Date      | Satellite number | SP position |           | Track number | EIRP (watt) | SNR (dB) | SR (dB) |
|-----------|------------------|-------------|-----------|--------------|-------------|----------|---------|
| June 5    | Cy02             | 114° 19' E  | 34° 42' N | 251          | 528.57      | 8.03     | -17.96  |
| July 23   | Cy03             | 114° 15' E  | 34° 48' N | 466          | 724.74      | 16.93    | -6.15   |
| August 13 | Cy02             | 114° 16' E  | 34° 42' N | 969          | 595.33      | 7.67     | -18.25  |

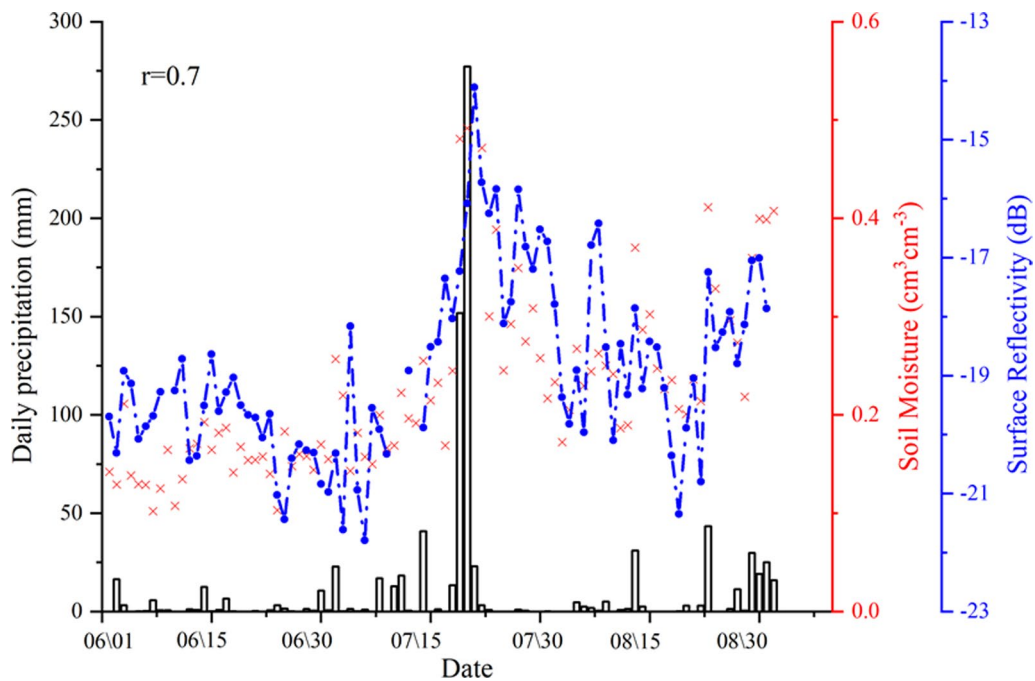


**Fig. 11** Changes in precipitation, soil moisture, and reflectivity near (34°N, 114°E) from June 1 to August 31, 2021. Black bars represent the precipitation, red scatter plots represent soil moisture, and blue dot plots represent surface reflectivity.  $r=0.7$  (Zhang et al., 2021)

(2023) conducted an in-depth study of the performance of spaceborne GNSS-R in detecting inland water bodies in the case of South Sudan, and quantitatively compared the water distributions obtained by CYGNSS with those obtained by MODIS, the Visible Infrared Imaging Radiometer (VIIRS), and the Sentinel-1 SAR in the C-band, respectively. The results showed that CYGNSS detected 35.4% more surface water when compared to Sentinel-1, whereas the VIIRS- and MODIS-based products underestimated these amounts by 4.8% and 83.7%, respectively. Yang et al. (2023a, 2023b) introduced a novel flood inundation retrieval index utilizing the CYGNSS data, the inter-annual threshold flood inundation index (ATFII), and flood inundation levels were quantified. The results were validated using VIIRS flood products and GPM precipitation data. Comparisons showed that the ATFII was capable of quickly mapping areas where flooding occurs and can reflect changes in inundation levels.

**Snow and cryosphere sensing**

GNSS-IR has been developed and used in estimating snow depths (Larson et al., 2009; Pinat et al., 2021; Yang et al., 2023a, 2023b; Zhang et al., 2023a, 2023b, 2023c) (Fig. 12), e.g., sensing snow depth variation using the GNSS SNR measurements (Larson & Nievinski, 2013) and phase-based multipath (Qian & Jin, 2016). Compared to other methods such as sonic rangers (footprint

around 1 m<sup>2</sup>), the GNSS-IR is well suited to remote regions since the estimate of daily snow depth can have a footprint between 1000–10,000 m<sup>2</sup> (Larson & Nievinski, 2013; Larson et al., 2020). Snow water equivalent (SWE) retrieval is possible by analyzing the phase difference between reflected and direct signals (Bai & Tan, 2020).

The GNSS reflected signals from each layer of snow allow us to estimate the snow and ice thickness. This measurement is possible by observing the delay of the reflected signal, with depth modeled based on the angle of incidence or the relative amplitude among the various polarizations (Fabra et al., 2011). Ice thickness, surface roughness, and permittivity measurement have been estimated (Cardellach et al., 2012; Komjathy et al., 2000). Rivas (2007), Rivas et al. (2009), and Wang et al. (2022) studied the temperature of the reflecting surface to distinct frozen areas from non-frozen areas. Furthermore, surface roughness and permittivity were retrieved through analyzing polarimetric reflectivity (Rivas et al., 2009).

**Vegetation remote sensing**

Vegetation water content and forest biomass content have been studied using GNSS multipath effects (Motte et al., 2016). The Leaf Area Index (LAI), and the Vegetation Height (VH) have been measured using GLORI

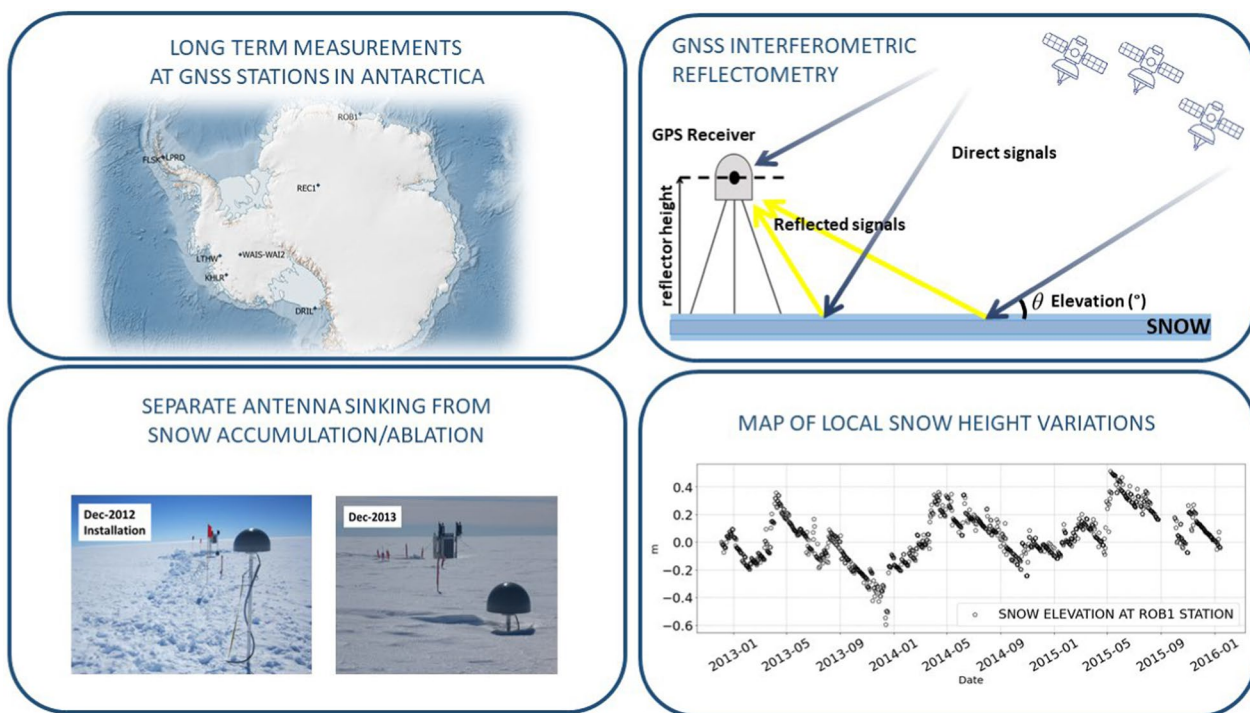


**Fig. 12** GNSS-IR for snow height measurement (Pinat et al., 2021)



airborne observations by (Zribi et al., 2018). For ground-based GNSS-R vegetation parameters estimation, the SNR method and IPT are the most widely used. The multipath information from the SNR was used to retrieve the vegetation water content and NMRI (Normalized Microwave Reflection Index) (Chew et al., 2016; Haase et al., 2008; Loria et al., 2019). The IPT employs an enhanced GPS receiver with improved vertical and horizontal polarization to acquire the surface properties (Rodriguez-Alvarez et al., 2010, 2012). The vegetation height information can be obtained by the notch position and number information of the interference waveform.

For airborne platform, Egido (2013) demonstrated a correlation between the bistatic reflectivity and the biomass for levels as high as 300 tons/ha. The LEiMON (Land Monitoring with Navigation Signals) experiment in the Florence agricultural area, Italy, showed a good correlation between the reflected signals and vegetation moisture content (Egido et al., 2012). ESA’s GRASS experiment carried out in Tuscany, Italy revealed that a level of AGB (Average Ground Biomass) was achieved, which was not possible with other remote sensing systems (Egido et al., 2014).

Camps et al. (2016) demonstrated the feasibility of monitoring vegetation through spaceborne GNSS-R. Carreno-Luengo et al. (2020) used the CYGNSS simulator to explore the relationship between GNSS-R observations and forest biomass, and some results were obtained

(Fig. 13). Santi et al. (2020b) studied and estimated forest biomass by using TDS-1 and CYGNSS data.

**Target detection**

In 2014, the University of Birmingham and Beihang University collaborated to investigate the potential of using Galileo navigation satellites as opportunistic transmitters for passive bistatic SAR systems, considering both signal processing and experimental protocols. Images captured through either the Galileo satellite’s E5a or E5b channel were obtained and analyzed. The channel combination scheme was proposed to merge E5a and E5b signals from the E5 band of the Galileo navigation satellite, which provided the possibility of high-resolution imaging in passive SAR technology. Utilizing the full E5 band for imaging was shown to potentially increase range resolution by a factor of five (Ma et al., 2015). Some experiments and results were shown in Figs. 14 and 15, respectively. Pieralice et al. (2017) conducted an experiment using a fishing boat as a small target over the sea. The experiment utilized the GLONASS satellite as the opportunity illuminator and recorded the boat’s position using a GPS receiver onboard. With the known speed of the boat’s movement, the real position of the target could be determined on the RD (Range-Doppler) map (Fig. 16). By accumulating non-coherently target echoes, distinct peaks were observed in the resulting map, enabling effective target detection. Furthermore, the target’s position

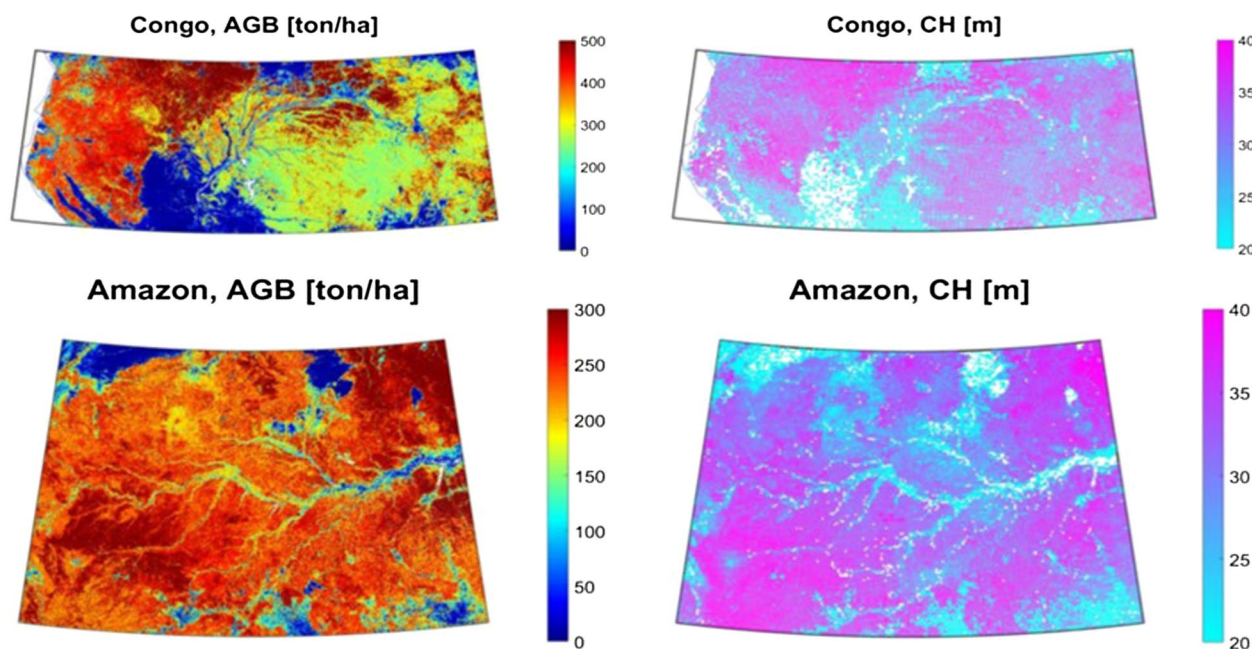


**Fig. 13** Above-Ground Biomass (AGB) and canopy height (CH) for Congo and Amazon (Carreno-Luengo et al., 2020)





**Fig. 14** Experimental hardware (Ma et al., 2015)

on the RD map was matched the position recorded by the GPS receiver (Pieralice et al., 2017).

Ma et al. (2017) conducted experiments to validate the feasibility of GNSS-based passive radar for maritime target detection (Fig. 17). A ferry sailing along a prescribed route was chosen as the target on the sea surface. Two Galileo satellites, GSA-SAT0201 and GSA-SAT0203, were selected as the illuminators of opportunity. Their transmitted E5a-Q signals were received by the receiving system. In the experiment, the total observation duration of the target by the receiving system was 145 s. The experiment validated the effectiveness of using target echo signals and performing azimuthal Fourier transform to achieve large-scale maritime target detection (Ma et al., 2017). Zhou et al. (2019) and Wu et al. (2021b) from Beihang University carried out a GNSS bistatic SAR imaging, while the receiving station was placed on the chairman's platform of a 3 m high football stadium, and the building in the university was used as the imaging area. Finally, azimuth phase compensation and geometric correction were carried out (Fig. 18). By observing the areas of strong scattering points, it can be seen that the edge of the swimming pool, gymnasium, gymnasium's spire, and teaching building (identified as 1–6 in the figure) aligned with those in the optical image, and the calculation efficiency was improved by nearly 10 times (Zhou et al., 2019).

In addition, He et al. (2020) from Hong Kong Polytechnic University conducted a study on the use of

GNSS-based passive Radar for moving target detection. They proposed a novel hybrid coherent and incoherent integration scheme termed the trapezoidal transform and Lv distribution. This method compensated for both the RCM and the DFM, while also offered integration gains, both coherent and noncoherent, to enhance the SNR (He et al., 2020). Santi et al. (2020c) proposed a detection strategy that reduced the sensitivity of prolonged integration methods to the chosen motion model. This approach offered computational complexity savings and made it attractive for real-time implementation.

Furthermore, Zhou et al. (2022) from Beihang University introduced a Moving Target Indication (MTI) algorithm based on High Frame Rate Image Sequences (HFRIS) into GNSS-based Passive Bistatic Radar (PBR). This algorithm avoids the need for iterative multidimensional parameter search, resulting in higher computational efficiency when compared to methods based on Range-Doppler Frequency-Time (RDFT) (Fig. 19). Li et al. (2021) from University of Electronic Science and Technology of China introduced a Maritime Moving Target (MMT) detection technique based on BDS Passive Multi-static Radar (PMR), which obtained the moving target through Space-Time Hybrid Integration (STHI) processing and the final integration result (Fig. 20).

In addition, Zhang et al. (2023b) from Wuhan University proposed a bistatic structure for Beidou synchronized Geostationary Earth Orbit (GEO) satellite

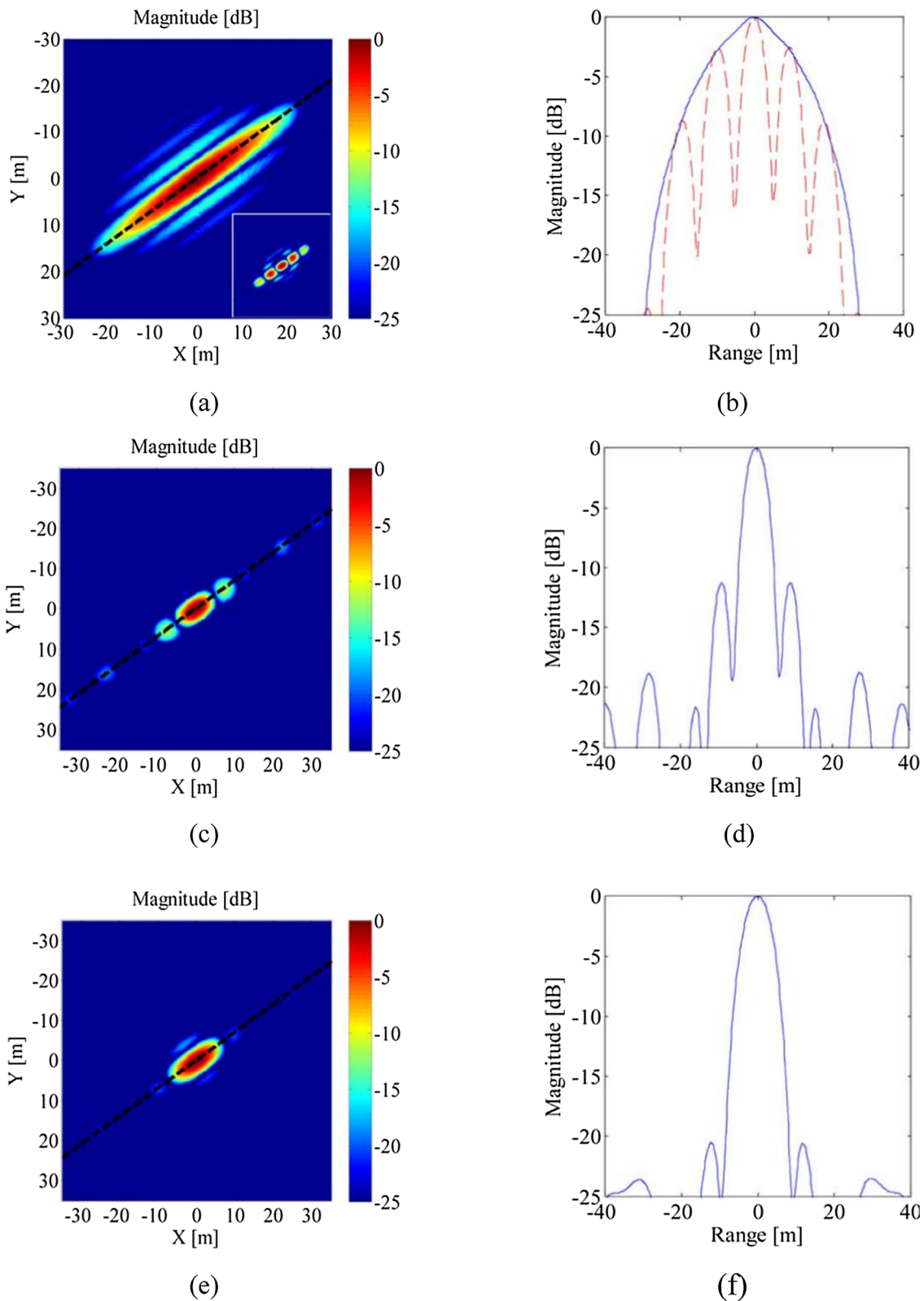


**Fig. 15** Experimental results. **a** PSF of the single E5b-Q band, with an inset featuring the coherently combined E5a-Q and E5b-Q band, maintaining uniform dimensions for the X- and Y-axes and utilizing a consistent color bar. **c** PSF of the combined E5-Q band employing the proposed method. **e** PSF resulting from the application of a Kaiser window to the range-compressed data. The range direction is delineated by the black dotted lines in all PSFs. **b, d, f** represent the range cross-sections of PSFs in **(a)**, **(c)**, and **(e)**, respectively (Ma et al., 2015)

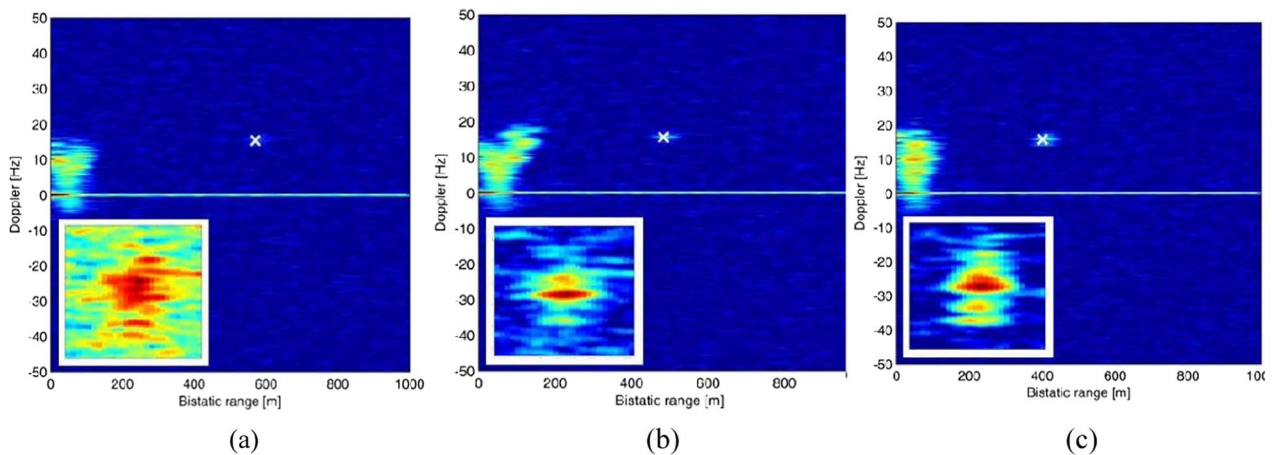


**Fig. 16** GNSS satellite-based target detection conducted at the University of Rome with the target detection results from a single frame (a), the target detection results from multiple frames without TMC (b), and the target detection results from multiple frames with TMC (c) (Pieralice et al., 2017)

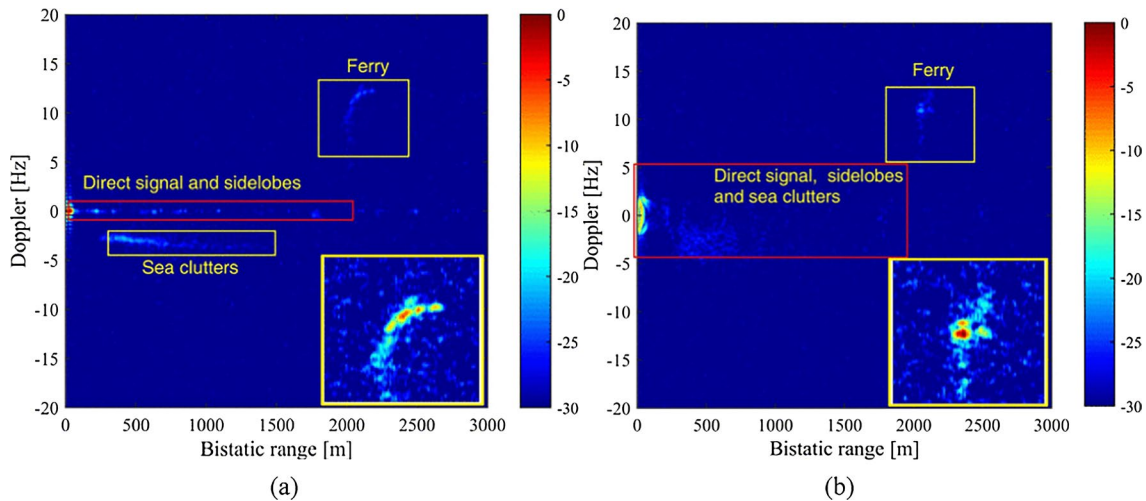


**Fig. 17** Experimental results from satellite 2–20 consecutive RD maps with integrated (a) and without (b) target motion compensation, with a total data acquisition time of 50 s (Ma et al., 2017)

opportunity signal reception, suitable for short-term coherent integration of echo signals and introduced corresponding signal processing methods. Therefore, GNSS-R technology provides promising opportunities for target detection in various domains. Whether in maritime, urban, or environmental applications, GNSS-R signals offer valuable information about target characteristics.

### Opportunities and prospects

#### Future developments

For ground-based GNSS-R observations, the evaluation of the BRCS across diverse vegetation types from very low altitude platforms (<20 m) to assess their effectiveness for commercial drones may be included

in the future research. New signals with a higher bandwidth, such as GPS L5 or Galileo E5a are currently explored with airborne studies. The feasibility of combining RHCP and LHCP antennas with coherent receivers is being explored using airborne observations to detect the polarimetry signature of the surface. The effectiveness of the utilization of two polarization antennas to directly estimate soil moisture, bypassing the need for surface roughness correction or vegetation attenuation, is currently being explored. The electronics miniaturization, help providing more data by integrating GNSS-R receivers, is a great achievement. The DDM generation in orbit with current approaches is an advance since it provides relaxed requirements with





(a)



(b)

**Fig. 18** Comparison of the optical and the radar image results. **a** Represents the optical image, while **b** denotes the radar image (Zhou et al., 2019)

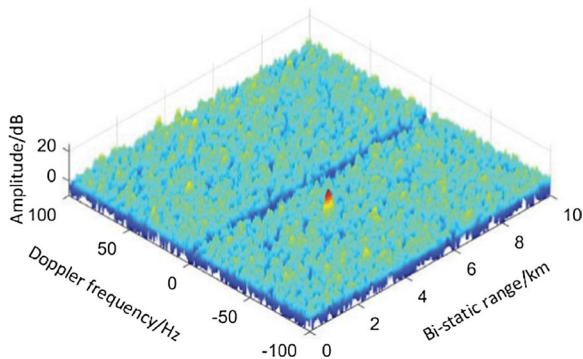


**Fig. 19** RD image of the target return generated by 1-s integration using the GRFT algorithm. The zero Doppler regions were isolated through frequency domain filtering to suppress the background clutters (Zhou et al., 2022)

a decreased data budget for the mission. For future missions, it may be imperative to integrate multi-channel correlators for various polarizations and cross-correlation channels to accurately generate the full Stokes parameters of the reflected wave. For better retrieval of geophysical parameters, all types of multi-GNSS constellations with higher bandwidth signals and polarimetric schemes must be integrated. Furthermore, developments in GNSS-R receivers, algorithms, and satellite missions will expand the scope and effectiveness of target detection using GNSS-R signals in the future.

**Emerging applications**

GNSS-R, beyond its traditional applications, starts to explore other areas of research or phenomena. Mesoscale ocean eddies, targets above the Earth’s surface, ionospheric plasma loss, river flow, ocean phytoplankton



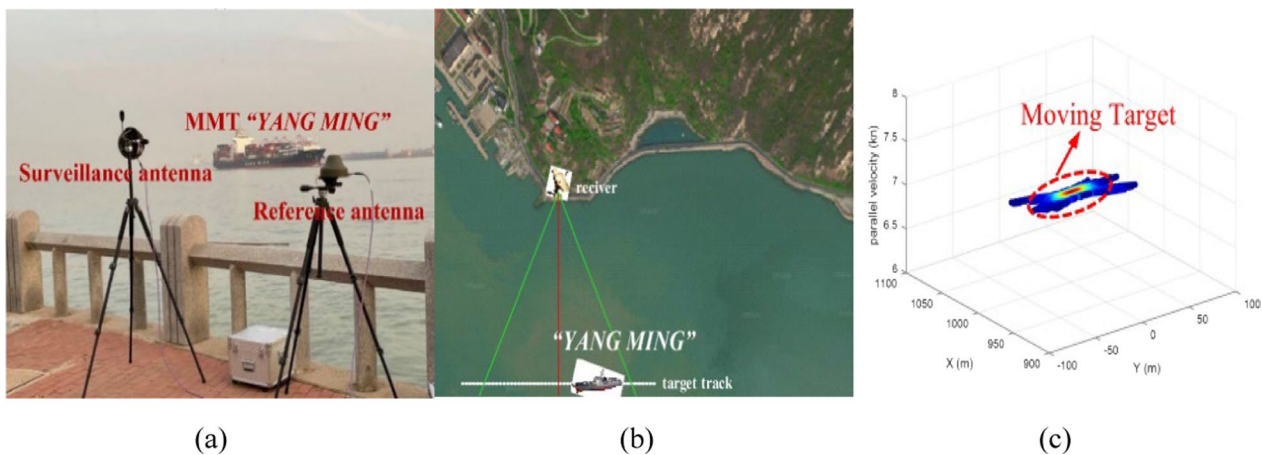


**Fig. 20** Detection experiment moving target (a), top view of the receiving geometry (b) and the final integration result at the X–Y–V domain (c) (Li et al., 2021)

blooms, ocean microplastics detection, and desert studies are some new areas being explored by GNSS-R (Rodriguez-Alvarez et al., 2023).

**Mesoscale ocean eddies**

Mesoscale ocean eddies can influence near-surface wind, cloud properties, and rainfall. GNSS-R (e.g. CYGNSS) offers a possibility to study ocean eddies. The utilization of CYGNSS data to detect mesoscale ocean eddies feasibility was the first time reported by Hoseini et al. (2020). The NBRCS responses were clearly observed at the center or edges of the eddies, and the analysis showed a strong inverse correlation between the sensible heat flux and the normalized bistatic radar cross section (Rodriguez-Alvarez et al., 2023). In addition, the so-called “Eddies Experiment” onboard the German High Altitude Long Range (HALO) Research Aircraft showed the capability of the GNSS-R technique for ocean eddie observations (Fig. 21).

**Above earth’s surface target detection**

Target detection above earth’s surface using GNSS-R was first studied by Simone et al. (2017) and then followed by Hu et al. (2019) during an investigation. They concluded in their work that the bright reflected signals that occur at a shorter delay than specular reflections are reflected from objects located above the Earth’s surface. Simulations of GNSS-R have demonstrated their capability to detect maritime ship targets (Fig. 22) (Lan et al., 2021) and aerial vehicles with experimental results (Suberviola et al., 2012). Furthermore, regarding the techniques, several methods have been proposed including backscattering configuration, sea clutter

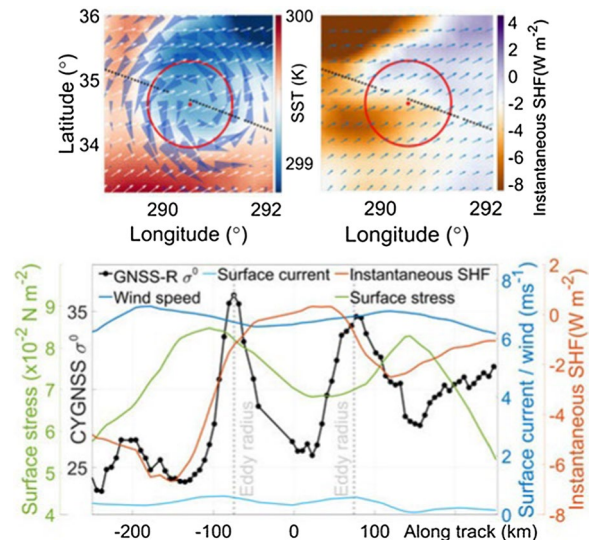


**Fig. 21** A CYGNSS track overpassed an eddy on 4 July 2017, 12:24. The top-left panel displays sea surface temperature, surface wind (indicated by white arrows), and current (represented by blue cones). The top-right panel visualizes instantaneous surface Sensible Heat Flux (SHF) and surface stress (illustrated with blue arrows). The bottom panel profiles CYGNSS  $\sigma_0$  along with the wind and current velocity, instantaneous SHF, and surface stress magnitudes (Hoseini et al., 2020)

compensation, sea target detection from GNSS-R DDM by using the spatial filter, and the constant false alarm rate (CFAR) method (Simone et al., 2017).

**Ionospheric plasma depletions**

The ionosphere impacts the GNSS-R signal, and its fluctuations in the electron content density can affect considerably the signal delay, intensity and phase, direction

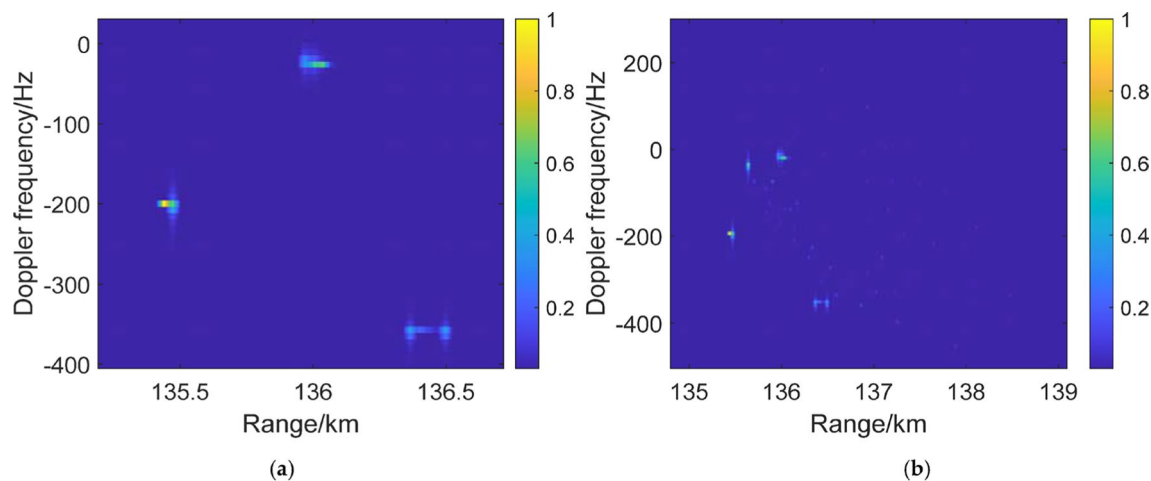


**Fig. 22** DDM detection results of 3 ship targets under the detection of satellite 3 without clutter and noise influence (a) and with clutter background (b) (Lan et al., 2021)

of arrival, polarization change, etc. Molina and Camps (2020) used CYGNSS data to study ionospheric plasma depletions. Electromagnetic waves experience signal delay, polarization change, direction of arrival, and fluctuations in signal intensity and phase were used to detect ionospheric bubbles in ocean regions. Furthermore, the measurement of the dimensions, duration, and the increased intensity scintillation (S4) of the ionospheric bubbles was demonstrated (Molina & Camps, 2020).

#### River flow

River flow velocity is fundamental in hydrologic studies, and its detection is valuable for the reason that it links variables such as hydrologic detection, flood control engineering design, hydrologic prediction, ecological environment assessment, and hydrodynamic research (Eric et al., 2021). The potential of the GNSS-R application in river flow measurement was studied using the Chinese BDS constellation (Zhang et al., 2022a, 2022b). A river flow velocity retrieval model, based on carrier phase observations, was developed to include both open-loop tracing and the carrier phase streamflow retrieval method.

#### Phytoplankton and green algae

Ocean surface roughness is decreased by the change in ocean surface tension with the areas covered by phytoplankton, and GNSS-R can be utilized to capture this change. The detection and monitoring of phytoplankton levels on the ocean surface using CYGNSS data were studied for the first time by (Rodriguez-Alvarez & Oudrhiri, 2021). The results illustrated the potential

of GNSS-R as an efficient tool for mapping phytoplankton inundation areas. The detection of the density of red tide was investigated by utilizing TDS-1 data (Ban et al., 2022a), where the used methods consisted of simulating the dielectric constant of red tide and sea mixture, the sea surface roughness with red tide, and simulating a model between red tide and DDM peak SNR. Furthermore, green algae were detected from geostationary earth orbit-reflectometry (GEO-R) (Ban et al., 2022b) by using various reflection coefficients and roughness, and the effect of green algae on the GEO-R signal power was analyzed (Fig. 23). In turn, the GEO-R power was used to retrieve the green algae density through an empirical model.

#### Microplastics

GNSS-R's capability in detecting and imaging ocean microplastics utilizing CYGNSS data was demonstrated by Evans and Ruf (2021). Ocean microplastics' spatial distribution and temporal variability can be measured and mapped based on the GNSS-R microplastic retrieval method (e.g. Figure 24) (Evans & Ruf, 2021). In addition, the experimental study used statistical analysis of the reflectivity (phase and amplitude) with a very short integration time and was conducted to detect the accumulation of marine plastic litter (Gonga et al., 2023), while the analysis of the change observed in the reflected power did not show significant results.

#### Desert studies

The feasibility of leveraging CYGNSS data for retrieving information on desert roughness was demonstrated (Stilla et al., 2020). Their study on the Sahara

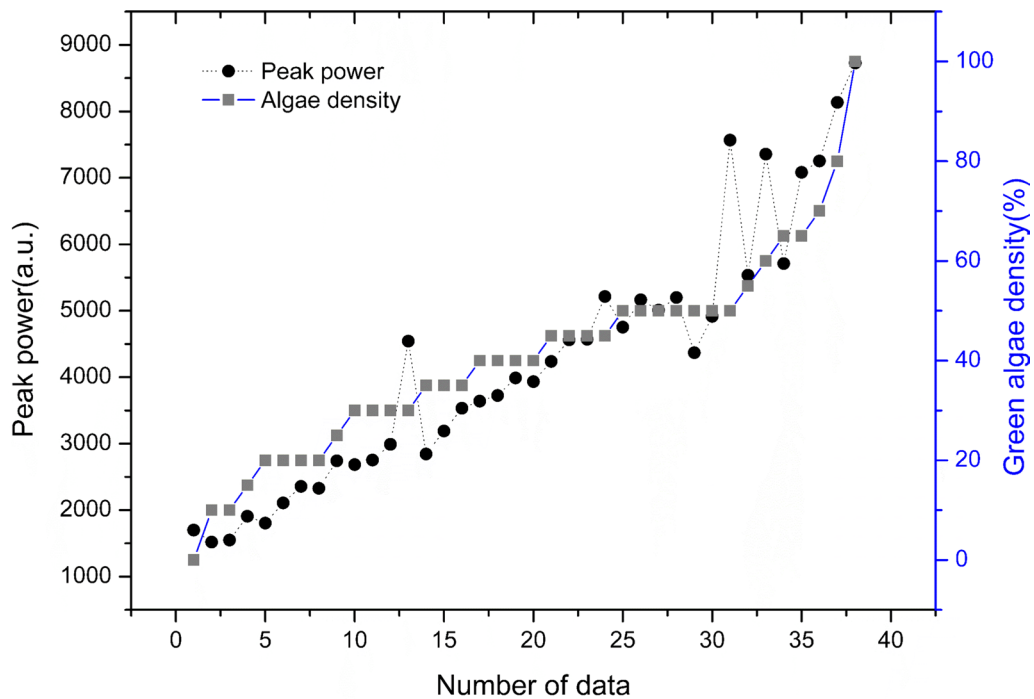


**Fig. 23** Observations of the GEO-R waveform peak power and green algae density values (Ban et al., 2022b)

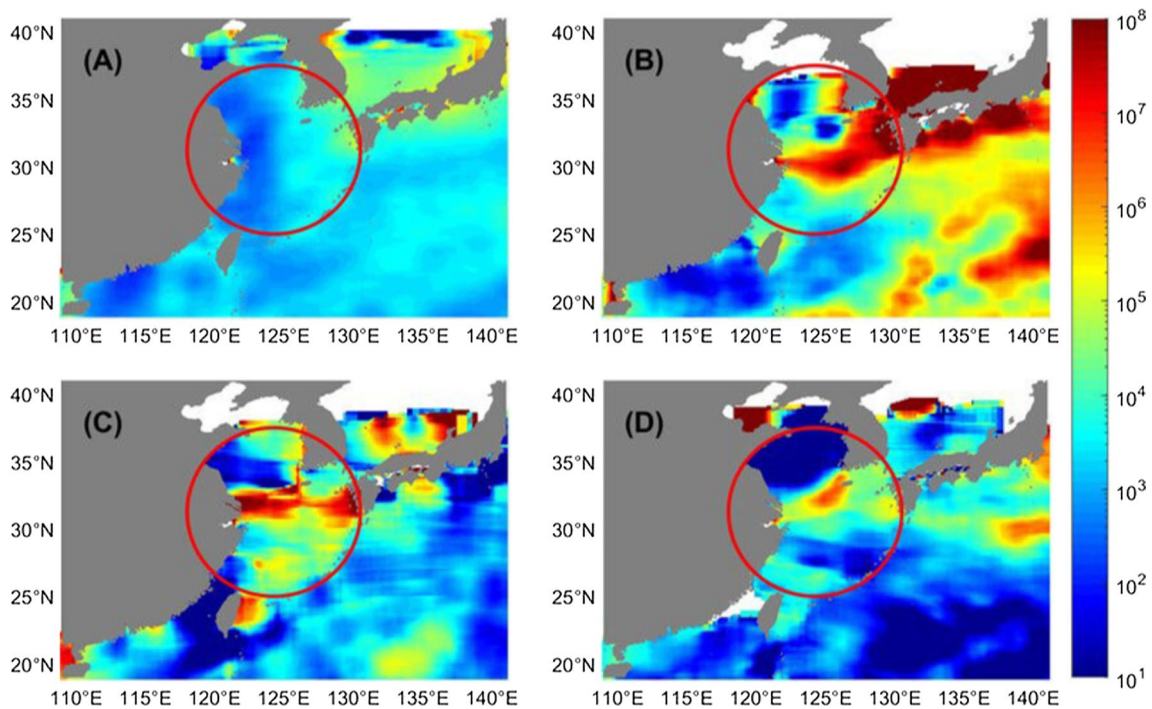


**Fig. 24** Estimated microplastic outflows into the East China Sea. **A** Annual average microplastics number density concentration ( $\#/km^2$ ,  $\log_{10}$  scale) serves as a reference. One week averages over **B** June 22, 2017–June 28, 2017, **C** October 27, 2017–November 2, 2017, and **D** December 2, 2017–December 8, 2017 reveal short-lived bursts of high microplastic concentration emerging from the Qiantang (b) and Yangtze (c) and (d) River mouths and dispersing into the East China Sea in the region highlighted by red circles (Evans & Ruf, 2021)



Desert identified reflectivity changes over time associated with various land surfaces (reliefs and dunes) (Fig. 25), indicating that the long-term average reflectivity could characterize surface properties. Their analysis revealed a robust correlation between CYGNSS data and SAR ALOS-2/PALSAR measurements. Furthermore, the analysis of the relationship between the CYGNSS and geometric or aerodynamic roughness was carried out. A strong correlation emerged between the surface parameters and the reflectivity. Finally, the four classes of aerodynamic roughness were shown for the Sahara, ranging from very smooth surfaces to mountainous surfaces (Stilla et al., 2020).

**Problems and challenges**

Although GNSS-R has been developed and widely used in ocean and land remote sensing, some problems still need to be improved or solved. For instance, a large number of works were performed to detect and measure

typhoons, however, some problems are still existed. The primary challenge involves enhancing the accuracy of high wind speed measurements during typhoons. At present, some artificial intelligence (AI) algorithms have been used in spaceborne GNSS-R retrieving wind speed and obtained better performances than the geophysical model functions (GMFs). It has been demonstrated that the GNSS signals have different responses to the high wind speed of typhoons from that of typhoon-free conditions, and therefore, developing a specialized AI model for high typhoon wind speed has the potential to enhance the retrieval precision of high typhoon wind speeds. The second problem is to improve the monitoring performance of typhoons. Due to the low signal power level, data quality control significantly decreases the temporal resolution of the CYGNSS. This decrease is adverse to the detection and measurement of typhoons. As known, above 130 GNSS satellites are in orbit, however, the CYGNSS only uses 31 GPS satellites. It is believed that

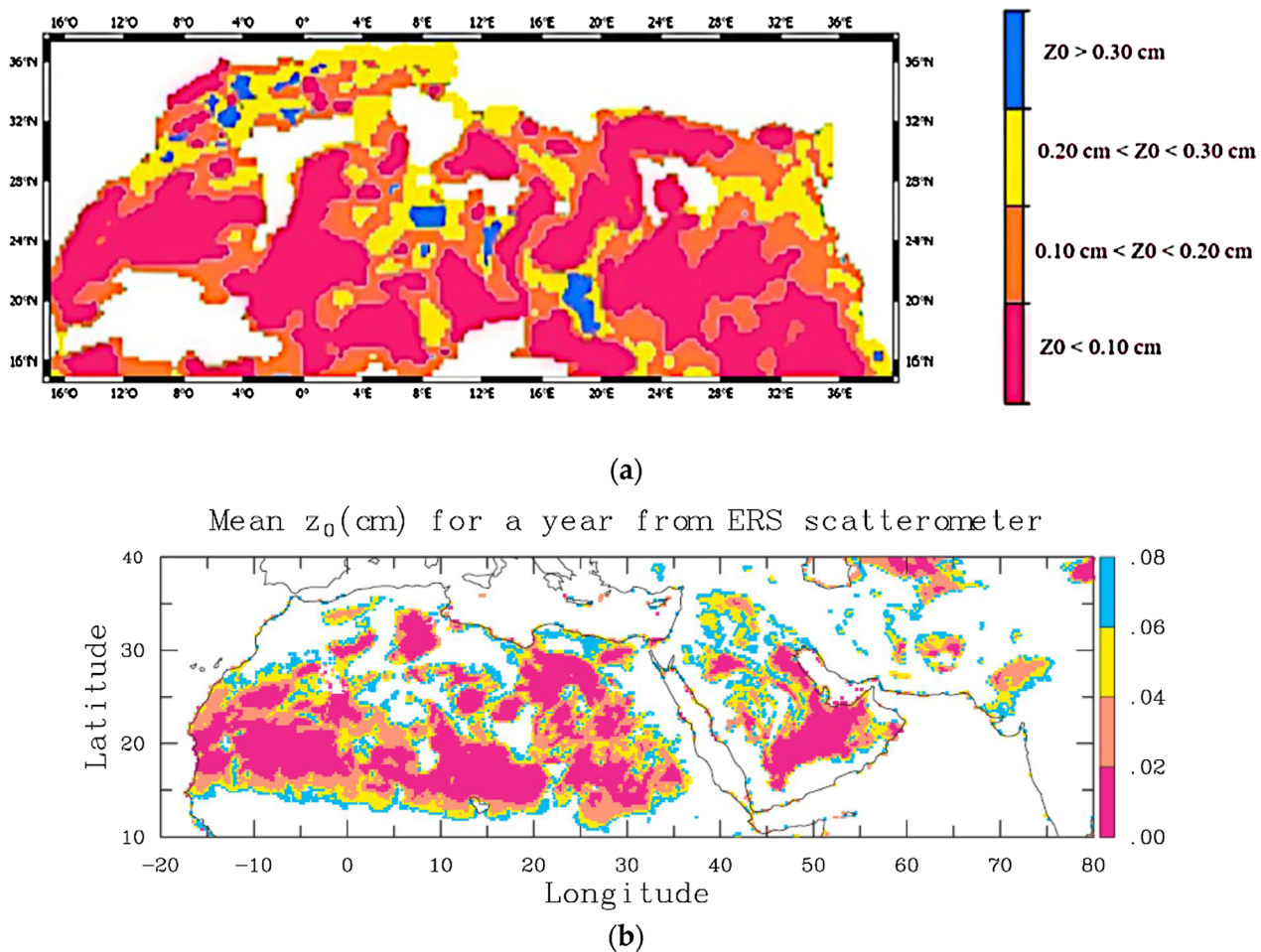


**Fig. 25** Aerodynamic roughness level maps over the Sahara desert: (a) derived from a CYGNSS reflectivity, (b) derived from the European Remote-Sensing Satellite (ERS) scatterometer (Prigent et al., 2005; Stilla et al., 2020)



multi-system GNSS-R can significantly increase the temporal resolution to more accurately monitor typhoons or tropical storms. This work was investigated by Alawwad & Elshafiey (2019). Another method to improve the performance of monitoring typhoons is to fuse the different data sources, such as spaceborne GNSS-R, altimeter, scatterometer, and radiometer. The third problem is that many works are based on the simulations, rather than the actually acquired data. Future works will continue demonstrations and assessments of those works using the actual acquired data from the CYGNSS and more future spaceborne missions.

GNSS-R is a promising technique for sea ice detection and characterization. However, there are still some challenges and open issues that need to be addressed in the future study. Some of these challenges are: improving the quality and availability of GNSS-R data, especially from spaceborne platforms, such as TechDemoSat-1 (retired) or FY-3, which can provide global and frequent observations of sea ice. More robust and accurate methods should be developed for sea ice detection and characterization, especially for complex and dynamic sea ice scenarios, such as marginal ice zones or leads and cracks. Integrating GNSS-R with other remote sensing techniques, such as SAR or PMR, can provide complementary information about sea ice properties, such as surface roughness or emissivity. Furthermore, GNSS-R methods should be validated and calibrated with ground truth or reference data, such as in situ measurements or numerical models, which can provide reliable estimations of sea ice properties, such as concentration or thickness.

In addition, monitoring floods by spaceborne GNSS-R, especially CYGNSS data still has some challenges in the current inversion process, which mainly include the following aspects: (1) Quasi-random distribution of data samples. Different from the traditional remote sensing satellite strip observation, CYGNSS observations are distributed "quasi-randomly" on the surface (due to the bistatic configuration of CYGNSS), although the coverage of observations is wider when compared with the former, the daily observations of CYGNSS may have obvious spatial "gaps" in a specific study area, i.e., not 100% coverage of the observed area. Therefore, for further comparisons and analyses, CYGNSS data must be integrated spatially and temporally. Currently, the vast majority of studies in CYGNSS terrestrial applications choose to grid the data to ensure a consistent spatial reference for time-domain analyses. However, achieving finer spatial grids consequently results in coarser temporal resolution (Al-Khalidi et al., 2020) (in order to ensure that a certain number of observations fall into each grid). Choosing the appropriate time window and grid size in conjunction with surface information is an important issue in

monitoring flooding using spaceborne GNSS-R data. (2) Surface Roughness, Vegetation Calibration. GNSS-R data are affected by surface roughness and vegetation in addition to the surface dielectric constant. Specifically, calm water bodies and moist soil increase the reflectivity, while surface roughness (microtopography) and microtopography decrease the reflectivity, while vegetation also attenuates the reflected signal strength. Therefore, eliminating the effects of roughness and vegetation should be the first consideration when using spaceborne GNSS-R data for water body detection. Current studies mostly used the surface roughness and vegetation parameters provided by SMAP or SMOS to calibrate the effects of both in the spaceborne GNSS-R data. However, 99.9% of SMAP roughness values at the 9 km scale are below 1.75 cm globally. The roughness parameters provided by SMAP may be underestimated when compared to the true surface roughness (Hornbuckle et al., 2017). Therefore, there is a need to explore more accurate surface roughness datasets that can be updated in real-time, or to explore new methods that can characterize roughness changes based on the spaceborne GNSS-R data itself. Similarly, the study of vegetation parameters that more accurately represent the attenuation effects of spaceborne GNSS-R signals is also an issue that must be addressed in the future.

Furthermore, the number of GNSS satellites will continue growing in the next decades. Today there are GNSS satellites in Medium Earth Orbit (MEO) as well as Geostationary Orbit (GEO). Future GNSS satellites may expand further into the lower MEO altitudes or even the Low Earth Orbit (LEO) region. The number of reflected signals from all these satellites will amount to several tens, as observed from LEO altitude. If it is taken into account that current space missions, flying or in development, can handle only up to the order of four reflection points in dual frequency and dual polarization (or an equivalent capability, like 16 reflection points in single frequency and single polarization) it becomes very clear GNSS-R has plenty of room for improvement ahead.

The key to increasing GNSS-R instrument capability to handle so many more simultaneous reflection points is on the one hand in the antenna design, and on the other hand, is the power of the digital Delay Doppler Map back-end. The use of dual-frequency dual-polarization multi-element antennas combined with digital beamforming seems to be a way in order to generate multiple high-gain beams, tracking each reflection point. High sampling rate digital circuits, implemented in FPGA or ASIC technology, together with high sampling rate Analog-to-Digital converters (of 3 bits as a minimum), are the technologies required in the fast-digital back-ends to produce the corresponding number of DDMs

on board. Alternatively, LEO-GEO optical links could be used to down-link to ground the raw measurements of each antenna element, eliminating the need for the digital beamforming and the digital back-end altogether.

There are also trade-offs to be made such as constellations of small satellites with performing GNSS-R as a function of the complexity for each spacecraft. For retrievals for which there are alternative solutions (like the microwave radiometers SMOS, Aquarius, and SMAP for soil moisture, scatterometers like those aboard ESA's METOP-SG, for wind over ocean, polarimetric Synthetic Aperture Radars like those on ESA Copernicus missions for wind in hurricanes, and interferometric radar altimeters like SWOT for mesoscale ocean altimetry, etc., ...) it is worthwhile to think about complementary aspects, that is, how these systems can benefit from each other. Some examples follow. Soil moisture retrieval using GNSS-R has been rather successful only because SMOS and SMAP soil moisture observations were available to first train and then validate the GNSS-R retrievals. Therefore, GNSS-R might always require a second independent microwave radiometer mission, to ensure the training and validity of its observations. Another example about the scatterometers and SWOT: how many GNSS-R satellites and how complex they should be to provide comparable wind and sea surface precision and coverage to those missions. Or, from another perspective, the question would turn into: how GNSS-R could enhance the revisit time of scatterometers (a few days) and SWOT (10 days), and what should be the number and complexity of such GNSS-R satellites?

A further well-deserved consideration is about the telecommunication mega-constellations. Those satellites are potential sources of opportunity. However, smarter techniques might be needed than those known today in the world of GNSS-R to convert them into useful sources of opportunity to retrieve meaningful remote sensing data from them.

### Concluding remarks

GNSS-R is an emerging means of remotely sensing oceans, land or glaciers, and snow fields using the reflected signals of the GNSS. As a long-term stable and free source of L-band signals, GNSS satellites fully leverage the advantages of the GNSS system, including all-weather, all-time, broad coverage, and high temporal and spatial resolution, etc. In particular, GNSS-R can be used to determine sea surface wind field, estimate sea-water salinity and sea surface oil spill in oceans, monitor soil moisture and plant growth in land and measure sea ice thickness, snow thickness, density, roughness, etc. In this paper, the current status and cutting-edge applications of GNSS-R are presented and discovered across

diverse fields such as oceanography, land monitoring, cryosphere, and atmospheric sciences. The latest advances in GNSS-R technology are reviewed and highlighted, including enhanced theoretical models, innovative instruments, and advanced signal processing techniques. Key application results and progresses are presented in details, such as wind speed, sea surface height, soil moisture and ice thickness. Furthermore, ongoing challenges and future prospects are addressed and discussed on GNSS-R technology and its emerging applications, potentially revolutionizing environmental monitoring and Earth observation. With the further development of GNSS-R technology, it may be possible to monitor natural disasters such as volcanoes, earthquake deformation, and landslides in the future. With the expansion of multi-frequency multi-GNSS constellations and space-based augmentation systems and the implementation of spaceborne GNSS reflection measurement missions (such as the upcoming HydroGNSS mission), one will get larger coverage and spatial-resolution surface feature information. In addition, more advanced GNSS-R receivers are in development: improved algorithms to meet different application requirements, and near real-time data processing ability to meet the needs of future space-based high-performance tasks (such as multi-mode GNSS reflection and Refraction Technology's next-generation Tri-GNSS receiver). In the next few years, it will be possible for the public to use low-cost satellites developed by some universities and other institutions, and the application of GNSS reflected signals in the field of remote sensing will also expand to a global scale.

### Acknowledgement

The authors would like to thank the editor and reviewers for the construction comments to improve our manuscript.

### Author contributions

All authors wrote and reviewed the manuscript. All authors read and approved the final manuscript.

### Funding

This work was supported by the Henan International Science and Technology Cooperation Key Project (Grant No. 241111520700) and Strategic Priority Research Program Project of the Chinese Academy of Sciences (Grant No. XDA23040100).

### Availability of data and materials

All figures were re-plot or used from the corresponding references.

### Declarations

### Competing interests

Shuanggen Jin is an editorial board member for *Satellite Navigation* and was not involved in the editorial review or decision to publish this article.

Received: 15 March 2024 Accepted: 26 April 2024

Published online: 27 May 2024

## References

- Alawwad, F., & Elshafiey, I. (2019). Hurricane monitoring using advanced GNSS reflectometry system (pp. 1053–1055). <https://doi.org/10.1109/APMC46564.2019.9038280>
- Al-Khaldi, M. M., Bringer, A., & Johnson, J. T. (2021a). Studies of a rapid change detector using CYGNSS level-2 wind speed products. *IEEE Journal of Selected Topics in Applied Earth Observations and Remote Sensing*, *14*, 7931–7937.
- Al-Khaldi, M. M., Johnson, J. T., Gleason, S., Chew, C. C., Gerlein-Safdi, C., Shah, R., & Zuffada, C. (2021b). Inland water body mapping using CYGNSS coherence detection. *IEEE Transactions on Geoscience and Remote Sensing*, *59*(9), 7385–7394.
- Al-Khaldi, M., Johnson, J., Kang, Y., Katzberg, S., Bringer, A., Kubatko, E., & Wood, D. (2019a). Track-based cyclone maximum wind retrievals using the Cyclone Global Navigation Satellite System (CYGNSS) mission full DDMS. *IEEE Journal of Selected Topics in Applied Earth Observations and Remote Sensing*, *PP*, 1–9. <https://doi.org/10.1109/JSTARS.2019.2946970>
- Al-Khaldi, M., Johnson, J., O'Brien, A., Balenzano, A., & Mattia, F. (2019b). Time-series retrieval of soil moisture using CYGNSS. *IEEE Transactions on Geoscience and Remote Sensing*, *PP*, 1–10. <https://doi.org/10.1109/TGRS.2018.2890646>
- Al-Khaldi, M., Shah, R., Chew, C., Johnson, J., & Gleason, S. (2020). Mapping the dynamics of the South Asian monsoon using CYGNSS's Level-1 signal coherence. *IEEE Journal of Selected Topics in Applied Earth Observations and Remote Sensing*, *PP*, 1. <https://doi.org/10.1109/JSTARS.2020.3042170>
- Alonso-Arroyo, A., Camps, A., Aguasca, A., Forte, G., Moneris, A., Rüdiger, C., Walker, J. P., Park, H., Pascual, D., & Onrubia, R. (2014). Improving the accuracy of soil moisture retrievals using the phase difference of the dual-polarization GNSS-R interference patterns. *IEEE Geoscience and Remote Sensing Letters*, *11*(12), 2090–2094. <https://doi.org/10.1109/LGRS.2014.2320052>
- Alonso-Arroyo, A., Zavorotny, V. U., & Camps, A. (2017). Sea ice detection using UK TDS-1 GNSS-R data. *IEEE Transactions on Geoscience and Remote Sensing*, *55*(9), 4989–5001.
- Arabi, S., Asgarimehr, M., Kada, M., & Wickert, J. (2023). Hybrid CNN-LSTM deep learning for track-wise GNSS-R ocean wind speed retrieval. *Remote Sensing*, *15*, 4169. <https://doi.org/10.3390/rs15174169>
- Arroyo, A. A., Camps, A., Aguasca, A., Forte, G. F., Moneris, A., Rüdiger, C., Walker, J. P., Park, H., Pascual, D., & Onrubia, R. (2014). Dual-polarization GNSS-R interference pattern technique for soil moisture mapping. *IEEE Journal of Selected Topics in Applied Earth Observations and Remote Sensing*, *7*(5), 1533–1544.
- Asner, G. (2001). Cloud cover in Landsat observations of the Brazilian Amazon. *International Journal of Remote Sensing*, *22*, 3855–3862. <https://doi.org/10.1080/01431160010006926>
- Auber, J.-C., Bibaut, A., & Rigal, J.-M. (1994). Characterization of multipath on land and sea at GPS frequencies. In *Proceedings of the 7th international technical meeting of the satellite division of the institute of navigation (ION GPS 1994)* (pp. 1155–1171).
- Bai, X., & Tan, S. (2020). Exploring signal of opportunity from GNSS for snow remote sensing. *AGU Fall Meeting Abstracts*, 2020, C005-0001.
- Ban, W., Zhang, K., Yu, K., Zheng, N., & Chen, S. (2022a). Detection of red tide over sea surface using GNSS-R spaceborne observations. *IEEE Transactions on Geoscience and Remote Sensing*, *PP*, 1. <https://doi.org/10.1109/TGRS.2022.3144289>
- Ban, W., Zheng, N., Yu, K., Zhang, K., & Liu, J. (2022b). Sea Surface green algae density estimation using ship-borne GEO-satellite reflection observations. *IEEE Geoscience and Remote Sensing Letters*, *19*, 1. <https://doi.org/10.1109/LGRS.2022.3198253>
- Bates, P. (2004). Remote sensing and flood inundation modelling. *Hydrological Processes*, *18*, 2593–2597. <https://doi.org/10.1002/hyp.5649>
- Breiman, L. (2017). *Classification and regression trees*. Routledge.
- Calabia, A., Molina, I., & Jin, S. (2020). Soil moisture content from GNSS reflectometry using dielectric permittivity from fresnel reflection coefficients. *Remote Sensing*, *12*, 122. <https://doi.org/10.3390/rs12010122>
- Camps A, Munoz-Martin J, Ruiz-de-Azua J, Fernandez L, Perez-Portero A, Llaveria D, Herbert C, Pablos M, Golkar, A, Gutierrez A, Antonio C, Bandeiras J, Andrade J, Cordeiro D, Briatore S, Garzaniti N, Nichele F, Mozzillo R, Piumatti A, Cardi M, Esposito M, van Dijk C, Verduyssen N, Barbosa J, Hefeles J, Koeleman R, Dominguez B, Pastena M, Filippazzo G Reagan, A. (2022). FSSCat: The Federated Satellite Systems <sup>3</sup>Cat Mission: Demonstrating the capabilities of CubeSats to monitor essential climate variables of the water cycle [Instruments and Missions], in *IEEE Geoscience and Remote Sensing Magazine*, *10*(4), 260–269. <https://doi.org/10.1109/MGRS.2022.3219778>.
- Camps, A., Park, H., Pablos, M., Foti, G., Gommenginger, C. P., Liu, P.-W., & Judge, J. (2016). Sensitivity of GNSS-R spaceborne observations to soil moisture and vegetation. *IEEE Journal of Selected Topics in Applied Earth Observations and Remote Sensing*, *9*(10), 4730–4742.
- Cardellach, E., Fabra, F., Nogués-Correig, O., Oliveras, S., Ribó, S., & Rius, A. (2011). GNSS-R ground-based and airborne campaigns for ocean, land, ice, and snow techniques: Application to the GOLD-RTR data sets. *Radio Science*, *46*(06), 1–16.
- Cardellach, E., Fabra, F., Rius, A., Pettinato, S., & D'Addio, S. (2012). Characterization of dry-snow sub-structure using GNSS reflected signals. *Remote Sensing of Environment*, *124*, 122–134.
- Cardellach, E., Nan, Y., Li, W., Padullés, R., Ribó, S., & Rius, A. (2020). Variational retrievals of high winds using uncalibrated CyGNSS observables. *Remote Sensing*, *12*(23), 3930. <https://doi.org/10.3390/rs12233930>
- Cardellach, E., Ruffini, G., Pino, D., Rius, A., Komjathy, A., & Garrison, J. L. (2003). Mediterranean balloon experiment: Ocean wind speed sensing from the stratosphere, using GPS reflections. *Remote Sensing of Environment*, *88*(3), 351–362.
- Carreno-Luengo, H., Camps, A., Ramos-Perez, I., & Rius, A. (2014). Experimental evaluation of GNSS-reflectometry altimetric precision using the P(Y) and C/A signals. *IEEE Journal of Selected Topics in Applied Earth Observations and Remote Sensing*, *7*, 1493–1500. <https://doi.org/10.1109/JSTARS.2014.2320298>
- Carreno-Luengo, H., Camps, A., Via, P., Munoz, J. F., Cortiella, A., Vidal, D., Jané, J., Catarino, N., Hagenfeldt, M., Palomo, P., et al. (2016). 3Cat-2—An experimental nanosatellite for GNSS-R earth observation: Mission concept and analysis. *IEEE Journal of Selected Topics in Applied Earth Observations and Remote Sensing*, *9*(10), 4540–4551.
- Carreno-Luengo, H., Lowe, S., Zuffada, C., Esterhuizen, S., & Oveisgharan, S. (2017). Spaceborne GNSS-R from the SMAP mission: First assessment of polarimetric scatterometry over land and cryosphere. *Remote Sensing*, *9*(4), 362.
- Carreno-Luengo, H., Luzi, G., & Crosetto, M. (2020). Above-ground biomass retrieval over tropical forests: A novel GNSS-R approach with CyGNSS. *Remote Sensing*, *12*(9), 1368.
- Chen, X., Valencia, R., Soleymani, A., & Scott, K. A. (2023). Predicting sea ice concentration with uncertainty quantification using passive microwave and reanalysis data: A case study in Baffin Bay. *IEEE Transactions on Geoscience and Remote Sensing*, *61*, 1–13.
- Chew, C. (2021). Spatial interpolation based on previously- observed behavior: a framework for interpolating spaceborne GNSS-R data from CYGNSS. *Journal of Spatial Science*, *68*, 155–168. <https://doi.org/10.1080/104498596.2021.1942253>
- Chew, C., Reager, J., & Small, E. (2018). CYGNSS data map flood inundation during the 2017 Atlantic hurricane season. *Scientific Reports*, *8*, 9336. <https://doi.org/10.1038/s41598-018-27673-x>
- Chew, C. C., & Small, E. E. (2018). Soil moisture sensing using spaceborne GNSS reflections: Comparison of CYGNSS reflectivity to SMAP soil moisture. *Geophysical Research Letters*, *45*(9), 4049–4057.
- Chew, C., & Small, E. (2020). Description of the UCAR/CU soil moisture product. *Remote Sensing*, *12*, 1558. <https://doi.org/10.3390/rs12101558>
- Chew, C., Small, E. E., & Larson, K. M. (2016). An algorithm for soil moisture estimation using GPS-interferometric reflectometry for bare and vegetated soil. *GPS Solutions*, *20*, 525–537.
- Clarizia, M. P., Pierdicca, N., Costantini, F., & Floury, N. (2019). Analysis of CYGNSS data for soil moisture retrieval. *IEEE Journal of Selected Topics in Applied Earth Observations and Remote Sensing*, *PP*, 1–9. <https://doi.org/10.1109/JSTARS.2019.2895510>
- Clarizia, M. P., & Ruf, C. S. (2016). Wind speed retrieval algorithm for the Cyclone Global Navigation Satellite System (CYGNSS) mission. *IEEE Transactions on Geoscience and Remote Sensing*, *54*(8), 4419–4432.
- Clarizia, M. P., & Ruf, C. S. (2017). Bayesian wind speed estimation conditioned on significant wave height for GNSS-R ocean observations. *Journal of Atmospheric and Oceanic Technology*, *34*(6), 1193–1202. <https://doi.org/10.1175/JTECH-D-16-0196.1>

- Clarizia, M. P., & Ruf, C. (2020). Statistical derivation of wind speeds from CYGNSS data. *IEEE Transactions on Geoscience and Remote Sensing*, *PP*, 1–10. <https://doi.org/10.1109/TGRS.2019.2959715>
- Clarizia, M. P., Ruf, C., Jales, P., & Gommenginger, C. (2014). Spaceborne GNSS-R minimum variance wind speed estimator. *IEEE Transactions on Geoscience and Remote Sensing*, *52*, 6829–6843. <https://doi.org/10.1109/TGRS.2014.2303831>
- Cox, C., & Munk, W. (1954). Measurement of the Roughness of the Sea Surface from Photographs of the Sun's Glitter. *Journal of the Optical Society of America*, *44*(11), 838–850. <https://doi.org/10.1364/JOSA.44.000838>
- Dielacher, A., Fagner, H., Moritsch, M., et al. (2019). The passive reflectometer on board of PRETTY. In *Proceedings of the ESA ARSI+KEO conference*.
- Dobson, M. C., Ulaby, F. T., Hallikainen, M. T., & El-Rayes, M. A. (1985). Microwave dielectric behavior of wet soil-Part II: Dielectric mixing models. *IEEE Transactions on Geoscience and Remote Sensing*, *1*, 35–46.
- Dong, Z., & Jin, S. G. (2021). Evaluation of the land GNSS-Reflected DDM coherence on soil moisture estimation from CYGNSS data. *Remote Sens.*, *13*(4), 570. <https://doi.org/10.3390/rs13040570>
- Downs, B., Kettner, A., Chapman, B., Brakenridge, R., O'Brien, A., & Zuffada, C. (2023). Assessing the relative performance of GNSS-R flood extent observations: Case study in South Sudan. *IEEE Transactions on Geoscience and Remote Sensing*, *12*, 1. <https://doi.org/10.1109/TGRS.2023.3237461>
- Edokossi, K., Calabria, A., Jin, S., & Molina, I. (2020). GNSS-reflectometry and remote sensing of soil moisture: A review of measurement techniques, methods, and applications. *Remote Sensing*, *12*(4), 614. <https://doi.org/10.3390/rs12040614>
- Egido, A. (2013). *GNSS reflectometry for land remote sensing applications*. <https://doi.org/10.13140/RG.2.1.2078.7049>
- Egido, A., Caparrini, M., Ruffini, G., Paloscia, S., Santi, E., Guerriero, L., Pierdicca, N., & Floury, N. (2012). Global navigation satellite systems reflectometry as a remote sensing tool for agriculture. *Remote Sensing*, *4*(8), 2356–2372.
- Egido, A., Paloscia, S., Motte, E., Guerriero, L., Pierdicca, N., Caparrini, M., Santi, E., Fontanelli, G., & Floury, N. (2014). Airborne GNSS-R polarimetric measurements for soil moisture and above-ground biomass estimation. *IEEE Journal of Selected Topics in Applied Earth Observations and Remote Sensing*, *7*(5), 1522–1532.
- Entekhabi, D., Njoku, E. G., O'Neill, P. E., Kellogg, K. H., Crow, W. T., Edelstein, W. N., Entin, J. K., Goodman, S. D., Jackson, T. J., Johnson, J., Kimball, J., Piepmeier, J. R., Koster, R. D., Martin, N., McDonald, K. C., Moghaddam, M., Moran, S., Reichle, R., Shi, J. C., ... Van Zyl, J. (2010). The soil moisture active passive (SMAP) mission. *Proceedings of the IEEE*, *98*(5), 704–716. <https://doi.org/10.1109/JPROC.2010.2043918>
- Eric, S., Shanafield, M., Hammond, J., Sefton, C., Leigh, C., & Detry, T. (2021). Classification and trends in intermittent river flow regimes in Australia, northwestern Europe and USA: A global perspective. *Journal of Hydrology*, *597*, 126170. <https://doi.org/10.1016/j.jhydrol.2021.126170>
- Eroglu, O., Kurum, M., Boyd, D. R., & Gürbüz, A. C. (2019). High spatio-temporal resolution CYGNSS soil moisture estimates using artificial neural networks. *Remote Sensing*, *11*, 2272.
- Evans, M., & Ruf, C. (2021). Toward the detection and imaging of ocean microplastics with a spaceborne radar. *IEEE Transactions on Geoscience and Remote Sensing*, *PP*, 1–9. <https://doi.org/10.1109/TGRS.2021.3081691>
- Fabra, F., Cardellach, E., Rius, A., Ribo, S., Oliveras, S., Nogués-Correig, O., Rivas, M. B., Semmling, M., & D'Addio, S. (2011). Phase altimetry with dual polarization GNSS-R over sea ice. *IEEE Transactions on Geoscience and Remote Sensing*, *50*(6), 2112–2121.
- Foti, G., Gommenginger, C., & Srokosz, M. (2017). First Spaceborne GNSS-reflectometry observations of Hurricanes from the UK TechDemoSat-1 Mission. *Geophysical Research Letters*, *44*, 12358–12366. <https://doi.org/10.1002/2017GL076166>
- Frappart, F., Zeiger, P., Betbeder, J., Gond, V., Bellot, R., Baghdadi, N., Blarel, F., Darrozes, J., Bourrel, L., & Seyler, F. (2021). Automatic detection of inland water bodies along altimetry tracks for estimating surface water storage variations in the Congo Basin. *Remote Sensing*, *13*(19), 3804.
- Fu, L.-L., Chelton, D. B., Le Traon, P.-Y., & Morrow, R. (2010). Eddy dynamics from satellite altimetry. *Oceanography*, *23*(4), 14–25.
- Gao, H., Yang, D., Zhang, B., Wang, Q., & Wang, F. (2017). Remote Sensing of Sea Ice Thickness with GNSS Reflected Signal. *Dianzi Yu Xinxi Xuebao/Journal of Electronics and Information Technology*, *39*, 1096–1100. <https://doi.org/10.11999/JEIT160765>
- Garrison, J. L., Komjathy, A., Zavorotny, V. U., & Katzberg, S. J. (2002). Wind speed measurement using forward scattered GPS signals. *IEEE Transactions on Geoscience and Remote Sensing*, *40*(1), 50–65.
- Geremia-Nievinski, F., & Larson, K. (2013). Forward modeling of GPS multipath for near-surface reflectometry and positioning applications. *GPS Solutions*. <https://doi.org/10.1007/s10291-013-0331-y>
- Gleason, S., Gommenginger, C., & Cromwell, D. (2010). Fading statistics and sensing accuracy of ocean scattered GNSS and altimetry signals. *Advances in Space Research - ADV SPACE RES*, *46*, 208–220. <https://doi.org/10.1016/j.asr.2010.03.023>
- Gleason, S., Hodgart, S., Sun, Y., Gommenginger, C., Mackin, S., Adjrad, M., & Unwin, M. (2005). Detection and processing of bistatically reflected GPS signals from low earth orbit for the purpose of ocean remote sensing. *IEEE Transactions on Geoscience and Remote Sensing*, *43*(6), 1229–1241. <https://doi.org/10.1109/TGRS.2005.845643>
- Gonga, A., Pérez-Portero, A., Camps, A., Pascual, D., de Fockert, A., & de Maagt, P. (2023). GNSS-R observations of marine plastic litter in a water flume: An experimental study. *Remote Sensing*, *15*(3), 637.
- Guan, D., Camps, A., & Park, H. (2019). Hurricane Observations with GNSS-Reflectometry from CYGNSS Mission—Case Study of Hurricane Irma 2017 (pp. 9875–9878). <https://doi.org/10.1109/IGARSS.2019.8898491>
- Guo, W., Du, H., Cheong, J. W., Southwell, B., & Dempster, A. (2021). GNSS-R wind speed retrieval of sea surface based on particle swarm optimization algorithm. *IEEE Transactions on Geoscience and Remote Sensing*, *PP*, 1–14. <https://doi.org/10.1109/TGRS.2021.3082916>
- Haase, J. S., Xie, F., Muradyan, P., Garrison, J. L., Lulich, T., Voo, J., & Larson, K. M. (2008). New atmospheric observations from the airborne GNSS instrument system for multistatic and occultation sensing (GISMOS). *AGU Fall Meeting Abstracts*, 2008, G41A-0595.
- Haji, G. A., & Zuffada, C. (2003). Theoretical description of a bistatic system for ocean altimetry using the GPS signal. *Radio Science*, *38*(5), 10–11.
- Hall, C., & Cordey, R. A. (1988). Multistatic Scatterometry. *International Geoscience and Remote Sensing Symposium, 'Remote Sensing: Moving Toward the 21st Century'*, *1*, 561–562.
- He, Z., Yang, Y., & Chen, W. (2020). A hybrid integration method for moving target detection with GNSS-based passive radar. *IEEE Journal of Selected Topics in Applied Earth Observations and Remote Sensing*, *12*, 1. <https://doi.org/10.1109/JSTARS.2020.3037200>
- Hein, G. (2020). Status, perspectives and trends of satellite navigation. *Satellite Navigation*, *1*, 22. <https://doi.org/10.1186/s43020-020-00023-x>
- Helm, A., Montenbruck, O., Ashjaee, J., Yudanov, S., Beyerle, G., Stosius, R., & Rothacher, M. (2007). GORS-A GNSS occultation, reflectometry and scatterometry space receiver. In *Proceedings of the 20th International Technical Meeting of the Satellite Division of The Institute of Navigation (ION GNSS 2007)*, 2011–2021.
- Helm, A. (2008). *Ground-based GPS altimetry with the L1 OpenGPS receiver using carrier phase-delay observations of reflected GPS signals*. Deutsches GeoForschungsZentrum GFZ Potsdam.
- Hirabayashi, Y., Roobavannan, M., Koirala, S., Konoshima, L., Yamazaki, D., Watanabe, S., Kim, H., & Kanae, S. (2013). Global flood risk under climate change. *Nature Climate Change*, *3*, 816–821. <https://doi.org/10.1038/nclimate1911>
- Hornbuckle, B., Walker, V., Eichinger, B., Wallace, V., & Yildirim, E. (2017). *Soil surface roughness observed during SMAPVEX16-IA and its potential consequences for SMOS and SMAP*. 2027–2030. <https://doi.org/10.1109/IGARSS.2017.8127379>
- Hoseini, M., Asgarimehr, M., Zavorotny, V., Nahavandchi, H., Ruf, C., & Wickert, J. (2020). First evidence of mesoscale ocean Eddies signature in GNSS reflectometry measurements. *Remote Sensing*, *12*, 542. <https://doi.org/10.3390/rs12030542>
- Hu, C., Benson, C., Park, H., Camps, A., Qiao, L., & Rizos, C. (2019). Detecting targets above the earth's surface using GNSS-R delay doppler maps: Results from TDS-1. *Remote Sensing*, *11*, 2327. <https://doi.org/10.3390/rs11192327>
- Hu, C., Benson, C., Rizos, C., & Qiao, L. (2017). Single-pass sub-meter space-based GNSS-R ice altimetry: Results from TDS-1. *IEEE Journal of Selected Topics in Applied Earth Observations and Remote Sensing*, *10*(8), 3782–3788.



- Hu, Y., Jiang, Z., Yuan, X., Hua, X., & Liu, W. (2024). Isometric mapping algorithm based GNSS-R sea ice detection. *Metascience in Aerospace*, 1(1), 38–52. <https://doi.org/10.3934/mina.2024002>
- Huang, F., Garrison, J., Leidner, S., Annane, B., Hoffman, R., Giuseppe, G., & Stofelen, A. (2020). A forward model for data assimilation of GNSS ocean reflectometry Delay-Doppler maps. *IEEE Transactions on Geoscience and Remote Sensing*, PP, 1–14. <https://doi.org/10.1109/TGRS.2020.3002801>
- Huang, F., Garrison, J., Rodriguez-Alvarez, N., O'Brien, A., Schoenfeldt, K., Ho, S., & Zhang, H. (2019). Sequential processing of GNSS-R delay-doppler maps to estimate the ocean surface wind field. *IEEE Transactions on Geoscience and Remote Sensing*, PP, 1–16. <https://doi.org/10.1109/TGRS.2019.2931847>
- Huang, F., Xia, J., Yin, C., Zhai, X., Xu, N., Yang, G., Bai, W., Sun, Y., Du, Q., Liao, M., et al. (2022). Assessment of FY-3E GNOSS-IIGNSS-R global wind product. *IEEE Journal of Selected Topics in Applied Earth Observations and Remote Sensing*, 15, 7899–7912.
- Jia, Y. (2018). *Remote sensing in land applications by using GNSS-reflectometry*. IntechOpen.
- Jia, Y., Jin, S., Chen, H., Yan, Q., Savi, P., Jin, Y., & Yuan, Y. (2021). Temporal-spatial soil moisture estimation from CYGNSS using machine learning regression with a preclassification approach. *IEEE Journal of Selected Topics in Applied Earth Observations and Remote Sensing*, PP, 1. <https://doi.org/10.1109/JSTARS.2021.3076470>
- Jia, Y., Jin, S., Savi, P., Gao, Y., Tang, J., Chen, Y., & Li, W. (2019). GNSS-R soil moisture retrieval based on a XGboost machine learning aided method: Performance and validation. *Remote Sensing*, 11(14), 1655.
- Jia, Y., Jin, S., Yan, Q., Savi, P., Zhang, R., & Li, W. (2022). An effective land type labeling approach for independently exploiting high-resolution soil moisture products based on CYGNSS data. *IEEE Journal of Selected Topics in Applied Earth Observations and Remote Sensing*, 15, 4234–4247.
- Jia, Y., Savi, P., Canone, D., & Notarpietro, R. (2016). Estimation of surface characteristics using GNSS LH-reflected signals: Land versus water. *IEEE Journal of Selected Topics in Applied Earth Observations and Remote Sensing*, 9(10), 4752–4758.
- Jin, S., Zhang, Q., & Qian, X. (2017b). New Progress and Application Prospects of Global Navigation Satellite System Reflectometry (GNSS+R). *Cehui Xuebao/Acta Geodaetica et Cartographica Sinica*, 46, 1389–1398. <https://doi.org/10.11947/j.AGCS.2017.20170282>
- Jin, S., Feng, G., & Gleason, S. (2011). Remote sensing using GNSS signals: Current status and future directions. *Advances in Space Research*, 47(10), 1645–1653. <https://doi.org/10.1016/j.asr.2011.01.036>
- Jin, S., & Komjathy, A. (2010). GNSS reflectometry and remote sensing: New objectives and results. *Advances in Space Research*, 46(2), 111–117.
- Jin, S., Qian, X., & Wu, X. (2017a). Sea level change from BeiDou Navigation Satellite System-Reflectometry (BDS-R): First results and evaluation. *Global and Planetary Change*, 149, 20–25.
- Jing, C., Niu, X., Duan, C., Lu, F., Di, G., & Yang, X. (2019). Sea surface wind speed retrieval from the first Chinese GNSS-R mission: Technique and preliminary results. *Remote Sensing*, 11(24), 3013.
- Jonkman, S. N. (2005). Global Perspectives on Loss of Human Life Caused by Floods. *Natural Hazards*, 34, 151–175. <https://doi.org/10.1007/s11069-004-8891-3>
- Juang, J., Ma, S.-H., & Lin, C.-T. (2016). Study of GNSS-R techniques for FORMOSAT mission. *IEEE Journal of Selected Topics in Applied Earth Observations and Remote Sensing*, 9, 4582–4592.
- Katzberg, S. J., & Garrison, J. L. (1996). Utilizing GPS to determine ionospheric delay over the ocean.
- Katzberg, S., Dunion, J., & Ganoe, G. (2013). The use of reflected GPS signals to retrieve ocean surface wind speeds in tropical cyclones. *Radio Science*, 48, 371–387. <https://doi.org/10.1002/rds.20042>
- Katzberg, S. J., Torres, O., & Ganoe, G. (2006a). Calibration of reflected GPS for tropical storm wind speed retrievals. *Geophysical Research Letters*, 33(18), L18602.
- Katzberg, S. J., Torres, O., Grant, M. S., & Masters, D. (2006b). Utilizing calibrated GPS reflected signals to estimate soil reflectivity and dielectric constant: Results from SMEX02. *Remote Sensing of Environment*, 100(1), 17–28.
- Katzberg, S., Walker, R., Roles, J., Lynch, T., & Black, P. (2001). First GPS signals reflected from the interior of a tropical storm: Preliminary results from Hurricane Michael. *Geophysical Research Letters - GEOPHYS RES LETT*, 28, 1981–1984. <https://doi.org/10.1029/2000GL012823>
- Kim, H., & Lakshmi, V. (2018). Use of Cyclone Global Navigation Satellite System (CYGNSS) observations for estimation of soil moisture. *Geophysical Research Letters*, 45, 8272–8282. <https://doi.org/10.1029/2018GL078923>
- Klemas, V. (2015). Remote sensing of floods and flood-prone areas: An overview. *Journal of Coastal Research*, 31, 1005–1013. <https://doi.org/10.2112/JCOASTRES-D-14-00160.1>
- Klemas, V., Finkl, C. W., & Kabbara, N. (2014). Remote sensing of soil moisture: An overview in relation to coastal soils. *Journal of Coastal Research*, 30(4), 685–696.
- Komjathy, A., Maslanik, J., Zavorotny, V. U., Axelrad, P., & Katzberg, S. J. (2000). Sea ice remote sensing using surface reflected GPS signals. In *IGARSS 2000 international geoscience and remote sensing symposium. Taking the pulse of the planet: The role of remote sensing in managing the environment. Proceedings (Cat. No. 00CH37120)*, 7, 2855–2857.
- Kucwaj, J.-C., Reboul, S., Stienne, G., Choquel, J.-B., & Benjelloun, M. (2017). Circular regression applied to GNSS-R phase altimetry. *Remote Sensing*, 9(7), 651.
- Lan, X., Wang, L., Jinxing, L., Jiang, W., & Min, Z. (2021). Maritime multiple moving target detection using multiple-BDS-based radar: Doppler phase compensation and resolution improvement. *Remote Sensing*, 13, 4963. <https://doi.org/10.3390/rs13244963>
- Larson, K., Braun, J., Small, E., Zavorotny, V., Gutmann, E., & Bilich, A. (2010). GPS multipath and its relation to near-surface soil moisture content. *Selected Topics in Applied Earth Observations and Remote Sensing, IEEE Journal of*, 3, 91–99. <https://doi.org/10.1109/JSTARS.2009.2033612>
- Larson, K. M., Gutmann, E. D., Zavorotny, V. U., Braun, J. J., Williams, M. W., & Nievinski, F. G. (2009). Can we measure snow depth with GPS receivers? *Geophysical Research Letters*, 36(17), L17502.
- Larson, K. M., MacFerrin, M., & Nylen, T. (2020). Brief Communication: Update on the GPS reflection technique for measuring snow accumulation in Greenland. *The Cryosphere*, 14(6), 1985–1988.
- Larson, K. M., & Nievinski, F. G. (2013). GPS snow sensing: Results from the EarthScope Plate Boundary Observatory. *GPS Solutions*, 17, 41–52.
- Lei, F., Senyurek, V., Kurum, M., Gurbuz, A., Boyd, D., Moorhead, R., Crow, W., & Eroglu, O. (2022). Quasi-global machine learning-based soil moisture estimates at high spatio-temporal scales using CYGNSS and SMAP observations. *Remote Sensing of Environment*, 276, 113041. <https://doi.org/10.1016/j.rse.2022.113041>
- Li, W., Yang, D., Fabra, F., Yunchang, C., & Yang, W. (2014b). Typhoon wind speed observation utilizing reflected signals from BeiDou GEO satellites. In *Lecture Notes in Electrical Engineering* (Vol. 303, pp. 191–200). [https://doi.org/10.1007/978-3-642-54737-9\\_18](https://doi.org/10.1007/978-3-642-54737-9_18)
- Li, C., Huang, W., & Gleason, S. (2015). Dual antenna space-based GNSS-R ocean surface mapping: oil slick and tropical cyclone sensing. *IEEE Journal of Selected Topics in Applied Earth Observations and Remote Sensing*, 8, 425–435. <https://doi.org/10.1109/JSTARS.2014.2341581>
- Li, H., Xia, Q., Yin, C., & Wan, W. (2014a). The current status of research on GNSS-R remote sensing technology in china and future development. *Journal of Radars*, 2, 389–399. <https://doi.org/10.3724/SP.J.1300.2013.13080>
- Li, W., Cardellach, E., Fabra, F., Rius, A., Ribó, S., & Martin-Neira, M. (2017). First spaceborne phase altimetry over sea ice using TechDemoSat-1 GNSS-R signals. *Geophysical Research Letters*, 44(16), 8369–8376.
- Li, W., Fabra, F., Yang, D., Rius, A., Martin-Neira, M., Yin, C., Wang, Q., & Yunchang, C. (2016). Initial results of typhoon wind speed observation using coastal GNSS-R of BeiDou GEO satellite. *IEEE Journal of Selected Topics in Applied Earth Observations and Remote Sensing*, 9, 1–10. <https://doi.org/10.1109/JSTARS.2016.2523126>
- Li, Z., Guo, F., Chen, F., Zhang, Z., & Zhang, X. (2023). Wind speed retrieval using GNSS-R technique with geographic partitioning. *Satellite Navigation*, 4(1), 4.
- Liu, Q., Zhang, S., Nan, Y., & Ma, Z. (2021). Flood detection of south asia using spaceborne GNSS-R coherent signals. *Geomatics and Information Science of Wuhan University*, 46(11), 1641–1648.
- Li, Z., Huang, C., Sun, Z., An, H., Wu, J., & Yang, J. (2021). BeiDou-based passive multistatic radar maritime moving target detection technique via space-time hybrid integration processing. *IEEE Transactions on Geoscience and Remote Sensing*, 60, 1–13.
- Liu, X., Bai, W., Tan, G., Huang, F., Xia, J., Yin, C., Sun, Y., Du, Q., Meng, X., Liu, C., & Hu, P. (2023). GNSS-R global sea surface wind speed retrieval based on deep learning. *IEEE Transactions on Geoscience and Remote Sensing*, 61, 3309690. <https://doi.org/10.1109/TGRS.2023.3309690>

- Loria, E., O'Brien, A., Zavorotny, V., Lavelle, M., Chew, C., Shah, R., & Zuffada, C. (2019). Analysis of wetland extent retrieval accuracy using CYGNSS. In *IGARSS 2019–2019 IEEE international geoscience and remote sensing symposium* (pp. 8684–8687).
- Ma, H., Antoniou, M., & Cherniakov, M. (2015). Passive GNSS-based SAR resolution improvement using joint Galileo E5 signals. *IEEE Geoscience and Remote Sensing Letters*, 12(8), 1640–1644.
- Ma, H., Antoniou, M., Pastina, D., Santi, F., Pieralice, F., Bucciarelli, M., & Cherniakov, M. (2017). Maritime moving target indication using passive GNSS-based bistatic radar. *IEEE Transactions on Aerospace and Electronic Systems*, 54(1), 115–130.
- Martin, F., Camps, A., Park, H., Fabra, F., Rius, A., martin-neira, M., D'Addio, S., Li, W., & Yang, D. (2014). *Typhoon observations using the interferometric GNSS-R technique* (pp. 3790–3793). <https://doi.org/10.1109/IGARSS.2014.6947309>
- Martin, F., Marchan, J. F., Aguasca, A., Vall-Ilossera, M., Corbera, J., Camps, A., Piles, M., Pipia, L., Tardà, A., & Villafranca, A. G. (2011). Airborne soil moisture determination using a data fusion approach at regional level. *IEEE International Geoscience and Remote Sensing Symposium, 2011*, 3109–3112.
- Martin-Neira, M. (1993). A passive reflectometry and interferometry system (PARIS): Application to ocean altimetry. *ESA Journal*, 17(4), 331–355.
- Martin-Neira, M., Caparrini, M., Font-Rossello, J., Lannelongue, S., & Vallmitjana, C. S. (2001). The PARIS concept: An experimental demonstration of sea surface altimetry using GPS reflected signals. *IEEE Transactions on Geoscience and Remote Sensing*, 39(1), 142–150. <https://doi.org/10.1109/36.898676>
- Masters, D. (2019). Design and planning for the first spire GNSS-R missions of 2019. In *Proceedings of IEEE GRSS, specialist meeting reflectometry using GNSS other signals opportunity*.
- Masters, D., Axelrad, P., & Katzberg, S. (2004). Initial results of land-reflected GPS bistatic radar measurements in SMEX02. *Remote Sensing of Environment*, 92(4), 507–520.
- Mayers, D., & Ruf, C. (2019a). Determining tropical cyclone center location with CYGNSS wind speed measurements. In *IGARSS 2019–2019 IEEE international geoscience and remote sensing symposium* (pp. 7529–7532).
- Mayers, D., & Ruf, C. (2019b). Tropical cyclone center fix using CYGNSS winds. *Journal of Applied Meteorology and Climatology*. <https://doi.org/10.1175/JAMC-D-19-0054.1>
- Minsi, A. O., Jianjun, Z., Youjian, H., Yun, Z., & Yadong, L. I. U. (2015). Comparative experiments on soil moisture monitoring with GPS SNR observations. *Geomatics & Information Science of Wuhan University*, 40(1), 117–120.
- Mironov, V. L., Fomin, S. V., Muzalevskiy, K. V., Sorokin, A. V., & Mikhaylov, M. I. (2012). The use of navigation satellites signals for determination the characteristics of the soil and forest canopy. *IEEE International Geoscience and Remote Sensing Symposium, 2012*, 7527–7529.
- Mironov, V. L., Kosolapova, L., & Fomin, S. (2009). Physically and mineralogically based spectroscopic dielectric model for moist soils. *Geoscience and Remote Sensing, IEEE Transactions on*, 47, 2059–2070. <https://doi.org/10.1109/TGRS.2008.2011631>
- Mishra, A., Mukherjee, S., Merz, B., Singh, V. P., Wrights, D., Villarini, G., Paul, S., Kumar, D. N., Khedun, C. P., Niyogi, D., Schumann, G., & Stedinger, J. (2022). An overview of flood concepts, challenges, and future directions. *Journal of Hydrologic Engineering*. [https://doi.org/10.1061/\(ASCE\)HE.1943-5584.0002164](https://doi.org/10.1061/(ASCE)HE.1943-5584.0002164)
- Molina, C., & Camps, A. (2020). First evidences of ionospheric plasma depletions observations using GNSS-R data from CYGNSS. *Remote Sensing*. <https://doi.org/10.3390/rs12223782>
- Morris, M., & Ruf, C. (2017a). Determining tropical cyclone surface wind speed structure and intensity with the CYGNSS satellite constellation. *Journal of Applied Meteorology and Climatology*, 56, 1847–1865. <https://doi.org/10.1175/JAMC-D-16-0375.1>
- Morris, M., & Ruf, C. (2017b). Estimating tropical cyclone integrated kinetic energy with the CYGNSS satellite constellation. *Journal of Applied Meteorology and Climatology*, 56, 235–245. <https://doi.org/10.1175/JAMC-D-16-0176.1>
- Motte, E., Zribi, M., Fanise, P., Egado, A., Darrozes, J., Al-Yaari, A., Baghdadi, N., Baup, F., Dayau, S., Fieuzal, R., et al. (2016). GLORI: A GNSS-R dual polarization airborne instrument for land surface monitoring. *Sensors*, 16(5), 732.
- Munoz-Martin, J. F., Miguelez, N., Castella, R., Fernandez, L., Solanellas, A., Via, P., & Camps, A. (2018). 3Cat-4: combined GNSS-R, L-Band radiometer with RFI mitigation, and AIS receiver for a I-Unit Cubesat based on software defined radio. In *IGARSS 2018–2018 IEEE international geoscience and remote sensing symposium* (pp. 1063–1066).
- Munoz-Martin, J., Fernandez, L., Ruiz-de-Azua, J., & Camps, A. (2020). The flexible microwave payload -2: A SDR-based GNSS-reflectometer and L-band radiometer for CubeSats. *IEEE Journal of Selected Topics in Applied Earth Observations and Remote Sensing*, PP, 1. <https://doi.org/10.1109/JSTARS.2020.2977959>
- Najibi, N., & Jin, S. G. (2013). Physical reflectivity and polarization characteristics for snow and ice-covered surfaces interacting with GPS signals. *Remote Sensing*, 5(8), 4006–4030. <https://doi.org/10.3390/rs5084006>
- Njoku, E. G., & Entekhabi, D. (1996). Passive microwave remote sensing of soil moisture. *Journal of Hydrology*, 184(1), 101–129. [https://doi.org/10.1016/0022-1694\(95\)02970-2](https://doi.org/10.1016/0022-1694(95)02970-2)
- Nogués, O., Sumpsi, A., Camps, A., & Rius, A. (2003). A 3 GPS-channels Doppler-delay receiver for remote sensing applications. In *IGARSS 2003. 2003 IEEE International Geoscience and Remote Sensing Symposium. Proceedings (IEEE Cat. No. 03CH37477)*, 7, 4483–4485.
- Nogues-Correig, O. (2002). *'Disseny, Montatge i Validació d'un Receptor/Gravador de Senyals GPS per a la Demostració del Concepte PARIS,' Proyecto Final Carrera, Univ. Politècnica Catalunya, Barcelona*.
- Nogués-Correig, O., Cardellach, E., Campderros, J., & Rius, A. (2007). A GPS-reflections receiver that computes doppler/delay maps in real time. *Geoscience and Remote Sensing, IEEE Transactions on*, 45, 156–174. <https://doi.org/10.1109/TGRS.2006.882257>
- Olivé, R., Amézaga, A., Carreno-Luengo, H., Park, H., & Camps, A. (2016). Implementation of a GNSS-R payload based on software-defined radio for the 3CAT-2 mission. *IEEE Journal of Selected Topics in Applied Earth Observations and Remote Sensing*, 9(10), 4824–4833.
- Onrubia, R., Pascual, D., Querol, J., Park, H., & Camps, A. (2019). The Global Navigation Satellite Systems Reflectometry (GNSS-R) microwave interferometric reflectometer: hardware, calibration, and validation experiments. *Sensors*, 19(5), 1019. <https://doi.org/10.3390/s19051019>
- Park, H., Camps, A., Pascual, D., Alonso-Arroyo, A., Martín, F., Carreno-Luengo, H., & Onrubia, R. (2014a). Simulation study on tropical cyclone tracking from the ISS using GNSS-R measurements. *International Geoscience and Remote Sensing Symposium (IGARSS)*. <https://doi.org/10.1109/IGARSS.2014.6947378>
- Park, H., Pascual, D., Camps, A., Martín, F., Alonso-Arroyo, A., & Carreno-Luengo, H. (2014b). Analysis of spaceborne GNSS-R delay-doppler tracking. *IEEE Journal of Selected Topics in Applied Earth Observations and Remote Sensing*, 7(5), 1481–1492. <https://doi.org/10.1109/JSTARS.2014.2322198>
- Park, J., Johnson, J., Yi, Y., & Brien, A. (2018). Using "rapid revisit" CYGNSS Wind speed measurements to detect convective activity. *IEEE Journal of Selected Topics in Applied Earth Observations and Remote Sensing*, PP, 1–9. <https://doi.org/10.1109/JSTARS.2018.2848267>
- Pascual, D., Clarizia, M. P., & Ruf, C. S. (2021). Improved CYGNSS wind speed retrieval using significant wave height correction. *Remote Sensing*, 13(21), 4313. <https://doi.org/10.3390/rs13214313>
- Petrou, Z. I., & Tian, Y. (2019). Prediction of sea ice motion with convolutional long short-term memory networks. *IEEE Transactions on Geoscience and Remote Sensing*, 57(9), 6865–6876.
- Pieralice, F., Santi, F., Pastina, D., Bucciarelli, M., Ma, H., Antoniou, M., & Cherniakov, M. (2017). GNSS-based passive radar for maritime surveillance: Long integration time MTI technique. *IEEE Radar Conference (Radar-Conf)*, 2017, 508–513.
- Pinat, E., Defraigne, P., Bergeot, N., Chevalier, J.-M., & Bertrand, B. (2021). Long-term snow height variations in antarctica from GNSS interferometric reflectometry. *Remote Sensing*, 13(6), 1164. <https://doi.org/10.3390/rs13061164>
- Prigent, C., Tegen, I., Aires, F., Marticorena, B., & Zribi, M. (2005). Estimation of the aerodynamic roughness length in arid and semi-arid regions over the globe with the ERS scatterometer. *Journal of Geophysical Research: Atmospheres*, 110(D9), D09205.
- Qian, X., & Jin, S. G. (2016). Estimation of snow depth from GLONASS SNR and phase-based multipath reflectometry. *IEEE Journal of Selected Topics*

- in *Applied Earth Observations and Remote Sensing*, 9(10), 4817–4823. <https://doi.org/10.1109/JSTARS.2016.2560763>
- Qiu, H., & Jin, S. G. (2020). Global mean sea surface height estimated from spaceborne Cyclone-GNSS Reflectometry. *Remote Sens.*, 12(3), 356. <https://doi.org/10.3390/rs12030356>
- Qiu, T., Wang, X., Sun, Y., Li, F., Wang, Z., Xia, J., Du, Q., Bai, W., Cai, Y., Wang, D., et al. (2023). An innovative signal processing scheme for spaceborne integrated GNSS remote sensors. *Remote Sensing*, 15(3), 745.
- Rajabi, M., Nahavandchi, H., & Hoseini, M. (2020). Evaluation of CYGNSS observations for flood detection and mapping during Sistan and Baluchestan Torrential rain in 2020. *Water*, 12, 2047. <https://doi.org/10.3390/w12072047>
- Reynolds, J., Clarizia, M. P., & Santi, E. (2020). Wind speed estimation from CYGNSS using artificial neural networks. *IEEE Journal of Selected Topics in Applied Earth Observations and Remote Sensing*, PP, 1. <https://doi.org/10.1109/JSTARS.2020.2968156>
- Ribó, S., Arco-Fernández, J. C., Cardellach, E., Fabra, F., Li, W., Nogués-Correig, O., Rius, A., & Martín-Neira, M. (2017). A software-defined GNSS reflectometry recording receiver with wide-bandwidth, multi-band capability and digital beam-forming. *Remote Sensing*, 9(5), 450. <https://doi.org/10.3390/rs9050450>
- Ribot, M. A., Kucwaj, J.-C., Botteron, C., Reboul, S., Stienne, G., Leclère, J., Choquel, J.-B., Farine, P.-A., & Benjelloun, M. (2014). Normalized GNSS interference pattern technique for altimetry. *Sensors*, 14(6), 10234–10257.
- Rius, A., Fabra, F., Ribó, S., Arco, J. C., Oliveras, S., Cardellach, E., Camps, A., Nogués-Correig, O., Kainulainen, J., Rohue, E., & Martín-Neira, M. (2012). PARIS Interferometric Technique proof of concept: Sea surface altimetry measurements. *IEEE International Geoscience and Remote Sensing Symposium*, 2012, 7067–7070. <https://doi.org/10.1109/IGARSS.2012.6352035>
- Rivas, M. B. (2007). *Bistatic scattering of global positioning system signals from Arctic sea ice*. University of Colorado at Boulder.
- Rivas, M. B., Maslanik, J. A., & Axelrad, P. (2009). Bistatic scattering of GPS signals off Arctic sea ice. *IEEE Transactions on Geoscience and Remote Sensing*, 48(3), 1548–1553.
- Rodríguez-Alvarez, N., Akos, D., Zavorotny, V., Smith, J., Camps, A., & Fairall, C. (2013). Airborne GNSS-R wind retrievals using delay-Doppler maps. *IEEE Transactions on Geoscience and Remote Sensing*, 51, 626–641. <https://doi.org/10.1109/TGRS.2012.2196437>
- Rodríguez-Alvarez, N., Bosch, X., Camps, A., Aguasca, A., Vall-Ilossera, M., Valencia, E., & Ramos-Perez, I. (2011). Review of crop growth and soil moisture monitoring from a ground-based instrument implementing the Interference Pattern GNSS-R Technique. *Radio Science - RADIO SC*, 46. <https://doi.org/10.1029/2011RS004680>
- Rodríguez-Alvarez, N., Bosch, X., Camps, A., Ramos-Perez, I., Valencia, E., Park, H., & Vall-Ilossera, M. (2012). Vegetation water content estimation using GNSS measurements. *IEEE Geoscience and Remote Sensing Letters*, 9, 282–286. <https://doi.org/10.1109/LGRS.2011.2166242>
- Rodríguez-Alvarez, N., & Garrison, J. (2015). Generalized linear observables for ocean wind retrieval from calibrated GNSS-R delay? Doppler maps. *IEEE Transactions on Geoscience and Remote Sensing*, 54, 1. <https://doi.org/10.1109/TGRS.2015.2475317>
- Rodríguez-Alvarez, N., & Oudrhiri, K. (2021). The bistatic radar as an effective tool for detecting and monitoring the presence of phytoplankton on the ocean surface. *Remote Sensing*, 13, 2248. <https://doi.org/10.3390/rs13122248>
- Rodríguez-Alvarez, N., Podest, E., Jensen, K., & McDonald, K. (2019b). Classifying Inundation in a Tropical Wetlands Complex with GNSS-R. *Remote Sensing*, 11, 1053. <https://doi.org/10.3390/rs11091053>
- Rodríguez-Alvarez, N., Bosch-Lluis, X., Camps, A., Vall-Ilossera, M., Valencia, E., Marchan-Hernandez, J. F., & Ramos-Perez, I. (2009). Soil Moisture retrieval using GNSS-R techniques: Experimental results over a Bare soil field. *IEEE Transactions on Geoscience and Remote Sensing*, 47(11), 3616–3624.
- Rodríguez-Alvarez, N., Camps, A., Vall-Ilossera, M., Bosch-Lluis, X., Moneris, A., Ramos-Perez, I., Valencia, E., Marchan-Hernandez, J. F., Martínez-Fernandez, J., Baroncini-Turricchia, G., et al. (2010). Land geophysical parameters retrieval using the interference pattern GNSS-R technique. *IEEE Transactions on Geoscience and Remote Sensing*, 49(1), 71–84.
- Rodríguez-Alvarez, N., Holt, B., Jaruwatanadilok, S., Podest, E., & Cavanaugh, K. C. (2019a). An Arctic sea ice multi-step classification based on GNSS-R data from the TDS-1 mission. *Remote Sensing of Environment*, 230, 111202.
- Rodríguez-Alvarez, N., Muñoz-Martin, J. F., & Morris, M. (2023). Latest advances in the Global Navigation Satellite System-Reflectometry (GNSS-R) field. *Remote Sensing*, 15(8), 2157.
- Ruf, C., Backhus, R., Butler, T., Chen, C.-C., Gleason, S., Loria, E., McKague, D., Miller, R., O'Brien, A., & van Nieuwstadt, L. (2020). Next generation GNSS-R instrument. In *IGARSS 2020–2020 IEEE international geoscience and remote sensing symposium* (pp. 3353–3356).
- Ruf, C. S., Atlas, R., Chang, P. S., Clarizia, M. P., Garrison, J. L., Gleason, S., Katzberg, S. J., Jelenak, Z., Johnson, J. T., Majumdar, S. J., et al. (2016). New ocean winds satellite mission to probe hurricanes and tropical convection. *Bulletin of the American Meteorological Society*, 97(3), 385–395.
- Ruf, C., & Balasubramaniam, R. (2018). Development of the CYGNSS geophysical model function for wind speed. *IEEE Journal of Selected Topics in Applied Earth Observations and Remote Sensing*. <https://doi.org/10.1109/JSTARS.2018.2833075>
- Ruf, C., Chew, C., Lang, T., Morris, M., Nave, K., Ridley, A., & Balasubramaniam, R. (2018). A new paradigm in earth environmental monitoring with the CYGNSS small satellite constellation. *Scientific Reports*. <https://doi.org/10.1038/s41598-018-27127-4>
- Ruf, C. S., Gleason, S., Jelenak, Z., Katzberg, S., Ridley, A., Rose, R., Scherrer, J., & Zavorotny, V. (2012). The CYGNSS nanosatellite constellation hurricane mission. *IEEE International Geoscience and Remote Sensing Symposium*, 2012, 214–216.
- Ruffini, G., Soulat, F., Caparrini, M., Germain, O., & Martín-Neira, M. (2004). The Eddy Experiment: Accurate GNSS-R ocean altimetry from low altitude aircraft. *Geophysical Research Letters*, 31(12).
- Said, F., Katzberg, S., & Soisuvarn, S. (2017). Retrieving Hurricane maximum winds using simulated CYGNSS power-versus-delay waveforms. *IEEE Journal of Selected Topics in Applied Earth Observations and Remote Sensing*, PP, 1–11. <https://doi.org/10.1109/JSTARS.2017.2695878>
- Santi, E., Pettinato, S., Paloscia, S., Clarizia, M. P., Dente, L., Guerriero, L., Comite, D., & Pierdicca, N. (2020a). Soil Moisture and Forest Biomass retrieval on a global scale by using CyGNSS data and Artificial Neural Networks. 5905–5908. <https://doi.org/10.1109/IGARSS39084.2020.9323896>
- Santi, E., Paloscia, S., Pettinato, S., Fontanelli, G., Clarizia, M. P., Comite, D., Dente, L., Guerriero, L., Pierdicca, N., & Flouy, N. (2020b). Remote sensing of forest biomass using GNSS reflectometry. *IEEE Journal of Selected Topics in Applied Earth Observations and Remote Sensing*, 13, 2351–2368.
- Santi, F., Pastina, D., & Bucciarelli, M. (2020c). Experimental demonstration of ship target detection in GNSS-based passive radar combining target motion compensation and track-before-detect strategies. *Sensors*, 20, 599. <https://doi.org/10.3390/s20030599>
- Schiavulli, D., Frappart, F., Ramillien, G., Darozes, J., Nunziata, F., & Migliaccio, M. (2017). Observing sea/ice transition using radar images generated from TechDemoSat-1 delay Doppler maps. *IEEE Geoscience and Remote Sensing Letters*, 14(5), 734–738.
- Senyurek, V., Lei, F., Boyd, D., Gurbuz, A., Kurum, M., & Moorhead, R. (2020). Evaluations of a machine learning-based CYGNSS soil moisture estimates against SMAP observations. *Remote Sensing*. <https://doi.org/10.3390/rs12213503>
- Shi, J., Du, Y., Du, J., Jiang, L., Chai, L., Mao, K., Xu, P., Ni, W., Xiong, C., Liu, Q., Liu, C., Guo, P., Cui, Q., Li, Y., Chen, J., Wang, A., Luo, H., & Wang, Y. (2012). Progresses on microwave remote sensing of land surface parameters. *Science China Earth Science*, 55, 1052–1078. <https://doi.org/10.1007/s11430-012-4444-x>
- Simone, A. D., Park, H., Riccio, D., & Camps, A. (2017). Sea target detection using spaceborne GNSS-R delay-Doppler maps: Theory and experimental proof of concept using TDS-1 data. *IEEE Journal of Selected Topics in Applied Earth Observations and Remote Sensing*, 10, 4237–4255.
- Soulat, F., Caparrini, M., Germain, O., Lopez-Dekker, P., Taani, M., & Ruffini, G. (2004). Sea state monitoring using coastal GNSS-R. *Geophysical Research Letters*, 31(21), L21303.
- Stilla, D., Zribi, M., Pierdicca, N., Baghdadi, N., & Huc, M. (2020). Desert roughness retrieval using CYGNSS GNSS-R data. *Remote Sensing*, 12, 743. <https://doi.org/10.3390/rs12040743>
- Suberviola, I., Mayordomo, I., & Mendizabal, J. (2012). Experimental results of air target detection with a GPS forward-scattering radar. *IEEE Geoscience and Remote Sensing Letters*, 9, 47–51.



- Sun, Y., Wang, X., Du, Q., Bai, W., Xia, J., Cai, Y., Wang, D., Wu, C., Meng, X., Tian, Y., & others. (2019). The status and progress of fengyun-3e gnss ii mission for gnss remote sensing. In *IGARSS 2019–2019 IEEE international geoscience and remote sensing symposium* (pp. 5181–5184).
- Sun, Y., Huang, F., Xia, J., et al. (2023). GNOS-II on Fengyun-3 satellite series: Exploration of multi-GNSS reflection signals for operational applications. *Remote Sensing*, *15*(24), 5756.
- Tabbagh, A., Camerlynck, C., & Cosenza, P. (2013). Numerical modeling for investigating the physical meaning of the relationship between relative dielectric permittivity and water content of soils. *Water Resources Research*, *36*, 2771–2776. <https://doi.org/10.1029/2000WR900181>
- Tang, F., & Yan, S. (2022). CYGNSS soil moisture estimations based on quality control. *IEEE Geoscience and Remote Sensing Letters*, *19*, 1–5.
- Troglia Gamba, M., Marucco, G., Pini, M., Ugazio, S., Falletti, E., & Lo Presti, L. (2015). Prototyping a GNSS-based passive radar for UAVs: An instrument to classify the water content feature of lands. *Sensors*, *15*(11), 28287–28313.
- Tsang, L., Kong, J. A., & Shin, R. T. (1985). *Theory of microwave remote sensing*.
- Ulabay, F. T., Moore, R. K., & Fung, A. K. (1982). Microwave remote sensing: active and passive. Volume II. Radar remote sensing and surface scattering and emission theory. *Microwave Remote Sensing: Active and Passive. Volume II. Radar Remote Sensing and Surface Scattering and Emission Theory*.
- Ulabay, F. T., Moore, R. K., & Fung, A. K. (1986). Microwave remote sensing: active and passive. Volume III: from theory to applications. *Microwave Remote Sensing: Active and Passive. Volume III: From Theory to Applications*.
- Unnithan, S. L. K., Biswal, B., & Rüdiger, C. (2020). Flood inundation mapping by combining GNSS-R signals with topographical information. *Remote Sensing*, *12*(18), 3026. <https://doi.org/10.3390/rs12183026>
- Unwin, M., Jales, P., Blunt, P., Duncan, S., Brummitt, M., & Ruf, C. (2013). The SGR-ReSI and its application for GNSS reflectometry on the NASA EV-2 CYGNSS mission. In *Proceedings of the 2013 IEEE aerospace conference*, 197. <https://doi.org/10.1109/AERO.2013.6497151>
- Unwin, M. J., et al. (2021). An introduction to the HydroGNSS GNSS reflectometry remote sensing mission. *IEEE Journal of Selected Topics in Applied Earth Observations and Remote Sensing*, *14*, 6987–6999. <https://doi.org/10.1109/JSTARS.2021.3089550>
- Unwin, M., Jales, P., Tye, J., Gommenginger, C., Foti, G., & Rosello, J. (2016). Spaceborne GNSS-reflectometry on TechDemoSat-1: Early mission operations and exploitation. *IEEE Journal of Selected Topics in Applied Earth Observations and Remote Sensing*, *9*(10), 4525–4539.
- Valencia, E., Camps, A., Marchan, J., Park, H., Bosch, X., Rodriguez-Alvarez, N., & Ramos-Perez, I. (2011). Ocean surface's scattering coefficient retrieval by delay-Doppler map inversion. *IEEE Geoscience and Remote Sensing Letters*, *8*, 750–754. <https://doi.org/10.1109/LGRS.2011.2107500>
- Wan, W., Bai, W., Zhao, L., Long, D., Sun, Y., Meng, X., Chen, H., Cui, X., & Hong, Y. (2015). Initial results of China's GNSS-R airborne campaign: soil moisture retrievals. *Chinese Science Bulletin*, *60*, 964–971. <https://doi.org/10.1007/s11434-015-0789-9>
- Wan, W., Liu, B., Zeng, Z., Xi, C., Wu, G., Xu, L., Chen, X., & Hong, Y. (2019). Using CYGNSS data to monitor China's flood inundation during typhoon and extreme precipitation events in 2017. *Remote Sensing*, *11*, 854. <https://doi.org/10.3390/rs11070854>
- Wang, F., Yang, D., Niu, M., Yang, L., & Zhang, B. (2022). Sea ice detection and measurement using coastal GNSS reflectometry: Analysis and demonstration. *IEEE Journal of Selected Topics in Applied Earth Observations and Remote Sensing*, *15*, 136–149. <https://doi.org/10.1109/JSTARS.2021.3133431>
- Wang, F., Yang, D., Zhang, B., Li, W., & Darrozes, J. (2016). Wind speed retrieval using coastal ocean-scattered GNSS signals. *IEEE Journal of Selected Topics in Applied Earth Observations and Remote Sensing*, *9*, 1–12. <https://doi.org/10.1109/JSTARS.2016.2611598>
- Wang, F., Zhang, G., Yang, D., & Kuang, H. (2023). Single-pass tropical cyclone detector and scene-classified wind speed retrieval model for spaceborne GNSS reflectometry. *IEEE Transactions on Geoscience and Remote Sensing*, *61*, 3253564. <https://doi.org/10.1109/TGRS.2023.3253564>
- Wang, J. R., & Schmugge, T. J. (1980). An empirical model for the complex dielectric permittivity of soils as a function of water content. *IEEE Transactions on Geoscience and Remote Sensing*, *4*, 288–295.
- Wang, Q., Zhu, Y., & Kasantikul, K. (2019). A novel method for ocean wind speed detection based on energy distribution of Beidou reflections. *Sensors*, *19*, 2779. <https://doi.org/10.3390/s19122779>
- Wei, H., Yu, T., Tu, J., & Ke, F. (2023). Detection and evaluation of flood inundation using CYGNSS data during extreme precipitation in 2022 in Guangdong Province, China. *Remote Sensing*, *15*, 297. <https://doi.org/10.3390/rs15020297>
- Wu, J., Chen, Y., Guo, P., Wang, X., Hu, X., Mengjie, W., Li, F., Niphy, M., & Hao, Y. (2022). Sea surface wind speed retrieval based on empirical orthogonal function analysis using 2019–2020 CYGNSS data. *IEEE Transactions on Geoscience and Remote Sensing*, *60*, 1–13. <https://doi.org/10.1109/TGRS.2022.3169832>
- Wu, J., Wang, T., & Wu, W. (2018). Retrieval model for soil moisture content using GPS-interferometric reflectometry. *Geomatics and Information Science of Wuhan University*, *43*(6), 887–892.
- Wu, S., Xu, Z., Wang, F., Yang, D., & Guo, G. (2021b). An improved back-projection algorithm for GNSS-R BSAR imaging based on CPU and GPU platform. *Remote Sensing*, *2021*(13), 2107. <https://doi.org/10.3390/rs1312107>
- Wu, X., Dong, Z., Jin, S. G., He, Y., Song, Y., Ma, W., & Yang, L. (2020). First measurement of soil freeze/thaw cycles in the Tibetan Plateau using CYGNSS GNSS-R data. *Remote Sensing*, *12*(15), 2361. <https://doi.org/10.3390/rs12152361>
- Wu, X., Guo, P., Sun, Y., Liang, H., Zhang, X., & Bai, W. (2021a). Recent progress on vegetation remote sensing using spaceborne GNSS-reflectometry. *Remote Sensing*, *13*, 4244. <https://doi.org/10.3390/rs13214244>
- Xing, J., Yu, B., Yang, D., Li, J., Shi, Z., Zhang, G., & Wang, F. (2022). A Real-time GNSS-R system for monitoring sea surface wind speed and significant wave height. *Sensors*, *22*, 3795. <https://doi.org/10.3390/s22103795>
- Yan, Q., & Huang, W. (2018b). Sea ice detection based on unambiguous retrieval of scattering coefficient from GNSS-R delay-Doppler maps. <https://doi.org/10.1109/OCEANSKOBE.2018.8559148>
- Yan, Q., Gong, S., Jin, S., Huang, W., & Zhang, C. (2020a). Near real-time soil moisture in China retrieved from CyGNSS reflectivity. *IEEE Geoscience and Remote Sensing Letters*. <https://doi.org/10.1109/LGRS.2020.3039519>
- Yan, Q., & Huang, W. (2016). Spaceborne GNSS-R sea ice detection using delay-Doppler maps: First results from the UK TechDemoSat-1 mission. *IEEE Journal of Selected Topics in Applied Earth Observations and Remote Sensing*, *9*(10), 4795–4801.
- Yan, Q., & Huang, W. (2018a). Sea ice sensing from GNSS-R data using convolutional neural networks. *IEEE Geoscience and Remote Sensing Letters*, *15*(10), 1510–1514.
- Yan, Q., & Huang, W. (2019a). Detecting sea ice from TechDemoSat-1 data using support vector machines with feature selection. *IEEE Journal of Selected Topics in Applied Earth Observations and Remote Sensing*, *12*(5), 1409–1416.
- Yan, Q., & Huang, W. (2019b). Sea ice concentration estimation from TechDemoSat-1 data using support vector regression. *IEEE Radar Conference (RadarConf)*, 2019, 1–6.
- Yan, Q., & Huang, W. (2019c). Sea ice remote sensing using GNSS-R: A review. *Remote Sensing*, *11*, 2565. <https://doi.org/10.3390/rs11212565>
- Yan, Q., & Huang, W. (2020). Sea ice thickness measurement using spaceborne GNSS-R: First results with TechDemoSat-1 data. *IEEE Journal of Selected Topics in Applied Earth Observations and Remote Sensing*, *13*, 577–587.
- Yan, Q., Huang, W., Jin, S., & Jia, Y. (2020b). Pan-tropical soil moisture mapping based on a three-layer model from CYGNSS GNSS-R data. *Remote Sensing of Environment*, *247*, 111944. <https://doi.org/10.1016/j.rse.2020.111944>
- Yan, Q., Huang, W., & Moloney, C. (2017). Neural networks based sea ice detection and concentration retrieval from GNSS-R delay-Doppler maps. *IEEE Journal of Selected Topics in Applied Earth Observations and Remote Sensing*, *10*(8), 3789–3798.
- Yang, G., Bai, W., Wang, J., Hu, X., Zhang, P., Sun, Y., Xu, N., Zhai, X., Xiao, X., Xia, J., et al. (2022). FY3E GNOS II GNSS reflectometry: Mission review and first results. *Remote Sensing*, *14*(4), 988.
- Yang, L., Wu, Q., Zhang, B., Liang, Y., Hong, X., & Zou, W. (2016). SVRM-assisted soil moisture retrieval method using reflected signal from BeiDou GEO satellites. *Journal of Beijing University of Aeronautics and Astronautics*, *42*, 1134–1141. <https://doi.org/10.13700/j.bh.1001-5965.2015.0656>
- Yang, S., Jia, Y., & Ye, M. (2021a). Significant wave height estimation from joint CYGNSS DDMA and LES observations. *Sensors*, *21*(18), 6123. <https://doi.org/10.3390/s21186123>



- Yang, T., Sun, Z., & Jiang, L. (2023a). A novel index for daily flood inundation retrieval from CYGNSS measurements. *Remote Sensing*, *15*, 524. <https://doi.org/10.3390/rs15020524>
- Yang, T., Wan, W., Sun, Z., Liu, B., Li, S., & Chen, X. (2020). Comprehensive evaluation of using TechDemoSat-1 and CYGNSS data to estimate soil moisture over mainland China. *Remote Sensing*, *12*, 1699. <https://doi.org/10.3390/rs12111699>
- Yang, W., Gao, F., Xu, T., Wang, N., Tu, J., Jing, L., & Kong, Y. (2021b). Daily flood monitoring based on spaceborne GNSS-R data: A case study on Henan, China. *Remote Sensing*, *13*, 4561. <https://doi.org/10.3390/rs13224561>
- Yang, W., Guo, F., Zhang, X., Xu, T., Wang, N., & Jing, L. (2023b). Daily landscape freeze/thaw state detection using spaceborne GNSS-R data in Qinghai-Tibet Plateau. *IEEE Transactions on Geoscience and Remote Sensing*, *61*, 3314622.
- Yin, C., Huang, F., Xia, J., Bai, W., Sun, Y., Yang, G., Zhai, X., Xu, N., Hu, X., Zhang, P., Wang, J., Du, Q., Wang, X., & Cai, Y. (2023). Soil moisture retrieval from multi-GNSS reflectometry on FY-3E GNOSS-II by land cover classification. *Remote Sensing*, *15*(4), 1097. <https://doi.org/10.3390/rs15041097>
- Yueh, S., Shah, R., Chaubell, J., Hayashi, A., Xu, X., & Colliander, A. (2020). A semiempirical modeling of soil moisture, vegetation, and surface roughness impact on CYGNSS reflectometry data. *IEEE Transactions on Geoscience and Remote Sensing*, *11*, 1–17. <https://doi.org/10.1109/TGRS.2020.3035989>
- Yueji, L., Chao, R. E. N., Yibang, H., Yalong, P. A. N., & Zhigang, Z. (2020). Multi-star linear regression retrieval model for monitoring soil moisture using GPS-IR. *Acta Geodaetica Et Cartographica Sinica*, *49*(7), 833.
- Yun, Z., Wanting, M., Qiming, G., Yanling, H., Zhonghua, H., Yunchang, C., Qing, X., & Wei, W. (2014). Detection of Bohai Bay sea ice using GPS-reflected signals. *IEEE Journal of Selected Topics in Applied Earth Observations and Remote Sensing*, *8*(1), 39–46.
- Zavorotny, V., Gleason, S., Cardellach, E., & Camps, A. (2014). Tutorial on remote sensing using GNSS bistatic radar of opportunity. *Geoscience and Remote Sensing Magazine, IEEE*, *2*, 8–45. <https://doi.org/10.1109/MGRS.2014.2374220>
- Zavorotny, V. U., Larson, K. M., Braun, J. J., Small, E. E., Gutmann, E. D., & Bilich, A. L. (2009). A physical model for GPS multipath caused by land reflections: Toward bare soil moisture retrievals. *IEEE Journal of Selected Topics in Applied Earth Observations and Remote Sensing*, *3*(1), 100–110.
- Zavorotny, V. U., & Voronovich, A. G. (2000). Scattering of GPS signals from the ocean with wind remote sensing application. *IEEE Transactions on Geoscience and Remote Sensing*, *38*(2), 951–964.
- Zeiger, P., Frappart, F., Darrozes, J., Prigent, C., & Jimenez, C. (2022). Analysis of CYGNSS coherent reflectivity over land for the characterization of pan-tropical inundation dynamics. *Remote Sensing of Environment*, *282*, 113278. <https://doi.org/10.1016/j.rse.2022.113278>
- Zhang, C., Shi, S., Yan, S., & Gong, J. (2023b). Moving target detection and parameter estimation using BeiDou GEO satellites-based passive radar with short-time integration. *IEEE Journal of Selected Topics in Applied Earth Observations and Remote Sensing*, *16*, 3959–3972.
- Zhang, S., Ma, Z., Li, Z., Zhang, P., Liu, Q., Nan, Y., Zhang, J., Hu, S., Feng, Y., & Zhao, H. (2021). Using CYGNSS data to map flood inundation during the 2021 extreme precipitation in Henan Province, China. *Remote Sensing*, *13*, 5181. <https://doi.org/10.3390/rs13245181>
- Zhang, S., Ma, Z., Liu, Q., Hu, S., Feng, Y., Zhao, H., & Guo, Q. (2023a). POBI interpolation algorithm for CYGNSS near real time flood detection research: A case study of extreme precipitation events in Henan, China in 2021. *Advances in Space Research*, *71*(6), 2862–2878. <https://doi.org/10.1016/j.asr.2022.11.016>
- Zhang, Y., Chen, X., Meng, W., Yang, S., Han, Y., Hong, Z., Yin, J., & Liu, W. (2022a). Wind direction retrieval from CYGNSS L1 level sea surface data based on machine learning. *IEEE Transactions on Geoscience and Remote Sensing*, *60*, 1–13.
- Zhang, Y., Yan, Z., Yang, S., Meng, W., Gu, S., Qin, J., Han, Y., & Hong, Z. (2022b). Research on shore-based river flow velocity inversion model using GNSS-R raw data. *Remote Sensing*, *14*, 1170. <https://doi.org/10.3390/rs14051170>
- Zhang, Y., Zhao, X., Yang, S., Han, Y., Hong, Z., Meng, W., Chen, Z., & Liu, W. (2024). Research on sea surface wind speed FM based on CYGNSS and HY-2B microwave scatterometer. *IEEE Transactions on Geoscience and Remote Sensing*, *62*, 1–15.
- Zhang, Z., Guo, F., Zhang, X., Li, Z., & Liu, H. (2023c). Physical modeling and compensation for systematic negative errors in GNSS-R snow depth retrieval. *IEEE Transactions on Geoscience and Remote Sensing*, *61*, 1–12.
- Zhou, X., Chen, J., Wang, P., Zeng, H., Fang, Y., Men, Z., & Liu, W. (2019). An efficient imaging algorithm for GNSS-R bi-static SAR. *Remote Sensing*, *11*(24), 2945. <https://doi.org/10.3390/rs11242945>
- Zhou, X., Wang, P., Zeng, H., & Chen, J. (2022). Moving target detection using GNSS-based passive bistatic radar. *IEEE Transactions on Geoscience and Remote Sensing*, *60*, 5113415.
- Zhu, Y., Guo, F., & Zhang, X. (2022). Effect of surface temperature on soil moisture retrieval using CYGNSS. *International Journal of Applied Earth Observation and Geoinformation*, *112*, 102929.
- Zhu, Y., Yu, K., Zou, J., & Wickert, J. (2017). Sea ice detection based on differential delay-Doppler maps from UK TechDemoSat-1. *Sensors*, *17*(7), 1614. <https://doi.org/10.3390/s17071614>
- Zribi, M., Huc, M., Antokoletz, S., Le Page, M., Pierdicca, N., & Baghdadi, N. (2019). Soil moisture estimation using CYGNSS constellation. 7014–7017. <https://doi.org/10.1109/IGARSS.2019.8898643>
- Zribi, M., Motte, E., Baghdadi, N., Baup, F., Dayau, S., Fanise, P., Guyon, D., Huc, M., & Wigneron, J. P. (2018). Potential applications of GNSS-R observations over agricultural areas: Results from the GLORI airborne campaign. *Remote Sensing*, *10*(8), 1245.

## Publisher's Note

Springer Nature remains neutral with regard to jurisdictional claims in published maps and institutional affiliations.